SQUID MEASUREMENTS OF MAGNETIC VORTICES IN VERY UNDERDOPED YTTRIUM-BARIUM-COPPER-OXIDE

A DISSERTATION
SUBMITTED TO THE DEPARTMENT OF PHYSICS
AND THE COMMITTEE ON GRADUATE STUDIES
OF STANFORD UNIVERSITY
IN PARTIAL FULFILLMENT OF THE REQUIREMENTS
FOR THE DEGREE OF
DOCTOR OF PHILOSOPHY

Brian Willard Gardner
December 2004

I certify that I have read this dissertation and that, in my opinion, it is fully adequate in scope and quality as a dissertation for the degree of Doctor of Philosophy.

Kathryn A. Moler
(Principal Advisor)

I certify that I have read this dissertation and that, in my opinion, it is fully adequate in scope and quality as a dissertation for the degree of Doctor of Philosophy.

Malcolm R. Beasley

I certify that I have read this dissertation and that, in my opinion, it is fully adequate in scope and quality as a dissertation for the degree of Doctor of Philosophy.

David Goldhaber-Gordon

Approved for the University Committee on Graduate Studies.

Abstract

This dissertation describes the first demonstration of a scanning Superconducting QUantum Interference Device (SQUID) susceptometer – a new tool for the study of local magnetic properties of materials – and a series of studies where we apply this tool to investigate vortices in the cuprate superconductor $YBa_2Cu_3O_{6+x}$. These studies demonstrate that the scanning SQUID susceptometer can be applied to answer questions for technological applications, such as the study of vortex pinning, as well as fundamental questions, such as tests of theories of cuprate superconductivity. The new samples of high quality single crystals of very underdoped $YBa_2Cu_3O_{6+x}$, made available to us by Ruixing Liang, Doug Bonn, and Walter Hardy of the University of British Columbia, have also played a critical role in allowing us to carry out these experiments.

In Chapter 2 we describe our tool: a scanning SQUID with an 8μm pickup loop, and an integrated 21μm diameter field coil for applying a local magnetic field. Together these comprise the susceptometer, which is tested by measuring the susceptibility of individual 3μm diameter tin disks. Images of the disks agree well with numerical modelling based on the known geometry of the SQUID susceptometer. The spatial resolution of the device is 8μm, set by the size of the pickup loop, and the low-field spin sensitivity between 1.5 and 6K is $1 \times 10^5 \mu_B/\sqrt{\text{Hz}}$ while scanning.

In Chapter 3 we demonstrate the application of the scanning SQUID susceptometer to the controlled, reversible manipulation of individual vortices in a superconductor using a locally applied magnetic field. The SQUID is used to image the vortices before and after moving. We calculate the force applied on a rigid vortex and find that ~ 0.5pN is necessary to move vortices in underdoped single crystals of $YBa_2Cu_3O_{6+x}$

with $T_c \sim 12$K.

Chapter 4 describes how locally applied magnetic fields from the SQUID susceptometer can be used to create vortex-antivortex pairs in superconducting films and thin crystals. These pairs typically annihilate on some timescale which depends on temperature. We use the SQUID susceptometer to create and observe vortex-antivortex pairs, and watch how they annihilate. We present measurements of annihilations at different locations in a sample of highly underdoped $YBa_2Cu_3O_{6+x}$, and show how different annihilation characteristics can be used to infer the qualitative nature of the local pinning landscape. Our results suggest that pinning sites in these materials have a wide range of energies, and that the length scale for the distribution of deep pinning sites is on the order of microns. We also present measurements of the distribution of annihilation times as a function of temperature. Even in the simplest cases, the pair lifetimes did not fit a simple picture of thermal activation of a vortex or antivortex out of a square-well pinning site, suggesting that pinning is complicated.

Chapter 5 addresses the long-standing debate about whether spin-charge separation is the root cause of the peculiar normal state properties and high T_c's of the cuprate superconductors. We performed the experiment proposed by Senthil and Fisher, in which a ring of cuprate superconductor would exhibit a vortex memory effect on cycling temperature from below T_c to above T_c and back, due to the presence of a topological excitation know as a vison. We did not detect the signature vortex memory effect, and our results place a conservative upper limit on the vison energy of 190K$\cdot k_B$. This is inconsistent with the theory, which predicts a vison energy on the order of 500-700K$\cdot k_B$ for our underdoped $YBa_2Cu_3O_{6+x}$ samples. As a result, spin-charge separation theories which predict visons seem unlikely as an explanation of cuprate superconductivity.

Finally, in Chapter 6 we report measurements of single vortex dynamics in a superconducting $YBa_2Cu_3O_{6+x}$ ring. In addition to the expected states of different numbers of vortices inside the centre of the ring, we also found evidence for intermediate states between n and $n+1$ vortices in the ring. Our measurements showed that there were several different intermediate states, but almost never more than one at a given temperature. These intermediate states were quite robust in the sense that

they persisted almost to T_c of the ring. Measurements of the temperature dependence of transitions between states was consistent with thermal activation over a barrier, but the barrier was much lower than would be expected for a rigid vortex moving across the ring wall. We conjecture that the vortices in our ring behave as stacks of pancake vortices and the intermediate states we observed were due to split stacks in which some pancake vortices remain inside the ring, while some escape outside.

In sum, in this dissertation we introduce a new form of scanning SQUID microscope: the scanning SQUID susceptometer, apply it to the study of single vortex pinning through new techniques of manipulating vortices with local magnetic fields and creation of vortex-antivortex pairs, and use it in conjunction with superconducting rings to study single vortex dynamics, and to test spin-charge separation theories of the cuprates by detecting the presence or absence of a vortex memory effect.

Acknowledgements

There are a great many people to thank who have unselfishly given their help and support over the course of my six years in graduate school. Chief among them is my advisor, Kathryn Moler. I would like to thank Kam especially for her inspiration – it's not hard to get me excited about physics, but Kam's brilliance and enthusiasm made working with her a rare treat. I'm grateful to have been so lucky. I would also like to thank Kam for her belief in me, for the opportunity to do exciting work, and the push to do great work, and for her patience and understanding when I struggled. She continues to be a great role model, both in physics and outside of it.

To my reading committee: Mac Beasley, for feeding and sharing my enthusiasm in our many great discussions after his *Phenomenology of Superconductivity* lectures. David Goldhaber-Gordon, for inspirational unending interest in everything, and for all his shared ideas, even at 2A.M. in the basement halls. To the rest of my defense committee: Ian Fisher, for his help and enthusiasm when I went to him with the most oddball ideas, and for being a genuine friend among the faculty, and Ravi Vakil, my defense committee chair, for a meaningful connection back to my alma mater.

Thank you to my friends and coworkers in the Moler group, who made it such a great place to work. First, to the three of my cohort as Kam's original graduate students: Janice Guikema, who I worked very closely with on all of the imaging experiments – I can't imagine a better person to work with. Per Björnsson, for being ready to help with anything and find an answer to every question. Eric Straver, my fellow Canadian, for his healthy dose of reality and killer sense of humour. Special thanks to (relative) newcomers to the group: Nick Koshnick, who worked very closely with me on the vortex dynamics in rings, for his imperturbable enthusiasm, his friendship,

and his willingness to be my arms and legs (and occasionally my brain) while I was an invalid. Physics was never so fun. Hendrik Bluhm, who did a lot of modelling for the vortex dynamics, for his good nature, clear thinking, and willingness to discuss physics (and sailing, and philosophy) at any length. Clifford Hicks, for his initial work on the rings project, and for sharing his interests in language and art. Rafael Dinner, for his willingness to debate, and vigorous defense of the right to do so. Yu-Ju Lin, Zhifeng Deng, for politely accomodating my horrible Mandarin, and our post-docs: Mark Topinka, for his limitless stream of ideas, equally limitless helpfulness, and for being a kindred spirit in appreciation of Tolkien, and Jenny Hoffman, for inspiration, humour, frankness, and chocolate.

There are also many of our collaborators from other institutions I would like to thank for sharing their efforts with me: Doug Bonn, Walter Hardy & Ruixing Liang, who generously provided the $YBa_2Cu_3O_{6+x}$ crystals that made this work possible. Doug in particular spent many, many hours in the lab with Janice and me on his sabbatical at Stanford, shouldering much of the work, teaching us from his vast array of skills (it is to Doug that I owe all my crystal-handling prowess, see p71), and sharing his excellent sense of humour. Martin Huber, for everything he has taught me about SQUIDs and their associated electronics, and all the other wealth of knowledge he has shared with me the many times we have worked together, and for being a friend as much as a collaborator. John Kirtley, for his many contributions in our collaborations, especially the great fun we had working on the vortex dynamics in rings while he was visiting Stanford for a month, and also for his mentorship and guidance at SQUID2001 and M2SRIO. Vladimir Kogan, for all his help with modelling, and his patience with my questions. Mark Ketchen, for his development of the SQUID susceptometers. Todadri Senthil & Matthew Fisher, for many insightful discussions regarding visons. And finally NSERC, and the Department of Energy for funding support. I'd also like to thank Kellogg, the makers of Pop Tarts^{TM}, for sustaining me through much of the data taking.

I also appreciate the work of the many fine administrative staff who made my life *so* much easier: Marcia Keating, Kathleen Guan, Maria Frank, Droni Chiu, Jeff Morrison, Mark Gibson, Judy Clark, Cyndi Mata, and Larry Candido.

Graduate school is, of course, so much more beyond the lab. To all of my friends who have shared these years, and whose contributions I cannot possibly begin to list, thank you. My closest friends: Puneet Batra, Jonathan Goldman & Anu Tewary, Debbie Berebichez, Matt Szczesny, John Poulos, Ken Stalzer, and Cameron Shelton. The Beer Night & Dude's Lunch crowd: Sam Waldman, Dave Weld, Sameer Bhalotra, Noah Helman, Randy Grow. McCullough, Moore & Varian friends: Myles Steiner, Moe Badi, Sylvia Smullin, David Santiago, Sara Cronenwett, Josh Folk, Ron Potok, Mark Peterman, Gabriel & Martine Zeltzer, Laila Mattos, Joe Hennawi, Aaron Miller. Roommates & neighbours: Talal Al-Attar, Elaine Cheung, Nishita Doshi. Gaming table friends: Jeremy Bergfeld, Rob Starling, Scott Atwood, Christian Shelton, Sarah Pilat. All my friends from Toronto, especially those who came to visit: Jacob Etches, Mary Anne Guerin, Helen Liú, Chau Tran, Ted Fortuna & Judy McCormick, and Seth Eatinger, who defies categorization.

I would like to thank some of the people in the community who enriched my life here: Zéng Lǎoshī, John & Katie Fogelsong, Rick Pam, the Friday Morning basketball guys. I thank Dr. Loretta Chou, for putting me back together again, and again, and Marvin & George for their colourful casting.

Finally, I would like to thank my family: My new family, Hue, Ylan & Ai Linh Tran, who have been so gracious in taking me in and giving of their support, advice, hospitality, and friendship. Thank you to my parents, for their love, patience, and support, and for always nurturing my curiosity. Thank you to my fiancée, Monica, who has been there every step of the way these last two-and-a-half years, sharing the highs and somehow knowing when to push and when to console in the lows, for her love, laughter, wisdom, and boundless patience.

Brian Willard Gardner
Stanford University
December 2004

Contents

List of Tables

List of Figures

Chapter 1

Introduction

This dissertation describes a sequence of experiments I worked on over the last six years here in the Moler lab. All of them involve Superconducting Quantum Interference Devices (SQUIDs) as the main sensor, and nearly all of them involve scanning microscopy and vortices in underdoped cuprate superconductors, specifically $YBa_2Cu_3O_{6+x}$. To condense six years into a single sentence, my work included implementing the first Scanning SQUID Susceptometer, developing a technique for the controlled manipulation of vortices with a locally applied magnetic field, developing a technique for creating vortex-antivortex pairs and studying their annihilation characteristics, performing an experiment ruling out a spin-charge separation theory of the cuprate superconductors which had predicted a 'vortex memory effect', and measuring single vortex dynamics in superconducting rings.

The bulk of the dissertation, of course, is concerned with the details of what I did and how I did it. My task in the introduction is explain why I did it, and to convince the reader that it is worth reading about. Some background and context are necessary to appreciate the motivations as well as some of the detail in later chapters, so I'll start with those.

The most basic description of what I've done might be: use SQUIDs to study underdoped cuprate superconductors by imaging the flux on the surface of the sample, in particular imaging vortices. This encapsulates most of the work in this thesis, and suggests a convenient basis for explaining the background and motivation by applying the questions "What are _____?" and "Why _____?" to the words

'superconductors', 'vortices', 'SQUIDs', 'imaging', and 'underdoped cuprates.'

1.1 Superconductors

Superconductivity is a correlated state of many electrons, described by a macroscopic wavefunction and displaying several characteristic properties. The most significant of these properties are vanishing dc resistivity, expulsion of magnetic flux (the Meissner effect), and quantization of the fluxoid. It is phenomenologically described by a Ginzburg-Landau order parameter related to the macroscopic wavefunction.

$$\psi_{\mathrm{GL}} = \sqrt{\rho_s} e^{i\varphi} \tag{1.1}$$

The amplitude squared of this wavefunction gives the probability density for finding a superconducting pair. This is known as the superfluid density and denoted ρ_s. The phase, φ, plays an extremely important role in superconductivity. The fact that all the superconducting pairs have quantum mechanical phase which is 'locked' relative to one another is referred to as phase coherence, and it is this which gives rise to the hallmarks of the superconducting state.

The phase of the wavefunction is linked to the motion of the pairs: a gradient in the phase causes pairs to move and a current to flow. The phase of the wavefunction is also linked to magnetic fields – specifically to the vector potential, $\vec{A}$, through gauge invariance.

The source of the Meissner effect is that the vector potential giving rise to a field causes the phase of the superconducting wavefunction to wind up, which in turn drives a current that screens the magnetic field out of the sample. Since this process is lossless, it proceeds until the field is completely screened out of the sample or superconductivity is somehow broken.

The screening takes place over a distance given by the penetration depth (phenomenological parameter λ). Lambda is closely related to the magnitude of the wavefunction, i.e. how much supercurrent is available to participate in the screening ($\lambda \sim 1/\sqrt{\rho_s}$).

The other important phenomenological scale is the characteristic length for changes in the magnitude of the wavefunction (the coherence length, ξ). This plays an important role for vortices, as the core of a vortex is a region where superconductivity is destroyed and ρ_s vanishes. The size of the core, the length scale over which the superconducting wavefunction 'heals' to its equilibrium value in the material, is ξ.

The zero dc resistivity is due to the fact that superconducting charge carriers occupy a single quantum ground state. Perturbations of the system which drive a current cannot create loss unless they excite some carriers out of the ground state (the fluctuation-dissipation theorem requires fluctuations between quantum states to dissipate energy). Because of phase coherence, all the electrons in a superconductor move together when they respond to external perturbations. To excite an electron out of the superconducting state you would have to force it to move independently – that is, change its phase in a way that 'unlocks' it from all the other electrons. This, however, costs energy, and can only occur if you push hard enough. Exactly what defines 'hard enough' is the superfluid density, which sets the scale for how much energy it costs to create a phase gradient. This idea of a limit on how hard you can push the superconductor gives rise to the notion of a local *critical current density*, $\vec{J}_c$, above which superconductivity breaks down.

Aside from vanishing dc resistivity and the expulsion of magnetic fields, the chief interesting property is that of fluxoid quantization. This arises from the phase coherence of the superconducting pairs, and the relation of the phase to magnetic flux. If a continuous piece of superconductor surrounds a region with some magnetic flux, then the flux causes a winding of the superconducting phase. The wavefunction must be single-valued, so the phase must change by a multiple of 2π.

$$\oint \nabla\varphi = n2\pi \tag{1.2}$$

expressing $\nabla\varphi$ in terms of the vector potential and supercurrent, we get

$$n2\pi = \oint (\frac{m^*}{2e\hbar\rho_s}\vec{J}_s + \frac{2e}{\hbar}\vec{A}) \cdot d\vec{\ell} \tag{1.3}$$

$$n2\pi\frac{\hbar}{2e} = \oint \frac{m^*}{4e^2\rho_s}\vec{J}_s \cdot d\vec{\ell} + \int_S \nabla \times \vec{A} \cdot d\vec{S} \tag{1.4}$$

$$n\frac{h}{2e} = \oint \frac{m^*}{4e^2\rho_s}\vec{J}_s \cdot d\vec{\ell} + \Phi \tag{1.5}$$

where we have used Stokes' theorem to convert the contour integral of the vector potential into the magnetic flux enclosed. If the surrounding piece of superconductor is much thicker than the penetration depth, λ, then the contour of integration may be taken sufficiently far into the sample that the screening currents, $\vec{J}_s$, have died off and the result is that the flux is quantized in units of $h/2e$. More generally, it is the fluxoid – containing contributions from both the flux and the line integral of the supercurrent – which is quantized.

1.2 Why Superconductors?

The zero dc resistance property of superconductors promises many applications, including energy storage and loss-free power lines. Their magnetic properties could be used for levitating trains and frictionless bearings. Already superconductors are used in powerful electromagnets, such as those in Magnetic Resonance Imaging (MRI) machines, and in electronic filters in cellular phone base stations. At the time of writing, superconducting qubits seem the most promising road forward to a quantum computer. A workable, affordable, room-temperature superconductor would change the world, probably as much as the steam engine or nuclear energy.

Aside from the techno- and sociological implications of room-temperature superconductivity if it were to be discovered in the future, superconductivity as it exists today is scientifically worth study in its own right. The cuprate superconductors, especially, are thought to depend on the physics of strongly correlated electrons – a unifying theme for many of the great unsolved problems in condensed matter.

1.3 Vortices

Flux quantization can be observed not only in superconducting samples with holes, but also in some superconductors which respond to applied fields by admitting flux quanta as vortices.

When an applied field is sufficiently large that the energy required to screen it out exceeds the condensation energy saved by maintaining the superconducting state, superconductivity will begin to collapse. The precise fashion in which this happens depends on the details of the sample shape and the applied fields. Generally, though, the response can be broken down into two distinct classes, and which one occurs depends on the energy of the interface between the superconducting region and the region that has been driven back into the normal state by the applied field.

If the interface energy is positive, then the superconductor will assume a configuration which minimizes the boundary between superconducting and normal regions. If the interface energy is instead negative, then the system will maximize the boundary by subdividing the normal-state region as much as possible. Since the normal region carries flux with it and is surrounded by superconductor, the flux is quantized and the maximum amount of subdivision possible is obtained by splitting the normal regions into tubes which carry a flux of $h/2e$. The swirling supercurrent which surrounds the normal core and confines the flux gives rise to the name vortex.

The sign of the interface energy between superconducting and normal regions is determined by the ratio of the two fundamental phenomenological parameters $\kappa \equiv \lambda/\xi$. Heuristically, consider that the penetration depth, λ, determines the size of the region near the boundary over which the field is screened out, while ξ sets the distance over which the superfluid density can change. If λ is short and ξ is long, then the field must be screened out over a short distance while the superfluid available to screen it is still significantly depressed. That is difficult, and energetically unfavourable. On the other hand, if λ is long and ξ is short, then superconductivity can recover quickly and screening takes place mostly in the fully superconducting region. Mathematically, one compares the condensation energy and the superfluid energy and finds that the interface energy is positive for $\kappa < \sqrt{2}$ and negative for $\kappa > \sqrt{2}$ (Abrikosov 1957).

Superconductors for which the former is true are called Type I, while the latter, which support vortices, are called Type II.

Vortices repel each other if they have the same sense (their flux points in the same direction), and attract each other if they have opposite sense (because they can annihilate one another and remove the energy of two vortices from the system). The mutual force of attraction can be calculated as in de Gennes (1989) to be:

$$F_r = \vec{J}_s \times \vec{\Phi}_0 \tag{1.6}$$

where $\vec{J}_s$ is the supercurrent density due to the first vortex at the location of the second vortex, and $\vec{\Phi}_0$ is a vector of length $\Phi_0 = h/2e$ along the direction of the second vortex. The same equation can be used to determine the force on a vortex due to any arbitrary supercurrent density – it need not come from another vortex. This formulation ignores the extent of the vortex core.

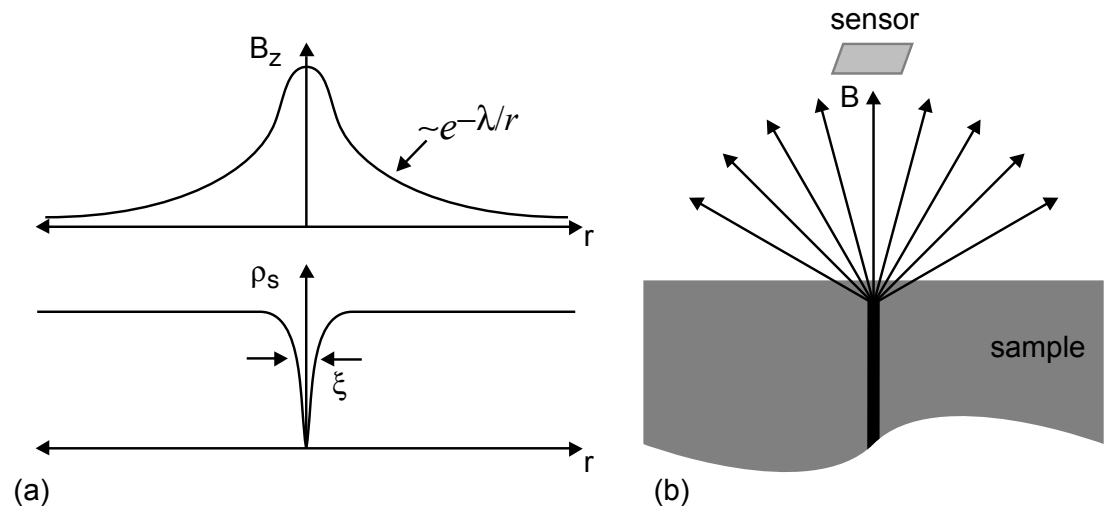

Figure 1.1: Anatomy of a vortex: (a) Deep in side the superconductor, the field profile of the vortex falls off exponentially over a length scale λ outside the vortex core (top); inside a core of size $\sim \xi$, the superfluid density falls to zero (bottom). (b) Near the surface of the superconductor, the flux of the vortex begins to spread out. To a magnetic sensor above, the vortex looks approximately like a magnetic monopole situated a distance λ below the sample surface.

1.4 Why Vortices?

Most of the work we've done in our lab has involved vortices. Vortices are particularly interesting objects in superconductivity for many reasons. They are described by two parameters: the penetration depth, λ, and the coherence length, ξ, which are the fundamental phenomenological parameters of superconductivity – they define almost everything about the superconducting state of a material.[1] Precise measurements on single vortices are valuable because they can yield an absolute measurement of the penetration depth (Moler et al. 1998; Guikema 2004). With sufficient spatial resolution, one could also use individual vortex measurements to determine the coherence length, ξ, by measuring the field profile around the core (see Figure 1.1).

As a vortex locally destroys superconductivity, it provides something of a window into the normal state of the material. For the cuprates, the normal state (especially on the underdoped side of the phase diagram, see Figure 1.2) is the big mystery. It is presumed (or at least hoped) that figuring out what's going on the the pseudogap will reveal the mechanism by which the cuprates become superconductors. The normal core of a vortex in the cuprates, then, is presumably a tiny, isolated sample of the pseudogap state, encapsulated in an object whose behaviours and surrounding state of superconductivity we think we understand.

Aside from the importance of vortices for fundamental questions of superconductivity, they also play a key role in technological applications. Movement of vortices is the source of dissipation in a superconductor.[2] Understanding what pins vortices and prevents them from moving is a key area of research for developing better superconducting devices. Some of the techniques we've pioneered in our lab, such as controlled movement of vortices, could be applied to detailed studies of vortex pinning.

[1] Except, of course, the mechanism of superconductivity and its associated characteristics such as internal angular momentum of Cooper pairs, or exotic core states in vortices.

[2] It causes dissipation even for dc current flow. There are also inherent ac losses in superconductors, but I'm not talking about those here.

1.5 Underdoped $YBa_2Cu_3O_{6+x}$

Cuprate superconductors are members of the perovskite family of ceramics. They derive their name from the common characteristic of copper-oxygen layers in the materials. In the undoped compound, these CuO planes are antiferromagnetic insulators, but superconductivity occurs when sufficient charge carriers are added. The layered structure of the cuprates results in highly anisotropic superconductivity in these materials. The penetration depth for screening currents running in the CuO planes (the crystallographic ab-plane) is denoted λ_{ab} and can be hundreds of times smaller than that for screening currents running perpendicular to the planes (along the crystallographic c-axis), denoted λ_c. In particular, very underdoped YBCO has λ_{ab} of order a micron, while λ_c may be in excess of 100μm. Meanwhile, the coherence length, ξ is of order ten Ångstroms, placing the material well into the Type II class of superconductors. The high anisotropy means that while vortices running along the c-axis, with their currents running in the ab-plane, are symmetric, off-axis vortices are not. Vortices running in between the CuO planes are highly elongated along the plane direction, and are called Josephson vortices in analogy with the vortices occurring in Josephson junctions. At very low doping, hence low superfluid density, the coupling between planes is very weak, and even c-axis oriented vortices may be described as individual 'pancake' vortices in each layer coupled together by electromagnetic and possibly Josephson coupling.

The discovery of the cuprates, with their high T_c's, caught physicists by surprise. The T_c's of the cuprates exceeded limits predicted by conventional BCS theory, and brought the question 'How high can we go?' back to the table. To answer that, and to get ideas for where else we might look to find or design materials with yet higher T_c's, everyone wants to know the mechanism by which superconductivity in the cuprates works.[3]

The superconducting state of the cuprates is not remarkably different from superconductivity in other materials in the sense that it exhibits the same hallmark

[3]There is still a separate question of the role of phase fluctuations: even if the mechanism for cuprate superconductivity were understood, and a "better" material were designed, T_c may in fact be limited by phase fluctuations rather than the mean field T_c.

characteristics described above (section 1.1), and is generally well described by the existing phenomenological theories (London and Ginzburg-Landau). It is the normal (non-superconducting) parent state and the mechanism for its transition into superconductivity which has thus far resisted adequate theoretical description.

The cuprates are unique among known superconductors in that they arise (at zero temperature) from doping an insulator, whereas most superconductors develop from a metallic parent state. This alone suggests that the very underdoped samples, where superconductivity first appears, should be an important region to search for clues to the mechanism by which the superconductivity arises. In addition, the underdoped region of the phase diagram shows interesting behaviour in the normal state: increasing the temperature above T_c one enters the pseudogap regime where there is evidence of a remnant of the superconducting gap (or something like it) though superconductivity has been suppressed.

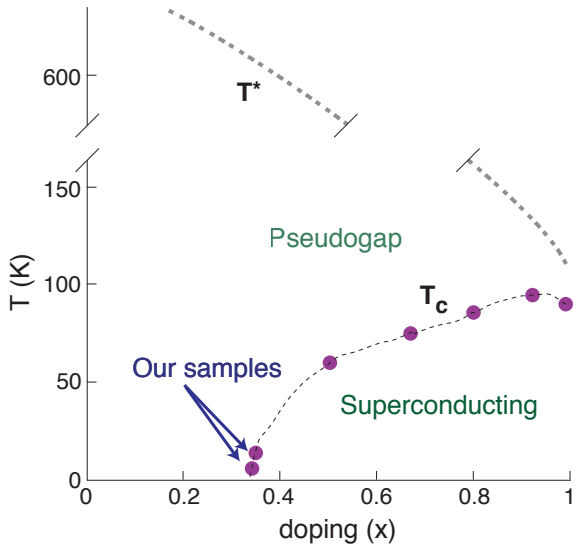

Figure 1.2: Phase diagram for $YBa_2Cu_3O_{6+x}$ showing the very underdoped crystals (with $T_c \cong$ 6-12K) used in the experiments described in this dissertation.

There is much speculation about the nature of the superconducting transition on

the underdoped side: is it a Kosterlitz-Thouless transition destroying phase coherence, a melting transition of stripes, a condensation of unpaired electrons that have lost their fermi statistics through spin-charge separation, or something else? Many theories of the cuprates make their strongest predictions at low doping where the superfluid density is small and competing orders, if they exist, may be nearby. Again, this is precisely because it is the nature of the normal state which is least understood, and superconductivity is sufficiently weak here that it may be easier to see through it to the underlying properties.

In the cuprate family, $YBa_2Cu_3O_{6+x}$ offers an excellent system to work with because it can be grown to very low dopings (BSCCO tends to flake apart when significantly underdoped). It is also stoichiometric in terms of the parent compound: doping is achieved by adding oxygen atoms to interstitial sites adjacent to the CuO planes rather than by substitution of the lanthanum for strontium as in LSCO. Similarly, it does not suffer from the inherent strontium inhomogeneity of BSCCO. It also does not exhibit the solid stripe phase at 1/8th doping that LSCO does – which may be related to superconductivity, or may be confounding. It also offers the unique opportununity to change the doping (even at fixed oxygen content) by thermal annealing which reorganizes the oxygen chains adjacent to the CuO layers.

Work by the UBC group of Bonn, Hardy, and Liang (Liang et al. 1998, 2001) has recently led to the development of techniques for growing 99.95% pure single crystals at extremely low doping (giving rise to T_c's in the range of 5-12K). These samples represent an important leap forward in the opportunity for condensed matter experimentalists to study a critical part of the cuprate phase diagram.

So far we've covered *what* we're studying. Now we'll turn to the techniques we use. We'll start with an introduction to the idea of scanning magnetic microscopy, and then cover the specific magnetic sensor used for the work in this thesis: the SQUID.

1.6 Scanning Magnetic Microscopy

The common theme for the measurements we do in the Moler lab is scanning magnetic microscopy. That is to say we measure the magnetic field (or field gradient, or flux – depending on the sensor used) on a grid of many points just above the surface of a sample. If you plot the resulting data as a colourscale image, with each measurement as a pixel, you get a picture of what the magnetic field is doing at the sample surface.

The scanning part of this setup is responsible for moving the magnetic sensor around to the different points over the sample surface. Most other scanning SQUID microscopes of which I am aware use some sort of mechanical scanner, usually a lever connected to a stepper motor. We use a piezoelectric S-bender scanner, after the design of Siegel et al. (1995), who developed this system for scanning Hall probes. This kind of scanner generally has a smaller range than can be obtained with mechanical scanners, but it is also much simpler, offers finer positioning control, and is less prone to vibration, hysteresis and creep. In addition, it is easy to allow for adjustment perpendicular to the scan plane (i.e. in the z direction if scanning is in x and y).

The basic component of the scanner is the S-bender (see Figure 1.3(a)) which consists of a piezoelectric bender with four electrodes – two on the upper half, two on the lower half. When a voltage is applied across the upper electrodes and the same voltage applied in the opposite polarity across the lower electrodes, the piezo bends in an 'S' shape. Note that the top and bottom of the S-bender remain parallel. To construct a scanner, you take two such S-benders in parallel, attach them at one end to the scan base, and at the other end to the secondary scan stage (see Figure 1.3(b)). These benders then move the secondary scan stage relative to the scan base in the x direction, and keep it parallel to the scan base. Attach a second pair of parallel S-benders to the secondary scan stage at one end, and at the other end (near the scan base) to the primary scan stage. These benders now move the primary scan stage relative to the secondary scan stage in the y direction.

The beauty of this design is that thermal contraction or expansion of the x piezo benders is compensated by that of the y benders, and vice versa, and thus does not

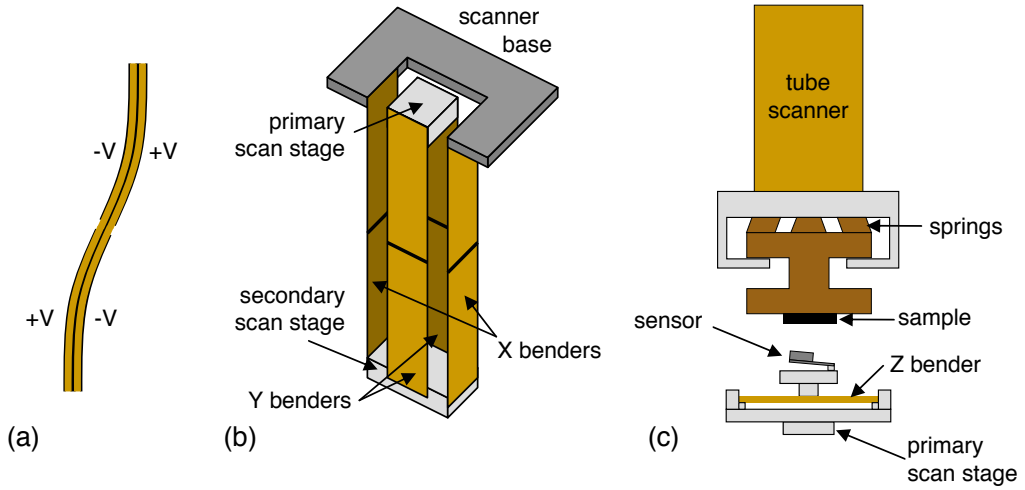

Figure 1.3: The S-bender scanner: (a) A piezoelectric S-bender. Applying voltages of opposite polarities across the top and bottom pairs of electrodes causes the piezo to bend in an 'S' shape. (b) Two pairs of S-benders form a scanner which is compensated against thermal expansion and keeps the scan stage parallel to the scan base while scanning. (c) Stick-slip coarse motion is implemented with a piezoelectric tube scanner which can move a sample puck over a range of 3mm relative to the sensor. The sensor and z-motion piezo are shown below; these connect to the primary scan stage shown in (b).

cause movement of the sensor. The primary scan stage is also kept parallel with the scan base at all times, preventing tilt of the sensor relative to the sample as a function of position. The height of the primary scan stage relative to the sample (assumed to be fixed relative to the scan base) does change very slightly with position, but this can be compensated for by attaching an additional piezo bender to the primary scan stage which moves the sensor in the z direction. In practice we usually control the z position of the sensor as a function of x and y position in order to scan in the plane of the sample, which is rarely in perfect alignment with the scan base.

Scan range depends on the length of the benders used, and the voltage applied – in practice this is limited by the breakdown voltage of the helium gas in the flow cryostat where our microscope is installed. At 4.2K we can achieve a scan range of

60μm by 60μm.

To extend the useful range of our scanner, our microscope is equipped with a coarse motion stage, which allows us to move the sample relative to the scanner so that we can image different areas of the sample. The coarse motion system is based on an inertial stick/slip technique. We mount our sample on a spring-loaded puck which is free to slide over a surface, except for the friction provided by the pressure of the springs (see Figure 1.3(c)). This assembly is attached to a piezoelectric tube scanner, and a sawtooth type voltage is applied. On the slow ramp of the sawtooth, the tube scanner moves the whole assembly in one direction. On the quick jump of the sawtooth, the tube scanner snaps back to its original position with sufficient force that the friction between the puck and surface is overcome, and the inertia of the puck keeps it in place at the new position. This process is repeated as necessary to move the puck. With this system we can move the sample over about 3mm relative to the sensor. More detail on the scanning microscope is available in Guikema (2004).

In any scanning magnetic microscopy, the spatial resolution of the resulting images is determined by the size of the sensor, and also by the height at which the sensor is scanned over the sample. If s is the size of the sensor and h the height above the sample, then the scan resolution is approximately given by $\sqrt{s^2 + h^2}$. Thus, it is very important to get your sensor as close to the sample as possible (at least within s). To help achieve this, our scanner is equipped with a capacitive deflection sensor that allows us to determine when the sensor touches the sample. By ramping the voltage on the z piezo of the scanner (causing the sensor to approach the sample) and noting the voltage at which touchdown occurs for at least three different xy positions, we can determine a plane parallel to the sample surface and scan in this plane to keep h minimized and fixed.

1.7 Why Scanning Magnetic Microscopy?

Though not all of the measurements reported in this thesis involve scanning, many do, and this is still the majority of what we currently do in the Moler lab. One of the many benefits of scanning is that humans are naturally visual creatures and can

assimilate a lot of detail in image-based data. It is extremely useful for giving a broad picture of what's going on, which is amazingly helpful when probing something unknown. For example, our discovery that we could create vortex-antivortex pairs and observe their subsequent annihilation was surely facilitated by our ability to look at pictures.

In more concrete terms, advantages of scanning techniques include the ability to investigate spatial inhomogeneity in samples, or to measure several different small samples (fabricated on the same surface) during a single cooldown (e.g. as we do with the Sn disks in Chapter 2). Scanning also allows one to measure samples which must be fabricated separately from the sensor – many previous SQUID measurements, for example, fabricated the sample in place on the SQUID, which can only be done if the fabrication process is compatible (see, for example, the references in the introduction of Chapter 2). Unlike many techniques in condensed matter, no damaging sample preparation is required. Imaging can be done on a film or a bulk sample with one reasonably good surface. Atomically flat surfaces (such as for STM or ARPES) or free standing, very thin samples (such as for TEM) aren't required.

Finally, the sensitivity of the sensors we have available is sufficient to discriminate fractions of $h/2e$, making this a useful tool for studying vortices (which I hope to have already convinced the reader is a worthwhile endeavour). Some of the uses to which we've put our scanning magnetic microscopes, considering only our work on the cuprates, include: manipulating individual vortices (SQUID susceptometer, MFM), measuring individual vortex pinning forces (SQUID susceptometer, MFM), measuring vortex size to put an upper limit on the penetration depth (Hall probe), measuring flux quantization (SQUID, Hall probe), establishing an upper limit on the energy of the proposed vison by measuring the absence of a vortex memory effect (SQUID), measuring spreading of vortices and apparent partial vortices which we believe to be indicative of split stacks of pancake vortices (SQUID, Hall probe). We have also used the same SQUID and Hall probe sensors to measure the dynamics of individual vortices in rings without the benefit of scanning, for various reasons, but found ourselves wishing to redesign the experiment to accomodate the scanning setup.

1.8 Magnetic Sensors

In our lab we use three different kinds of magnetic sensors for scanning magnetic microscopy: Superconducting QUantum Interference Devices (SQUIDs), Hall probes, and magnetically-tipped cantilevers. SQUIDs and Hall probes are both used on the scanning setup described in section 1.6, while the cantilevers are used in our Magnetic Force Microscope (MFM), where the scanning system is significantly different (Straver 2004).

The three sensors measure different quantities: the SQUID measures magnetic flux, the Hall probe measures magnetic field, and the MFM measures the gradient of the magnetic field convolved with the magnetic moment of the cantilever tip.

SQUIDs have the best flux sensitivity, but have a relatively large sensor area, giving them poor spatial resolution. Our SQUIDs are also based on niobium (Nb), which constrains their operating range to below the 9K superconducting T_c of Nb. Hall probes, on the other hand, can be made with a much smaller active area, giving better spatial resolution, and can operate to room temperature and above. The smallest Hall probes can achieve a flux sensitivity approaching that of SQUIDs, but Hall probes fabricated from a two-dimensional electron gas (2DEG, such as GaAs/AlGaAs, as we use) also exhibit 'switching noise' which is believed to come from changes in the electronic configuration of the silicon donor atoms, and this switching noise increases with decreasing probe size. The result is that small Hall probes can acheive excellent spatial and flux resolution, but require long averaging times. Switching noise is also extremely undesirable when looking at switching phenomena such as fluxoid dynamics in a superconducting ring, because the switching noise looks like the vortex jump signals you are trying to measure, and you can't average to get rid of it. Our SQUIDs have also been equipped with susceptometry coils from the outset, allowing them to apply local magnetic fields, while our Hall probes have not.

The MFM has much better spatial resolution than either SQUIDs or Hall probes, but the interaction between the magnetic tip and the sample can perturb the sample. In addition, interpretation of MFM data is much more complicated than that from SQUIDs or Hall probes because it is difficult to extract the magnetic field from the

measurement.

For a more detailed explanation of MFM, see Straver (2004); for details on Hall probes and a comparison of these magnetic sensors, see Guikema (2004).

1.9 SQUIDs

SQUIDs operate on the same principle of flux quantization as was discussed in section 1.1. In its simplest form, a SQUID consists of a loop of superconductor, broken by two weak links (Josephson junctions) which are strong enough that fluxoid quantization still applies to the loop (see Figure 1.4). Josephson junctions allow current to pass with zero voltage if that current is less than a critical current, I_c. If the current exceeds I_c, however, then a voltage develops across the junction. If you attach leads to the loop and pass a current (called the bias current) in parallel across the Josephson junctions so that they are at their critical currents, then any excess current will lead to a voltage across the SQUID.

If field is applied so that external flux enters the loop, then the loop must compensate by generating a circulating current to maintain the fluxoid quantization condition. This circulating current will cause one of the Josephson junctions to exceed its critical current, and a voltage, V_S, will develop across the SQUID. This voltage is measured and sent into a feedback system that sends a current, $I_{\rm fb}$, through a loop whose mutual inductance to the SQUID, $L_{\rm fb}$, is known. The feedback flux $\Phi_{\rm fb} = L_{\rm fb} I_{\rm fb}$ required to keep V_S minimized is equal to the applied flux through the SQUID that generated the signal.

The SQUIDs we use have several modifications to make them suitable for scanning. Since spatial resolution is important, we need a SQUID which has the smallest possible loop as close as possible to the sample. We achieve this by drawing off part of the SQUID loop in a long arm with a small 'pickup loop' at the end. The arm is magnetically shielded so that fields near the pickup loop only penetrate through the pickup loop. The substrate on which the pickup loop sits is then polished to a point so that when the point is in contact with the sample, the pickup loop is a within a few microns (usually 0.5μm-2μm, depending on the angle between the SQUID and

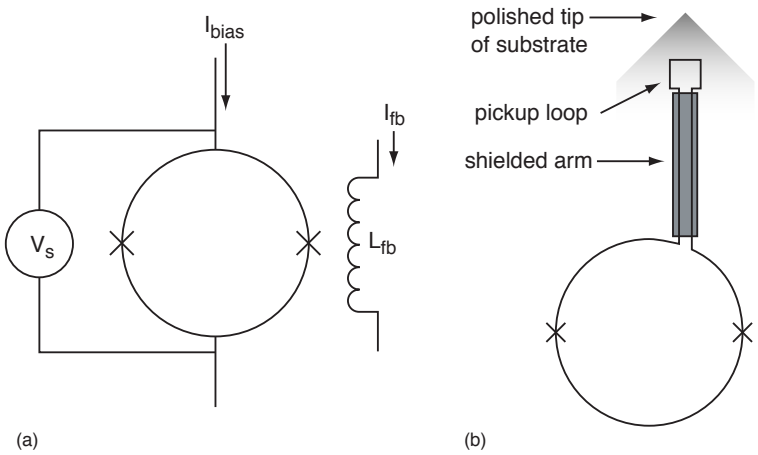

Figure 1.4: SQUID schematic: (a) A SQUID is formed from a superconducting loop broken by two Josephson junctions (marked with $\times$). A bias current holds the junctions at their critical currents. Flux through the SQUID loop causes a circulating current to maintain fluxoid quantization, which causes a voltage V_S across the junctions. A feedback system cancels the applied flux and keeps V_S minimized. (b) For scanning applications, a small pickup loop is connected to the main SQUID loop via a magnetically shielded arm. The substrate is polished to a point near the pickup loop.

the sample) of the sample surface. Fields from the surface of the sample are detected by the pickup loop, while the rest of the SQUID is far away and picks up only any homogeneous background field, which is irrelevant for the measurement. Further details on the design of our SQUIDs are given in Chapter 2.

Chapter 2

Scanning SQUID Susceptometry

2.1 Introduction

Superconducting QUantum Interference Device (SQUID) microsusceptometers (Ketchen et al. 1989, 1984) have been used to measure the susceptibility of a 5μm tin particle (Ketchen et al. 1984) and of iron nanotowers (McCord and Awschalom 1990), to perform Nuclear Magnetic Resonance on a 50μm platinum particle (Narasimhan et al. 1994), and for picosecond magnetic spectroscopy of dilute magnetic semiconductors (Awschalom and Warnock 1989). With a *scanning* microsusceptometer it would be possible to make measurements on samples which cannot be fabricated within the pickup loop, to look at several mesoscopic objects in a single cool-down, or to locally characterize macroscopic samples that may be mesoscopically inhomogeneous. In this chapter I describe the scanning microsusceptometer measurements of the susceptibility of 3μm granular tin disks.

2.2 Design of the Susceptometer and Cryogenic Scanner

The SQUID susceptometer is similar to the one designed by Ketchen et al. (1984), but modified for scanning (Fig. 2.1). The susceptometer's primary pickup loop (8μm by 8μm square) captures flux over the region of interest near the sample. A current,

$I_{\rm fc}$, through an octagonal field coil is used to apply a local field. The same current runs through a secondary field coil around a counterwound secondary pickup loop 0.6mm away, canceling the flux from the applied field. Thus, the net flux coupled into the SQUID is the response of the sample to the applied field. A center-tap between the two field coils is used to compensate for slight differences in their mutual inductance to the pickup loops, such as might be caused by variations in the geometry due to the limitations of the fabrication process. The susceptometer was fabricated using a multilayer Nb/AlO_x/Nb process at HYPRES, a commercial superconducting electronics foundry (HYPRES Inc.). The pickup loops are fabricated as small as the HYPRES design rules allow, and the process tolerances give an inductance mismatch of less than about 6%, or 0.3pH. A similar inductance mismatch would be expected in pickup loops fabricated by other processes, including submicron pickup loops fabricated by electron beam lithography. The center-tap is most important for relatively large applied local fields. At the maximum applied local field, a 6% inductance mismatch leads to a net flux of $8.25\Phi_0$ through the SQUID. Nulling this mismatch signal with the center-tap allows us to measure weak responses in relatively strong applied local fields.

The susceptometer chip is polished to a point close to the primary pickup loop (Fig. 2.1(b)). It is then mounted on a conducting cantilever which forms one plate of a variable capacitor used to determine when the susceptometer touches the sample surface. The variable capacitor and susceptometer are mounted on a piezoelectric scanner in a variable temperature flow cryostat. A passive impedance-matching circuit is also mounted in the cryostat to match the low output impedance of the SQUID to the room temperature preamp. The useful temperature range runs from 1.5K, the base temperature of the cryostat, to slightly below the 9K T_c of the Nb in the SQUID. The scanning system consists of an S-bender scanner (Siegel et al. 1995) with a range of 60μm by 60μm, and stick-slip coarse motion with a 3mm range.

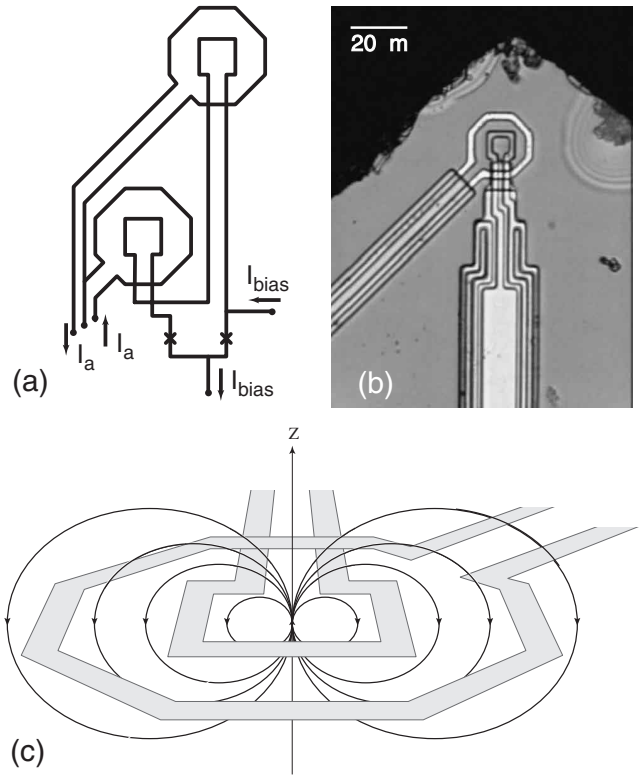

Figure 2.1: (a) Schematic of the SQUID susceptometer. Two drive coils (octagonal) are used to couple equal and opposite amounts of flux into two pickup loops (square). The sample changes the amount of flux coupled into the primary pickup loop. (b) Photograph of primary pickup loop with shielded leads and field coil. Spatial resolution of the susceptometer is limited by the size of the pickup loop (8μm by 8μm). (c) Diagram of pickup loop and field coil over a dipole. The SQUID detects the net flux through the pickup loop. The field applied by the field coil is not shown.

2.3 Model for Measurement of Induced Dipole

We tested the system by imaging the diamagnetic response of individual small (3μm diameter) superconducting disks. Each disk may be closely approximated by an induced dipole, allowing us to test models of the resolution function of our susceptometer for future deconvolution. The disk is modeled as an induced dipole of magnitude $m_z \propto H_{az}$, where H_{az} is the field applied by the field coils and the volume susceptibility dm_z/dH_{az} is an unknown. For simplicity, we model the field coil as a circle of radius $R_{\rm fc} = 10.5\mu$m. With the disk located at a position $\vec{r}_0 = (x_0, y_0, h)$ from the center of the field coil and pickup loop, the z-component of the field at the center of the disk is

$$H_{az}(\rho_0, h) = \frac{\mu_0 I_{\rm fc}}{4\pi R_{\rm fc}} \int_0^{2\pi} \frac{\left(1 - \frac{\rho_0}{R_{\rm fc}} \sin\phi\right) d\phi}{\left(1 + \frac{\rho_0^2 + h^2}{R_{\rm fc}^2} - 2\frac{\rho_0}{R_{\rm fc}} \sin\phi\right)^{3/2}}, \tag{2.1}$$

where $\rho_0 = \sqrt{x_0^2 + y_0^2}$, and the integral is solved numerically.

The flux from the dipole which is coupled into the pickup loop, modeled as a square of side s, is

$$\Phi_s(\vec{r}_0) = \frac{\mu_0}{4\pi} \frac{dm_z}{dH_{az}} H_{az} \int_{-\frac{s}{2}}^{\frac{s}{2}} \int_{-\frac{s}{2}}^{\frac{s}{2}} \left(\frac{3h^2}{r^5} - \frac{1}{r^3}\right) dxdy, \tag{2.2}$$

where $r = \sqrt{(x - x_0)^2 + (y - y_0)^2 + h^2}$. The susceptibility dm_z/dH_{az} and height h are free parameters of the model.

2.4 Characterization of Tin Microdisks

The test sample consisted of granular tin disks 3μm in diameter, with a typical grain size of a few hundred nanometers, spaced 30μm apart on a silicon substrate. The unpatterned film had a critical temperature $T_c \simeq 3.8$K and transition width $\Delta T_c \simeq 0.34$K, as measured with a commercial magnetometer in a 50G applied field.

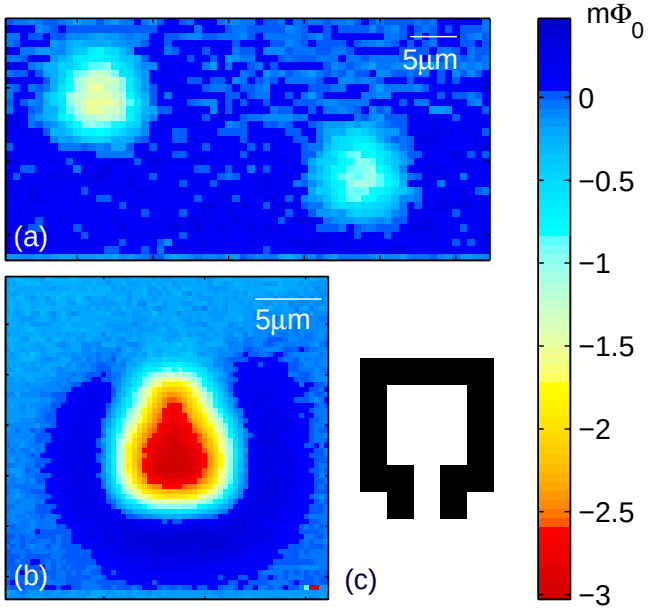

Figure 2.2: (a) Scanning susceptometry image of two 3μm tin disks at 2.3K. While the pickup loop is over a disk, the signal from the field coil is suppressed by the addition of the diamagnetic response of the superconducting disk. The difference in signal between the two disks is attributed to their granularity. (b) Scanning susceptometry image of a 3μm superconducting tin disk at 1.8K. The leads to the pickup loop are responsible for the keyhole shape. (c) Diagram of pickup loop drawn to the same scale as (b).

In contrast, with the scanning microsusceptometer, the transition width of an unpatterned region of the film measured in a 0.1G applied field was found to be 0.1K.

The susceptometry images shown in figures 2.2 and 2.3 were taken with $I_{\rm fc} = 440\mu$A rms at 100Hz, inducing an applied field $H_a = 0.23$G rms in the center of the pickup loop, about 1% of the maximum field we can apply with these field coils. The in-phase 100Hz component of the total flux through the SQUID, Φ_s, is shown in the colorscale images (Fig. 2.2). Figure 2.2(a) shows an image of two disks, which have peak signals differing by 4%. We attribute this difference to the granularity of the sample. Figure 2.2(b) shows an image of a single 3μm diameter tin disk. The protuberance on the top is due to the disk passing under the leads (Fig. 2.2(c)) of

the pickup loop.

Figure 2.3 shows a fit to data from a cross section of an image of a single disk at $T = 1.8$K. The best fit is obtained for $h = 3.0 \pm 0.1\mu$m and $dm_z/dH_{az} = (-3.65 \pm 0.07) \times 10^7 \mu_B$/G. The quoted errors include both the statistical and the systematic deviation of the data from the fit. The systematic deviation may be attributed to the simplified model, which neglects the shielded leads and the finite size of both the disk and the susceptometer wires. These assumptions begin to fail at smaller heights as the disk gets close to the susceptometer wires.

The net flux through the pickup loop is maximized when the height above the dipole is minimized and the dipole sits in the corner of the loop (see Fig. 2.1(c)). We have observed this signal enhancement in images taken at $h = 1.4\mu$m. Although measurements at lower heights could lead to greater precision, accurate determination of the dipole moment would require better modelling in this regime. For example, we have also modeled the disk as a flat cylinder (Clem and Sanchez 1994) in the case where it lies in the plane of the pickup loop ($h = 0$), at the loop center. These calculations disagree with the dipole model by 4%, and the disagreement would be worse away from the center of the pickup loop.

In the London model in the limit of zero penetration depth, a superconducting disk of diameter R_d has an induced dipole moment (Clem and Sanchez 1994; Landau and Lifshitz 1984, p.185)

$$m_z = -\frac{4\pi}{\mu_0}\frac{2R_d^3}{3\pi}H_{az}. \tag{2.3}$$

For $R_d = 1.5\mu$m, this gives a theoretical value of $dm_z/dH_{az} = -7.9 \times 10^7 \mu_B$/G. Various disks had measured susceptibilities ranging from -3.5×10^7 to $-5.5 \times 10^7 \mu_B$/G. The ability to measure many mesoscopic objects individually is one of the strengths of the scanning microsusceptometer.

The temperature dependence of the susceptibility of a tin disk, from fits of cross sectional data shown in figure 2.4(b), is shown in figure 2.4(a), along with the susceptibility of an unpatterned region of the film, also measured with the scanning microsusceptometer. The measurements were made with an applied current $I_{\rm fc} = 200\mu$A rms at 100Hz, inducing an applied field $H_{az} = 0.1$G rms in the center of the pickup

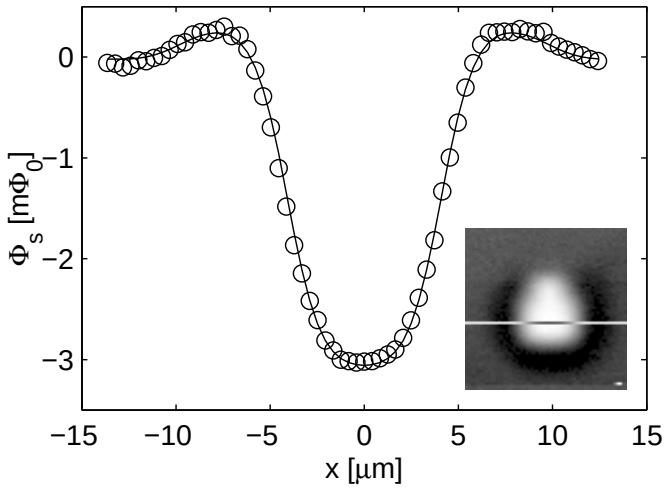

Figure 2.3: Cross section of susceptometry image (circles) of a tin disk. The solid line is a fit to the data with the pickup loop modeled as a square, the field coil as a circle, and the disk as a dipole. The susceptibility, $dm_z/dH_{az} = (-3.65 \pm 0.07) \times 10^7 \mu_B/\mathrm{G}$, and the height of the pickup loop above the disk, $h = 3.0 \pm 0.1 \mu\mathrm{m}$, are free parameters. Inset: Image indicating location of cross section.

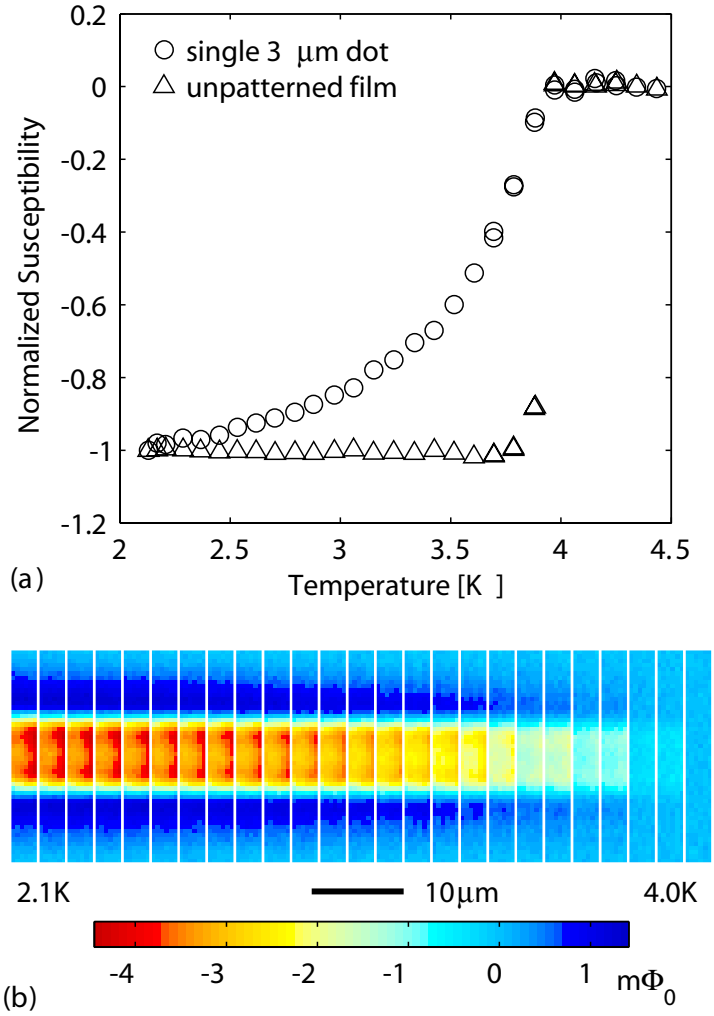

Figure 2.4: (a) Susceptibility of a 3μm tin disk as a function of temperature, and susceptibility of an unpatterned region of the tin film, both measured with the scanning SQUID microsusceptometer. Statistical errors are about 2%. Each curve is normalized to $T = 2.1$K. The susceptibility of the disk at 2.1K is $5 \times 10^7 \mu_B$/G. (b) Susceptometry images of the disk as a function of temperature (with background subtracted). The diamagnetic response from the disk appears as it cools through T_c and increases (from right to left in the figure) as the temperature drops. Fits to cross sections of this data were used to generate the graph in (a). (Images above 4K not shown.)

loop. The linearity of the susceptibility was checked within 0.1% for applied fields up to 0.12G on this disk and up to 1.15G on another disk. The transition of the disk is markedly broader than the transition of the unpatterned film. We attribute the broader transition of a single disk to the temperature dependent penetration depth of the tin and the small size and granularity of the disk.

2.5 Figures of Merit and Applications

The SQUID noise is $\delta\Phi_n = 5 \times 10^{-5}\Phi_0/\sqrt{\text{Hz}}$ under typical conditions, which gives a spin sensitivity of $\delta m = 1 \times 10^5 \mu_B/\sqrt{\text{Hz}}$ for our geometry. The spin sensitivity could be improved in three ways. First, the intrinsic noise level of the SQUIDs outside the scanning system is $3 \times 10^{-6}\Phi_0/\sqrt{\text{Hz}}$ or lower, indicating that our flux sensitivity could be improved by an order of magnitude. Second, the spin sensitivity could be increased by decreasing the separation between the pickup loop and the sample, which is presently limited by the wire bonds to the SQUID chip and by the SiO_2 layer covering the pickup loop. The signal could be increased by a factor of 4 by placing the dipole in the corner of the pickup loop and decreasing the height from $h = 3\mu$m to $h = 0.5\mu$m. Third, the spin sensitivity could be improved by fabricating susceptometer SQUIDs with smaller pickup loops (Ketchen et al. 1989). The spatial resolution could be improved with smaller pickup loops and, at least in principle, by applying deconvolution algorithms to future images using the measured geometry of the pickup loops.

Possible applications of the scanning SQUID microsusceptometer include measurements of the penetration depth in superconductors, studies of persistent currents in mesoscopic electronic systems (Chandrasekhar et al. 1991), searches for trace amounts of superconductivity or magnetism in novel materials (Scott et al. 1997), and studies of nanomagnets.

Chapter 3

Vortex Manipulation

3.1 Introduction

The ability to manipulate single vortices in a superconductor is of interest for the study of pinning sites in superconducting materials, and to control vortex configurations in superconducting devices. This chapter describes a method for locally applying a controlled, tunable force to a vortex at the surface of a superconductor. We demonstrate this technique by reversibly moving individual vortices at the surface of a single crystal of $YBa_2Cu_3O_{6.354}$. The force is provided by a locally applied magnetic field from a current-carrying coil integrated into a scanning Superconducting QUantum Interference Device (SQUID), as described in chapter 2. The applied field induces screening currents in the sample, thereby exerting a Lorentz force on the vortex.

Moving single vortices in a superconductor has been achieved previously in limited cases. Currents in cross-strip Josephson junctions have been used to move part of a vortex in one of the superconducting layers reversibly between pinning sites, determining the vortex position from junction diffraction patterns (Hyun et al. 1987, 1989; Li et al. 1991; Li and Finnemore 1991; Sok and Finnemore 1994; Kouzoudis et al. 1999; Breitwisch and Finnemore 2000). Plourde and Van Harlingen (Plourde 2000) observed that the tip of a scanning SQUID microscope would irreversibly sweep vortices out of its path in amorphous MoGe films, but not in Nb films, though the exact

mechanism is not yet understood. The technique reported here should be viable for many materials and sample types, provides *in situ* images of the vortex configuration, does not depend on fabricating a Josephson junction out of the sample material, and provides a tunable local force.

3.2 Samples

Single crystals of very underdoped $YBa_2Cu_3O_{6.354}$ were chosen as a test material in anticipation of relatively low pinning forces. Two test samples were grown by Liang et al. (1998, 2001) with T_c's of 11K and 12K and transition widths of about 2K. Both crystals were approximately 1mm by 1mm in the *ab*-plane and 50μm thick along the *c* axis. The sample thickness is simply a product of the growing technique. As discussed below, quantitative interpretation of the results would be simpler in samples that are thinner than the penetration depth. The samples were imaged with the *ab*-plane parallel to the sample surface. The $T_c = 11$K sample was subsequently re-annealed to create a third sample with $T_c = 6$K and a 3K transition width. Vortex motion was demonstrated in all three samples. Vortex-antivortex pairs were created in the $T_c = 11$K sample and in the $T_c = 6$K sample.

3.3 System

The apparatus used for this experiment is the same scanning SQUID microscope described in chapter 2. The entire cryostat is surrounded by triple-layer mu-metal shielding which shields out the Earth's magnetic field. The residual field inside the microscope is sufficiently small ($\sim$ 20mG) that cooling below T_c gives a sparse arrangement of vortices within the field of view of the scanning SQUID.

The SQUID's 8μm by 8μm square pickup loop is surrounded by a concentric octagonal field coil, 21μm across (Fig. 3.1(a)). The field coil is used to apply local fields to the sample, the maximum field being determined by its critical current, which is 55mA at 4.2K. The pickup loop and field coil are within 2° of parallel to the sample at a height of 1-2μm above the surface. With the field coil at a height of 2μm, our

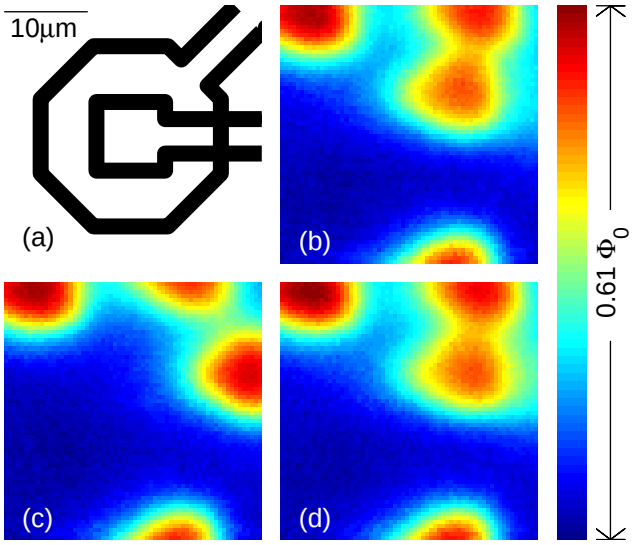

Figure 3.1: Moving vortices. (a) Sketch of the field coil (octagonal) and pickup loop (square) of the scanning SQUID on the same scale as the images. (b) through (d) show movement of a single vortex between pinning sites in a $T_c = 11$K $YBa_2Cu_3O_{6.354}$ crystal at $T = 3.4$K. (b) Scanning SQUID image of the initial configuration of vortices. (c) Same area after a current $I_{fc} = -3$mA has been passed through the field coil for 10s with the SQUID held stationary over the centre of the image. The two vortices in the top right corner of the scan area have moved. (d) After running a current $I_{fc} = 4$mA through the field coil with the SQUID at image centre. Both vortices have moved back to their original locations.

maximum current corresponds to a force of ∼5pN on a vortex directly under one edge of the coil, according to a model described below.

3.4 Moving Vortices

To move a vortex, current was applied through the field coil for 10 seconds (with 4s linear ramp-up beforehand and 4s ramp-down after) and the area was re-scanned to see if any of the vortices had moved. The current was increased incrementally until a scan showed that a vortex had moved. The $T_c = 11$K and 12K samples required 4-6mA to move a vortex, depending on location and vortex configuration, and the $T_c = 6$K sample took 0.2mA. Subsequent scans showed the vortex to be stable in its new location for at least several hours. The process was repeated with current passed

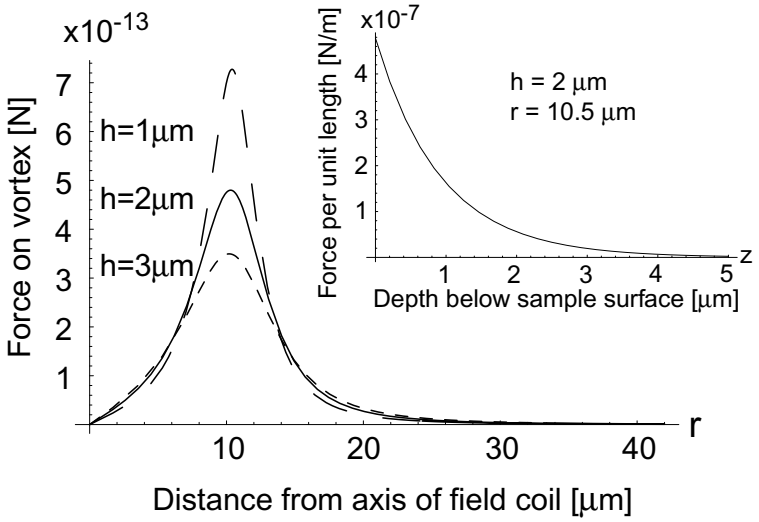

Figure 3.2: Force on a vortex, assuming $\lambda_{ab} = 1\mu$m, as a function of the distance of the vortex from the axis of the field coil, evaluated for a current $I_{\rm fc} = 5$mA through a field coil of radius $r_{\rm fc} = 10.5\mu$m at heights $h = 1, 2, 3\mu$m above the superconductor surface. A positive current, $I_{\rm fc}$ counterclockwise from above, and vortex flux along the $\hat{z}$ direction are assumed. *Inset*: Force per unit length on the vortex as a function of depth below the surface of the sample, evaluated for a vortex directly beneath the field coil wire ($r = r_{\rm fc}$).

in the reverse direction until the vortex moved again. Once the currents necessary to move the vortex in each direction were established, we moved the vortex back and forth many times and always found it to move between the same two approximate positions (Fig. 3.1). Vortex pinning potentials are expected to vary on the scale of the coherence length, so we would need to improve our effective spatial resolution to resolve individual pinning sites and map out pinning potentials.

3.5 Force Calculations

To determine the force applied on the vortex, we first calculate the magnetic fields within the sample due to the field coil based on the method of Kogan et al. (1993); Kogan (2003), which involves solving the London equations by Fourier transformation in the x and y directions. The screening currents are determined from these fields via

Maxwell's equation $\mathbf{J} = \nabla \times \mathbf{H}$, and the Lorentz force exerted on the vortex follows from $\mathbf{F} = \Phi_0 \int_{-\infty}^{0} \mathbf{J} \times \hat{z}\, dz$ where $\mathbf{J}$ is evaluated at the x-y location of the vortex core. We have assumed that the vortex is a rigid cylinder along the z axis, ignoring the possibility of bending. The force is integrated along the length of the vortex. Treating the field coil as a circular current loop of radius $r_{\rm fc}$ and carrying current $I_{\rm fc}$, the resulting total force on the vortex is in the radial direction from the axis of the field coil, and may be written:

$$F_r(r) = -\frac{\Phi_0 I_{\rm fc} r_{\rm fc}}{2\lambda_{ab}^2} \int_0^\infty \frac{dk\, k e^{-kh}}{q\,(q+k)} J_1(kr_{\rm fc}) J_1(kr) \tag{3.1}$$

where $q = \sqrt{\lambda_{ab}^{-2} + k^2}$, λ_{ab} is the in-plane penetration depth, Φ_0 is the superconducting flux quantum, and h is the height of the field coil above the sample. This equation can also be derived by the method of Clem and Coffey (1992) when the penetration depth is isotropic in the ab-plane, as we assume here. A graph of the result is shown in Figure 3.2. We have used the following values in the calculation: $I_{\rm fc} = 5\text{mA}, \Phi_0 = 2\text{fTm}^2, \lambda_{ab} = 1\mu\text{m}, r_{\rm fc} = 10.5\mu\text{m}$. The approximate value for λ_{ab} is consistent with Hall probe studies of isolated vortices in the $T_c = 12\text{K}$ sample (Wynn et al. 2001). The force varies by a factor of 2 for λ_{ab} ranging from 0.1μm to 2μm. $h = 2\mu$m is a typical value for the height of the SQUID above the sample. With these assumptions, the total force on a vortex required to observe vortex motion was ~ 0.5pN in the $T_c = 11\text{K}$ and 12K samples.

3.6 Conclusions

In addition to the advantages discussed earlier, this technique has two disadvantages. First, it does not provide an image of the vortex below the surface of the superconductor. The two-dimensionality of the information complicates the interpretation of studies in thick films and bulk samples, where bending of the vortices may occur. This should not affect studies of thin films. Second, the field coil applies a force over many square microns. It can only be used to manipulate a single vortex

when the vortex is sufficiently isolated. This limitation could be reduced by designing different field coils. Scaling the field coil and pickup loop to smaller dimensions would result in more localized applied fields, as well as improving the resolution of the SQUID for imaging. The SQUIDs for this study were commercially fabricated according to (HYPRES Inc.) design rules, which at the time limited feature size to 1-2μm – resulting in an 8μm pickup loop. It is important for the pickup loop to be fabricated with a process that allows the pickup loop leads to be properly shielded (Ketchen and Kirtley 1995). It would, however, be possible to subsequently fabricate a submicron field coil on the SQUID chip, and apply forces on a submicron scale.

For SQUIDs with a minimum detectable flux change of $\delta\Phi$, the minimum detectable vortex motion is given by $\delta x = (d\Phi/dx)^{-1}\delta\Phi$. For a vortex moving near the edge of an 8 micron pickup loop, the change in flux with the vortex position is $d\Phi/dx \approx 0.1\Phi_0/\mu$m. In principle, it is possible to determine a vortex's position on the Ångstrom scale, even with the existing 8 micron pickup loops.

Chapter 4

Vortex-Antivortex Annihilation

4.1 Introduction

In addition to moving single vortices back and forth, we can also use the field coil on our scanning SQUID susceptometer to create a vortex-antivortex pair (i.e. a pair of vortices with opposite flux) at the surface of the superconductor where none was before. Because a scanning SQUID only images the surface flux, we note it is possible that the vortex-antivortex pair forms a U-shaped tube of flux inside the sample instead of penetrating all the way through – we would be unable to distinguish such configurations. These vortex-antivortex pairs generally persist for some time, then annihilate each other. In this chapter we discuss the technique we use to create the pairs, and report the result of measurements of pair lifetimes and observations of several ways in which the pairs annihilate. We find that the characteristic vortex pair lifetime is a strong function of temperature, as might be expected for annihilation by thermally activated depinning. Observation of pair annihilations shows that pairs typically encounter several intermediate pinning sites before they annihilate, indicating that the pinning landscape in this material is complicated. Two possible naïve models, thermally activated annihilation out of a double-well potential or a mesoscopically uniform pinning distribution, are insufficient.

4.2 Samples

Our sample is a very underdoped single crystal of $YBa_2Cu_3O_{6.354}$ (Liang et al. 2002), with approximate dimensions 1mm by 1mm and about 4μm thick along the c-axis, as measured under a microscope. T_c for this sample is about 12K. We have also created vortex-antivortex pairs in another crystal at two different oxygen configurations ($T_c = 11$K, subsequently re-annealed to 6K), though we we did not make a systematic study of pair lifetimes in those samples.

4.3 Making Pairs

To make a vortex-antvortex pair, we cool the sample in zero field and take an image to make sure our field of view is free of vortices. We then park the SQUID in the centre of the scan area and run a current $I_{\rm fc}$ through the field coil for 10s (with 4s ramp up and 4s ramp down for a total of 18s). We then scan again to see if we have created a vortex-antivortex pair. If not we repeat the current ramp with a larger $I_{\rm fc}$.

When a sufficient $I_{\rm fc}$ has been applied, a vortex pair will be created at some location around the field coil, presumably at a weak point (depressed ρ_s?) in the superconductor near the location of the applied field. One vortex will be just inside the field coil, the other just outside, and they will have opposite flux, one into the sample, the other out of the sample, as determined by the direction of the field induced by the current in the field coil, $I_{\rm fc}$ (Fig. 4.1).

Note that we never saw vortex pairs created far from the field coil. It would be interesting to work in a system where ξ is very large so that there should be no especially weak points of the superconductivity on a scale smaller than the field coil. Other possibilities for breaking the symmetry could be a tilted SQUID which puts part of the field coil closer to the sample than other parts. For extremely large applied currents $I_{\rm fc}$ we definitely created many vortex pairs around the field coil (Fig. 4.2).

We found that vortex-antivortex pairs can be created with applied fields just slightly greater than that necessary to move vortices, as discussed in chapter 3. Typical currents required to create a pair in the $T_c = 12$K sample are 15-23mA, depending

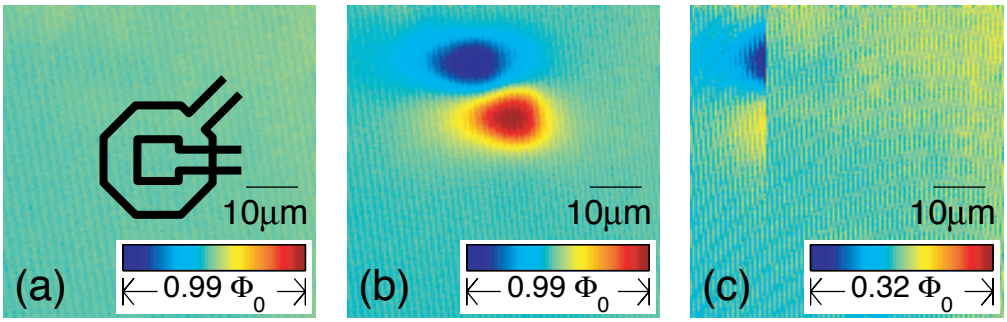

Figure 4.1: Creation and annihilation of a vortex-antivortex pair. (a) Image of a vortex-free region of a $YBa_2Cu_3O_{6.354}$ crystal with $T_c = 6$K at $T = 2.7K$. A schematic of the SQUID field coil (octagon) and pickup loop (square) is superimposed. The SQUID is held stationary while a current $I_{\rm fc} = 0.8$mA is applied counterclockwise through the field coil for 10s, creating a downward magnetic field outside the octagon and an upward field inside. (b) After the current $I_{\rm fc}$ is turned off a SQUID magnetometry scan reveals a vortex-antivortex pair created by the field from the field coil. (c) Two scans (∼130s) later, we see the vortex-antivortex pair annihilating during the scan. Scan raster direction is left-to-right, the pair annihilates between one scan line and the next. The colour scale has been amplified in (c) for clarity.

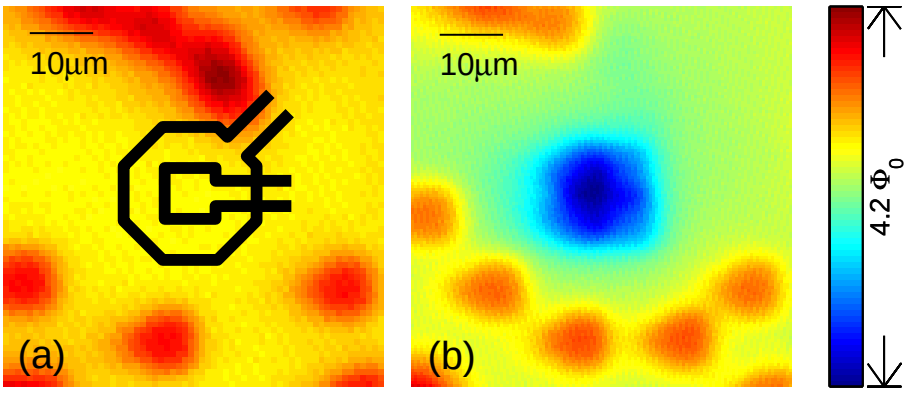

Figure 4.2: Multiple pairs can be created around the field coil with larger applied currents $I_{\rm fc}$. This pair of images was taken at $T = 3.5$K in a $T_c = 6$K sample, using a current $I_{\rm fc} = 15$mA.

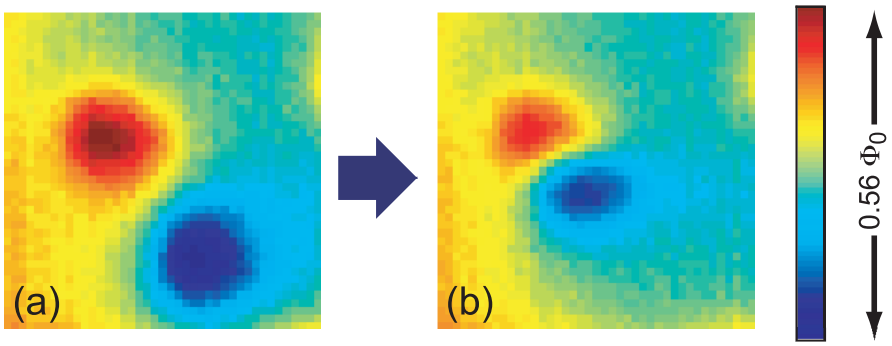

Figure 4.3: A vortex-antivortex pair pauses at an intermediate pinning site before annihilating. (a) The initial configuration of the pair. (b) The lower vortex has moved from its original pinning site to an intermediate site closer to its partner vortex. Because the characteristic length scale for the pinning potential is the coherence length ξ, there are generally many pinning sites available in between vortex pairs created by our field coil.

on the location and the height above the sample. In the $T_c = 11$K, 6K samples, creating pairs required currents $I_{\rm fc}$ of about 7mA, 0.8mA, respectively. Variations in height of the SQUID can result in large changes to the current $I_{\rm fc}$ required to generate a pair. We have been able to change $I_{\rm pair}$ by about a factor of two due to change in height, though we never pursued this systematically. Variation from place to place was fairly small. Variation from one cooldown to the next was sometimes large (up to an overall factor of four), probably dependent on the height due to good or poor alignment of the SQUID with the sample, possibly also affected by room temperature annealing of the sample.

Once we have created a pair, we scan continuously to see when the vortex and antivortex annihilate (Fig. 4.1). Even at a given temperature, the pair annihilation time ranged from tens of seconds to more than 24 hours. Instead of simply annihilating, some pairs moved closer on a time scale of minutes, and then persisted in their new locations (Fig. 4.3). Presumably, the pair moves together until both members of the pair are stuck in local pinning potentials that exceed the vortex-antivortex attraction. In a simpler geometry, such as a film that is thin compared to the penetration depth, this behavior could be used to quantitatively determine the pinning force. The thickness of our samples makes this too complicated for our situation since it is possible

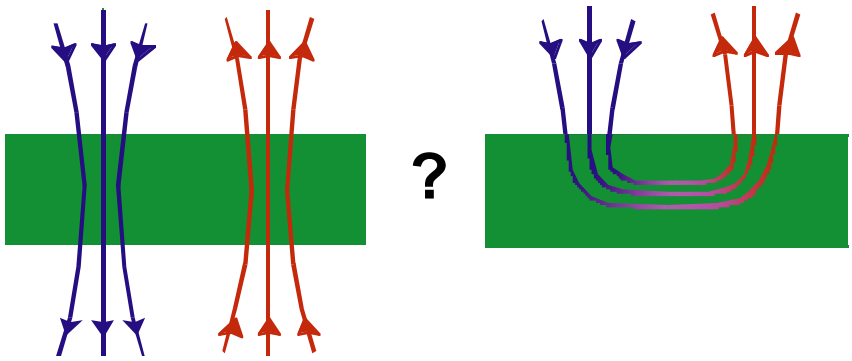

Figure 4.4: Is it a pair or a loop?

that the vortex pairs did not penetrate all the way through the crystal, but instead formed a U-shaped tube of flux within the crystal (Fig. 4.4).

Instead of simply waiting for vortex-antivortex pairs to annihilate on their own, they could also be induced to do so by applying a field with the field coil opposite in sense to that used to create the pair (Fig. 4.5). Generally, the magnitude of the field required to induce annihilation of the pair was much less than that required to create it.

4.4 Pair Lifetime Measurements

To measure pair lifetimes, we create a pair and immediately park the SQUID over one member of the pair. We can then record the flux measured by the SQUID as a function of time and detect the pair annihilation event as a rapid jump in the flux signal to the background flux level (i.e. the flux with no pair). Fig. 4.6 shows two examples, (a) and (b), obtained at different sites in the sample. This measurement is repeated many times and the resulting data used to build a histogram of pair lifetimes for the given temperature, T_{ref} (Fig. 4.6(c)).

To measure pair lifetimes at other temperatures while ensuring the same initial

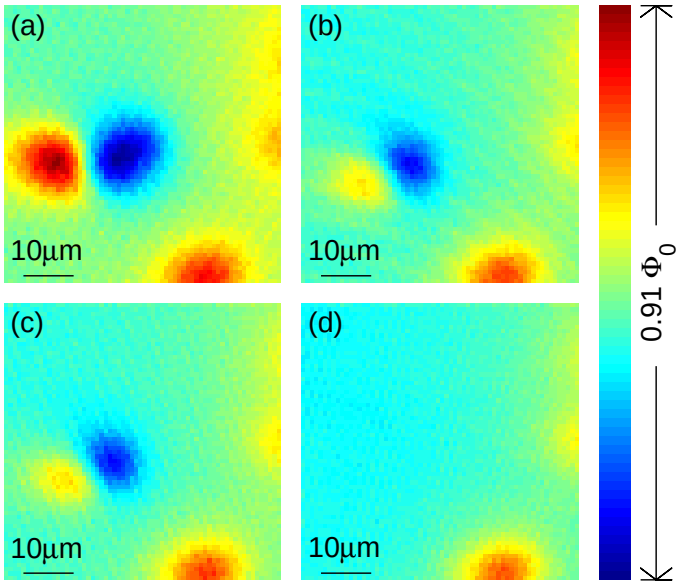

Figure 4.5: Vortex pair annihilation sequence at $T = 5.25$K induced by an applied field from the field coil. (a) The vortex pair created by a current $I_{\rm fc} = -21$mA through the field coil. (b) The same pair after a reverse current $I_{\rm fc} = +10$mA has been applied through the field coil. The vortices have moved to new pinning sites closer together. (c)After a reverse current $I_{\rm fc} = +11$mA is applied there is no further change. (d) After a reverse current $I_{\rm fc} = +12$mA the pair annihilates.

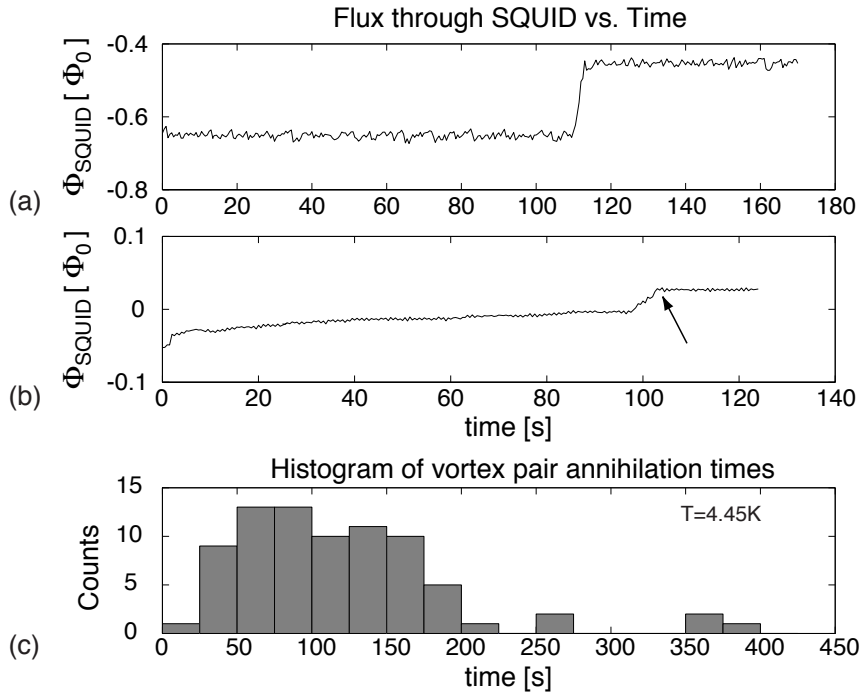

Figure 4.6: (a) Annihilation event: The pickup loop of the scanning SQUID is placed over one member of a vortex-antivortex pair. The flux through the pickup loop changes abruptly to the background flux level when the pair annihilates. (b) As in (a), but the annihilation event (indicated with an arrow) is preceded by gradual changes in flux associated with the vortex moving through intermediate pinning sites. (c) Histogram of vortex pair lifetimes at $T = 4.45$K at a single location obtained from a sequence of flux vs. time graphs with clear, simple annihilation events as in (a).

conditions, we create the pairs at the *same* initial temperature, $T_{\rm ref}$, position the SQUID and begin the flux vs. time measurement, then quickly heat to the desired measurement temperature $T_{\rm meas}$ and watch for the annihilation event. Heating from $T_{\rm ref} = 4.16$K to $T_{\rm meas} = 4.60$K takes a few seconds, reaching 4.64K by 10s and leveling off at 4.65K by about 20s. Similarly for the lower measurement temperatures: $T_{\rm meas} = 4.20$K is reached from $T_{\rm ref}$ within a few seconds, 4.25K within 10s, and 4.26K by 20s; $T_{\rm meas} = 4.50$K is reached from $T_{\rm ref}$ within a few seconds, 4.54K within 10s, and 4.55K by 20s.

4.5 Results & Discussion

A simple model consisting of vortices with opposite flux separated by a uniform potential barrier annihilating by thermal activation over the barrier would lead to a pair lifetime $\tau(T) = \tau_0 \exp(U/k_B T)$ where U is the barrier height. None of the sites we measured exhibited pair annihilation behaviour simple enough to be appropriately described by this model. Most sites were much more complicated, and the vortices appeared to either hop or creep through a sequence of intermediate pinning sites before finally annihilating (e.g. Fig. 4.7(b)). This is not unexpected since the coherence length sets the scale on which the pinning potential varies, and in this material it is much smaller than the separation at which we can create the vortices in a pair.

Specifically, most or all pairs seem to pass through a sequence of pinning sites as they approach each other before they eventually annihilate. This process of passing through intermediate pinning sites may be:

1. very quick compared to the pair lifetime so that the pair seems to be stationary in its initial configuration right up until annihilation (what we will call simple annihilations),

2. it may be a process that consists of several quick jumps with significant stationary configurations in between (we will call these hopping annihilations),

3. it may be a process that occurs continuously through the lifetime of the pair as though the vortices approach each other at something like a constant velocity (we will call these creeping annihilations),

4. or it may consist of creep terminated in a simple annihilation, or of hops combined with periods of creep (creep/simple or creep/hop annihilations).

Table 4.1 shows the number of annihilations of each type from five different sites in the sample. Clearly, different sites tend toward different characteristic annihilations, suggesting underlying differences in the local pinning potentials.

Simple annihilations might occur in situations where the pinning potential between the two members of the pair can be approximated by a simple double-well potential.

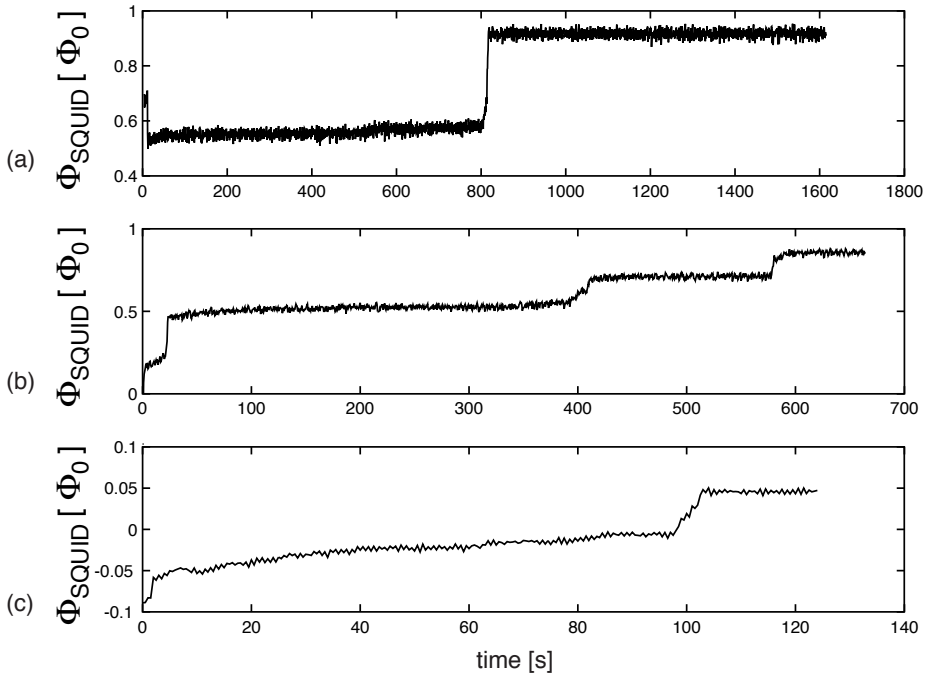

Figure 4.7: Three different characteristic vortex-antivortex annihilations. The graphs show the flux through the SQUID as a function of time from the creation of a vortex pair for pairs at three different sites. The flux is measured with the SQUID parked over the initial position of one member of the pair. As the pair moves closer together, the flux captured by the SQUID is reduced until, when the pair annihilates, the flux reaches the background level. (a) A well defined annihilation event: the flux through the SQUID jumps directly from the initial value to the background level. Data such as these are used to build histograms of pair lifetimes (see Fig. 4.8). (b) Flux through the SQUID jumps through several intermediate values before reaching the background level. We believe this sort of signal is due to the one vortex of the pair (or possibly both) hopping through a set of pinning sites on its way to annihilation with the other member of the pair. (c) The measured flux through the SQUID creeps slowly from the initial value to the background level. We believe this is associated with the vortex-antivortex pair creeping slowly together through a sequence of closely spaced pinning sites.

Table 4.1: Accumulated data from vortex-antivortex annihilation measurements at five different sites on a $YBa_2Cu_3O_{6.354}$ sample. Data in the 'other' category consist of annihilation timetraces in which the SQUID feedback lost lock, and timetraces in which the pair persisted longer than the measurement time (1 minute at 4.6K, 4 minutes at 4.5K, 8 minutes at 4.26K).

site	# simple	# creep/simple	# hop	# creep/hop	# other
A	156	23	3	2	24
B	0	2	0	20	4
C	30	9	4	3	3
D	9	3	24	1	1
E	0	2	7	4	4

For example, the vortices might be pinned in sites relatively much deeper than other pinning sites between them, and the thermal energy available to the vortices is larger than the depth of the intermediate sites so that their effect can be neglected once one of the vortices escapes its initial, deep pinning site and begins moving toward its partner. I would speculate that creep annihilations occur in regions where the pinning potential has many closely spaced pinning sites available, all of similar energies, and at temperatures where the thermal energy is comparable to the pinning energies so that the vortices keep moving. Hopping annihilations probably result when the landscape has a few relatively deep pinning sites, with the thermal energy slightly less than the average pinning energy of these deeper sites so that the vortices are likely to become trapped in the sites for some time before escaping. In this picture it is useful to consider the attraction between the two vortices in the pair. A simple calculation from de Gennes (1989), for example, gives formula 4.1. Note, however, that this expression for the force is derived under the assumptions that the vortex behaves as a rigid cylinder and that the superconductor has a homogeneous background superfluid density. Chapter 6 of this thesis and Guikema (2004, chapters 5 & 6) give strong evidence that vortices in these samples behave as stacks of pancake vortices rather than as rigid ones, and that the homogeneity is in question. Nonetheless, the formula for rigid vortices is approximately correct as long as the pancakes remain at least closely aligned (within about λ_{ab}). The force of attraction between the two vortices

is thus approximately

$$f_{12} = \frac{\Phi_0}{c} j_1(r_2) = -\frac{\Phi_0^2}{8\pi^2\lambda^2} \frac{\partial}{\partial r_{12}} K_0(r_{12}/\lambda) \tag{4.1}$$

which varies as $1/r_{12}$ for $r_{12} \ll \lambda$ and like $\exp(-r_{12}/\lambda)$ for $r_{12} \gg \lambda$. In our situation we are creating the pairs with $r_{12}(t = 0)$ of about 8μm. So we probably start almost in the exponential regime, but we cross over into the $1/r$ regime before annihilation.

It is interesting to note that the paths through intermediate pinning sites seemed reproducible at a given location and temperature in the sense that for hop and creep/hop annihilations, the sequence of hops would almost always be the same size (in terms of flux change). This is at least consistent with the pairs going through the same sequence of intermediate pinning sites. Anecdotally, the time constants associated with each of the hops in such a sequence was consistent from one timetrace to the next at the given location and temperature, though there are insufficient data to quantify this.

At those sites without intermediate pinning, we could measure pair lifetime histograms as a function of temperature and found that the characteristic $\tau(T)$ does sharply decrease as T increases. In the absence of any detailed information on the local pinning potential at the measurement site, we analyzed the histograms in terms of the overly simplistic picture of thermal activation out of a double-well potential. In this case, the pair lifetimes should follow an exponential distribution with $\tau(T)$ as the time constant. Fitting this model to the histograms in Fig. 4.8 gives $\tau(4.6\text{K}) =$ 31s+8/-15s, $\tau(4.5\text{K}) =$ 56s+13/-14s, and $\tau(4.2\text{K}) =$ 83s+37/-29s, where the errors quoted are the 90% confidence intervals calculated with a bootstrap method. However, as noted on Figure 4.8(b) and (c), we sometimes measured pairs which persisted for a very long time and were omitted from the fits. These pairs did not fit into the thermal activation picture. To the extent that the exponential distribution of pair lifetimes is valid, the procedure of generating pairs at T_{ref} and then ramping to T_{meas} does not introduce a systematic error in the the determination of $\tau(T)$ as long as only those trials where a vortex pair was still present once T_{meas} was reached are counted.

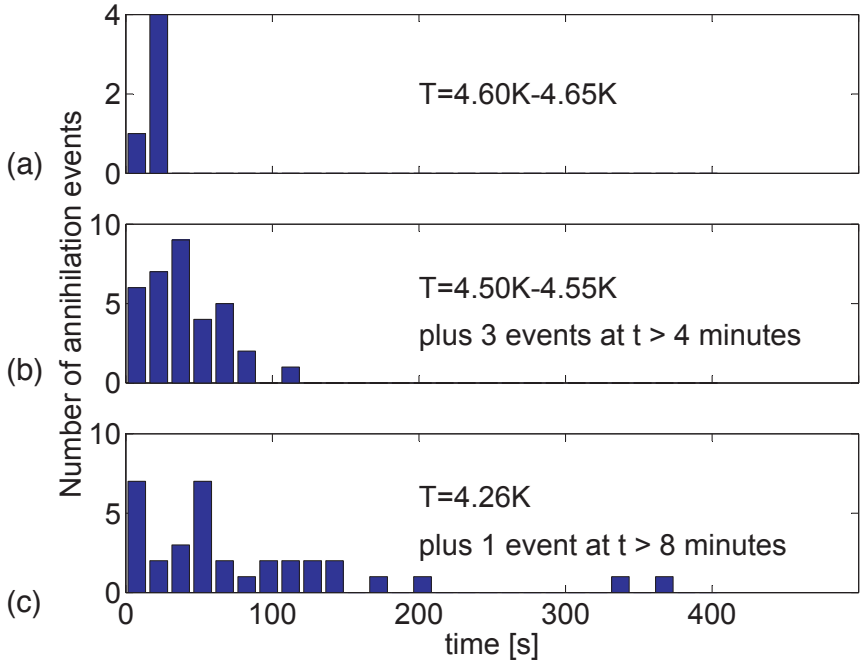

Figure 4.8: Histograms of vortex pair lifetimes at different temperatures. (a) At $T = 4.60 - 4.65K$. (b) At $T = 4.50 - 4.55K$. (c) At $T = 4.20 - 4.26K$. Each histogram consists of many vortex lifetime measurements like that in Fig. 4.6(a). The characteristic lifetime for nominally identical vortex-antivortex pairs decreases sharply with increasing temperature. Some vortex pairs persisted beyond the measurement time (noted in each panel), indicating that a simple model of thermal activation of the vortices over a potential barrier (which leads to an exponential distribution of pair lifetimes at each temperature) is inadequate. All measurements in this dataset were made on nominally identical vortex pairs created at $T = 4.16K$ with a current $I_{\rm fc} = 20$mA. Measurements were performed by first creating the vortex pair at $T = 4.16K$ and then quickly ramping to the measurement temperature.

We note the possibility that a single crystal may be thick enough to allow a U-shaped tube of flux inside the sample instead of a pair of vortices which penetrate all the way through (Fig. 4.4). Because a scanning SQUID only images the surface flux, we would be unable to distinguish such configurations. Additional theoretical work is required to address this possibility and to model the motion through intermediate pinning sites.

4.6 Conclusions

We have developed a technique for creating vortex-antivortex pairs in superconducting samples by the application of a local magnetic field from a SQUID susceptometer. This allows us to study the vortex pairs, the fields required to create them, and the ways in which the pairs annihilate.

The fact that pairs could be created at field scales just slightly higher than was required to move vortices in these samples (chapter 3) suggests that the pinning sites on which vortices sit are very deep, because it takes a field almost sufficient to suppress superconductivity in order to move them.

The variety of characteristic types of vortex-antivortex pair annihilations we observed suggests that pinning sites in these materials have a wide range of energies. The number of hops in a hopping annihilation suggests that the length scale for deep pinning sites is on the order of microns. The existence of simple annihilations similarly supports that idea.

Even in the simplest cases, the pair lifetimes did not fit a simple picture of thermal activation, suggesting that pinning is complicated.

Chapter 5

The Senthil Experiment

5.1 Introduction

Since their discovery, the cuprates have proven a fertile ground for theories intended to explain their high superconducting critical temperatures, and indeed to explain why they superconduct at all. Spin-charge separation (SCS), first proposed for the cuprates by Anderson (1987), was one prominent growth out of the jungle of competing explanations, and has branched into several popular theories (including stripes and visons). Recently, one of these theories, proposed by Todadri Senthil and Matthew Fisher, garnered significant attention by using an object called a vison to neatly solve the problem of $h/2e$ flux quantization (which had been a challenge for SCS theories), to explain the pseudogap, and offer a sharp experimental test!

At sufficiently low doping, many SCS theories (including the Senthil-Fisher theory) predict h/e flux quanta instead of the conventional $h/2e$. At the time we began the experiment described in this chapter, our lab had recently measured flux quantization in underdoped $YBa_2Cu_3O_{6+x}$ (Wynn et al. 2001). That experiment addressed the fact that no one had previously looked at the value of the flux quantum in underdoped cuprates. We measured it to be the conventional $h/2e$. This measurement of $h/2e$ vortices at low doping can be interpreted as an upper limit of 60K[1] on the energy of the vison proposed by Senthil and Fisher, but this limit was subject to a caveat

[1]Throughout this chapter we talk freely of energies as temperatures. The factor of Boltzmann's constant, k_B, is to be understood.

that the $h/2e$ vortices observed might have been metastable: there remained the possibility that the dynamic processes involved in vortex formation could produce $h/2e$ vortices on cooling, even if h/e were energetically preferred. One could imagine this happening, for example, if there were several pinning sites available in a region where an h/e vortex was forming. Depending on the relative energy barriers for thermally activated hopping of h/e vs. $h/2e$ vortices, an $h/2e$ component of the vortex might jump into a nearby pinning site and get stuck there upon further cooling. Even if it were energetically favourable to have a single h/e vortex, this metastable state could persist. There are many other considerations that may play a role, such as the repulsive force between two vortices of the same field polarity, etc.

The experimental test proposed by Senthil and Fisher for their theory, often called the Senthil experiment, is not subject to that caveat and provides a more direct test for the vison by relying on its topological properties, not merely arguments about its energy. We performed the Senthil experiment and found no evidence for the vison. Our experiment placed an upper bound of 160-190K on the possible energy of the vison which, while higher than the 60K limit based on $h/2e$ flux quantization, is not subject to the metastability caveat and is still far below the predicted energy (the pseudogap energy $T^* \sim$ 500-700K in these samples). This makes theories relying on the vison to explain superconductivity and the pseudogap unlikely candidates as theories of the cuprates.

Around the same time as we were performing the Senthil experiment, Kirtley et al. (2003) approached the problem by making dynamic measurements of the telegraph noise associated with vortices hopping in and out of superconducting rings. These experiments were performed on Pearl vortices[2] in thin film BSCCO rings and, depending on the estimates of τ_0, showed a vison energy of 60-300K, where the pseudogap temperature at that doping is $\sim$ 300K. Our work has centred on $YBa_2Cu_3O_{6.350}$ samples which are single crystals and grown at much lower doping than is possible

[2]Pearl vortices occur in thin films and have an increased effective penetration depth $\Lambda = \lambda_{ab}^2/d$, where d is the film thickness, due to the fact that such a thin film cannot support sufficient currents to shield the vortex field exponentially (Pearl 1966). The field for such vortices falls off as $1/r$ for short distances and $1/r^2$ at longer distances, where Λ defines the crossover between the two regimes. For samples which are laterally small compared to or of order Λ in addition to being thin, one has fluxoid quantization rather than full flux quantization (see Chapter 1).

in BSCCO, allowing a greater difference between T_c and the pseudogap temperature scale.

5.2 A picture of spin-charge separation theory

Spin-charge separation (SCS) refers to a system consisting of many electrons which forms a state where the electron is no longer the basic excitation. Instead, the basic excitation of the system is a collective one consisting of many electrons. A more familiar example of this might be the Landau quasiparticle from the theory of metals, in which the basic excitation consists of an electron surrounded by a collection of other electrons it is pushing or pulling along with it. In the case of SCS there are two collective excitations of electrons: one called the "spinon", with spin $\frac{1}{2}$ and charge 0, and one called the "chargon", with spin 0 and charge e, which become the basis states appropriate for describing excitations of the system. Thus, in the resulting states, the spin and charge may behave more or less independently. The electron is said to fractionalize into a spinon and a chargon. Theoretically, $c^\dagger = f^\dagger b^\dagger$, where $f^\dagger$ is the spinon creation operator (a fermion) and $b^\dagger$ the chargon creation operator (a boson). Note that the chargon is a boson, so that a collection of chargons may bose-condense into a superconducting state without regard to what the spinons are doing. No Cooper pairing is necessary.

The lack of need for Cooper pairing to achieve superconductivity is one of the attractive features of SCS theories for the cuprates, because it may explain the extraordinarily high transition temperatures. Superconductivity without pairing might also be expected to have other novel features. Flux quantization in conventional superconductivity is $h/2e$ and comes about from the condition that the circulation of a Cooper pair (charge $2e$) around one flux quantum should result in a winding of the phase of the wavefunction by 2π. In SCS theories where the charge carrier is the chargon (charge e) rather than the Cooper pair, the equivalent condition would give a flux quantum of h/e.

Shortly after Anderson's suggestion that cuprate superconductivity may be driven by spin-charge separation, Gough et al. (1987) measured the flux quantum to be

the conventional $h/2e$ in optimally doped $YBa_2Cu_3O_{6+x}$, initially dampening the prospects for SCS. There proved to be ways to reconcile SCS with $h/2e$ flux quantization (Kivelson et al. 1988; Sachdev 1992; Nagaosa 1994; Senthil and Fisher 2001), however h/e remains a feature of the theories at very low doping. This is because the low superfluid density implies a relatively low energy cost (in terms of the Ginzburg-Landau superfluid energy) to combine two $h/2e$ vortices. It eventually becomes smaller than the energy cost of whatever mechanism provided for $h/2e$ flux quantization in the given SCS model. Thus, many SCS theories for the cuprates, including Senthil & Fisher's, predicted an area at low doping where h/e vortices would be energetically favourable compared to $h/2e$. In the case of Senthil-Fisher theory, the mechanism for $h/2e$ flux quantization is the vison (to be explained in the next section). So the existence of h/e flux quanta is tied to the energy of the vison.

The only existing measurements of flux quantization in the cuprates (Gough et al. 1987) had been carried out in the optimally doped regime. This led us to extend measurements on flux quantization into underdoped regime (Wynn et al. 2001) where we measured it to be $h/2e$ – the same as in the optimally doped regime. In terms of spin-charge separation, the measurement of $h/2e$ vortices at low doping gave a limit on the energy of the vison (60K), but this limit was subject to a caveat that the $h/2e$ vortices observed might have been metastable.

Senthil and Fisher's proposal for the detection of visons is not subject to this caveat.

5.3 The Senthil-Fisher formulation of SCS

The spin-charge separation theory proposed by Senthil and Fisher has three exciting features:

1. It fixes the h/e vs. $h/2e$ flux quantization issue (at most dopings) because the the $h/2e$ fluxoid coexists with a vison which contributes an additional phase winding of π

2. It gave some hope of explaining the strange behaviour of the pseudogap as the

physics of spin-charge separation, e.g. spinons, chargons and visons.

3. They proposed an experimental test for their theory based on detecting the signature of the vison!

Clearly the vison plays a central role in this theory. A more detailed look at the vison and its role in Senthil-Fisher theory can be found in Appendix A, but for the purposes of this chapter, it can be defined by three properties:

1. The vison is a topological defect which introduces a phase π to the wavefunction of a chargon or spinon that winds around it. It has no effect on an electron.

2. The vison has an energy on the scale of the pseudogap temperature T^*.

3. The vison carries $\mathbb{Z}_2$ symmetry because it results from the flux of a $\mathbb{Z}_2$ gauge field. This means that two visons are the same as no vison, or any even number of visons. Similarly, one vison is the same as three visons, or any odd number.

The vison can reconcile the notion of charge e chargons in SCS with $h/2e$ fluxoids in the following way: a chargon going around a vison picks up a phase winding of π, so that in order for the wavefunction to remain single-valued there must be another source of $\pm\pi$ phase winding. For charge e chargons, a magnetic flux of $h/2e$ fulfills exactly this role. So the Senthil-Fisher picture of spin-charge separation has composite vortices which consist of $h/2e$ flux plus a vison.

Because of the $\mathbb{Z}_2$ nature of visons, two visons are the same as no vison. So a putting two vortices with flux $h/2e$ and a vison each together creates a double vortex with flux h/e and no vison. Another way to think of this is that a double vortex with flux $\pm h/e$ would already provide a phase shift of $\pm 2\pi$ to the wavefunction of a chargon and wouldn't require any visons anyway. Since visons cost an energy $\sim T^*$ each, any situation requiring an even number of visons will have zero, and any situation requiring an odd number will have just one.

The scaling of the vison energy with T^* means that visons become more and more expensive as doping is decreased (see Fig. 5.1). In particular, they begin to dominate the superfluid energy of the vortex. At sufficiently low doping, it is energetically

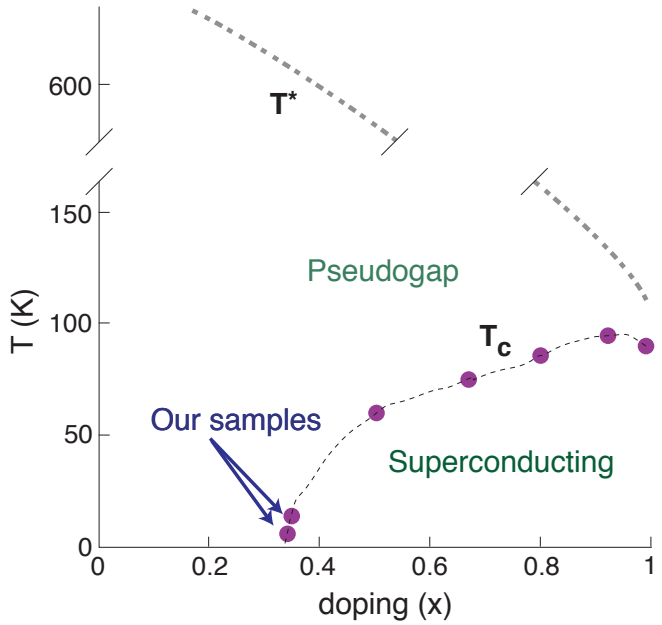

Figure 5.1: Phase diagram for $YBa_2Cu_3O_{6+x}$ showing the very underdoped crystals (with $T_c = 6$K, 12K) used in the experiment. The vison energy is predicted to be of order T^* which is extrapolated to be 500K-700K for the doping of the samples we used.

favourable to combine two $h/2e$ vortices into an h/e vortex in order to save the cost of the visons. This is the source of the predicted stable h/e vortex regime at very low doping in the Senthil-Fisher theory.

The Senthil-Fisher picture of the phenomenology of the underdoped side of the cuprate phase diagram goes like this:

- At high temperatures ($>> T^*$) the electrons are the basic excitations of the system. Theoretically, visons proliferate (they are essentially free) so that any spinon separated from a chargon incurs a cost of a wildly fluctuating phase as visons whiz between them, thus the electron is preferred to separated spinons and chargons.

- As T decreases below T^*, there are fewer free visons roaming around. The spinon and chargon collective excitations can then become unbound and you have spin-charge separation. The pseudogap phenomenon seen in various experiments results from the energy cost of the vison necessary to re-bind the spinon and chargon excitations into an electron excitation that is actually measured.

- As T decreases below T_c the chargons bose condense and form a superconducting state. Vortices with $h/2e$ flux must also contain a vison.

The vison can be thought of as the glue that holds the spinon and chargon together. The fact that visons start to become energetically expensive below T^* means that this is the temperature where spin-charge separation sets in.

The fluxoid and vison have different energies (T_c and T^*, respectively) which lead to different characteristic timescales for them to escape over a superconducting barrier via thermal activation.

5.4 The Senthil experiment

The experimental test for the existence of the vison depends crucially on its phase-winding characteristics, and the difference in the escape rates over a superconducting barrier for a vison compared to an $h/2e$ fluxoid. The experiment, as depicted in Figure 5.2, works like this:

1. Cool a superconducting ring below T_c in an ambient field so that there is one fluxoid in the ring (and in the Senthil-Fisher theory, there is also a vison).

2. Remove the applied field so that the ring is now in zero field.

3. Warm the ring to T_c so that the fluxoid will escape from the ring. Re-cool. This step should be performed very quickly so that the vison has very little chance to escape.

4. Check to see if there is a fluxoid formed upon re-cooling. If there is no vison, then cooling in zero field should lead to no fluxoid in the ring. If there is a vison, then an $h/2e$ fluxoid is required to satisfy the phase winding of $n2\pi$. In zero applied field, the orientation of the spontaneously generated fluxoid doesn't affect the energy, so it should be random.

So the signature of a vison would be a 'memory effect' whereby re-cooling in zero field would generate a fluxoid of random sign if there was originally a fluxoid (plus vison) in the ring. In fact, the $\mathbb{Z}_2$ nature of the vison where two visons are equivalent to no vison implies that there should be a fluxoid of random sign for any odd number of initial fluxoids (plus one vison), and no fluxoid upon re-cooling for an even number of initial fluxoids (which have no vison).

The brilliance of this experiment lies in the fact that it detects the vison based on its topological properties. With a scanning SQUID or Hall probe sufficiently sensitive to readily discriminate single $h/2e$ fluxoids, one can be sure of detecting the vison signature. It is not subject to the concern that a given $h/2e$ vortex in a sample may be a metastable state rather than the ground state.

The original proposal for the experiment actually called for varying the doping of the sample at zero temperature in order to move in and out of the superconducting regime. While this is indeed more elegant, it remains impossible. Varying the temperature, on the other hand, is something we can do. This leads to the entry of vison/vortex dynamics into the picture. Instead of performing a simple yes/no experiment for the existence of the vison, we use the notion of the escape rate for

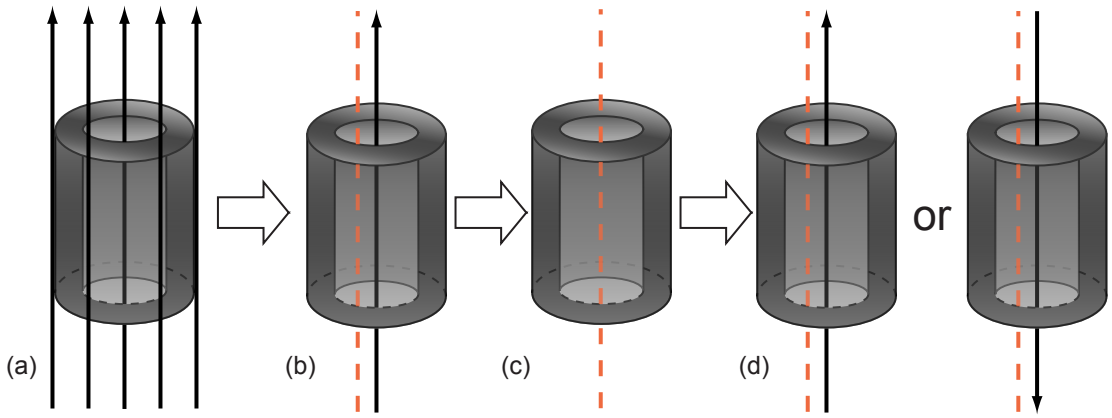

Figure 5.2: Sequence of steps in the experiment proposed by Senthil and Fisher: (a) a superconducting ring is cooled below T_c in an ambient field so that there is one $h/2e$ fluxoid (and one vison) in the ring. (b) the applied field is removed so that the ring is now in zero field. (c) the ring is quickly warmed above T_c so that the $h/2e$ magnetic flux escapes, but the vison remains trapped, and immediately re-cooled. (d) on cooling back below T_c the bare vison must nucleate an $h/2e$ fluxoid to satisfy the requirement that the phase winding be a multiple of 2π. In zero applied field, the orientation of the spontaneously generated fluxoid doesn't affect the energy, so it should be random.

the vison to set a limit on the activation energy for the vison to jump the barrier presented by the ring wall, and hence set a limit on the energy of the vison.

Since the energy of the vison in the hole is zero, then the height of the energy barrier the vison must jump to get over the sample wall is at least equal to the energy of the vison in the material. Using a thermal activation picture, the time for a vison to escape the sample is given by

$$\tau_{\text{vison}} = \tau_0 \exp\left[E_{\text{vison}}/k_B T\right] \tag{5.1}$$

where τ_0 is an unknown timescale between the vison's "escape attempts" based on microscopic details.

In order to perform the test for a vortex memory effect, it is important to be able to cycle the sample to T_c and re-cool faster than the vison escape time. The vison escape time is longest at low doping due to the increase of the pseudogap energy ($E_{\text{vison}} \sim T^*$ in the Senthil-Fisher theory). Not only do we want the vison not to escape, but we have to wait for the fluxoid to escape before re-cooling. Therefore we want samples in which the energy of the vison and the magnetic energy of the fluxoid lead to very different timescales for the escape rates τ_{vison} and τ_{fluxoid}. That is, T^* should be as high as possible and T_c as low as possible, as is the case for very underdoped samples. The low T_c of sample also means that thermal energy ($k_B T$) is low throughout thermal cycle. Thus, the low doping and low T_c of the samples combine to keep $E_{\text{vison}}/k_B T$ large, and hence τ_{vison} remains long, and long compared to τ_{fluxoid}.

5.5 Samples

High-quality samples of $YBa_2Cu_3O_{6.354}$ with the required characteristics have recently become available (Liang et al. 1998, 2001). The samples used in our experiments were single crystals with T_c of $\sim$ 12K, $\sim$ 7.5K and 6K. Each was hand cleaved to approximate dimensions of 50μm by 50μm in order to fit entirely within the scan range of our scanner. Each sample then had a 10μm diameter hole drilled in it with

a Focussed Ion Beam (FIB) (see Fig. 5.4, top right), and was then mounted in silver epoxy.

5.6 Measurements

With its high flux sensitivity, ability to vary temperature quickly in a range near the sample T_c and capacity to image an entire 50μm sample, our scanning SQUID microscope was well suited for the Senthil experiment.

The SQUID used in this experiment was a Nb based susceptometer fabricated at HYPRES Inc. with an 8μm by 8μm square pickup loop. For the lowest T_c sample (T_c = 6.0K), this meant that we were able to measure T_c *in situ* by observing the diamagnetic susceptibility turn on as a function of T. The other samples had T_c's which were either above or too close to the SQUID's T_c for us to measure them in this fashion, and their T_c's were measured on a commercial SQUID magnetometer.

Imaging with an applied field at low T allowed us to use the sample's diamagnetic shielding to locate it and centre it within our scan area using the coarse motion stage. With the sample centred, we cycled above T_c and cooled in various dc applied fields then imaged the sample to determine how many flux quanta were captured in the hole. We later performed integration of the flux in the images to ensure our flux quanta were multiples of $h/2e$ (rather than h/e). Once we had determined zero field and the applied fields required to trap a given number of flux quanta, we proceeded with the experiment described in section 5.4.

Scans to check the flux in the hole took approximately 60s. Note, though, that it is the time spent cycling near/above T_c which is relevant to the possibility of vison escape, not the low T scanning measurement time.

5.7 Results & Discussion

In all of our measurements we saw no evidence of a vortex memory effect. Figure 5.3 shows a complete set of images for one sample with initial configurations ranging from +6 to -3 fluxoids. The cross sections shown in the right-hand column

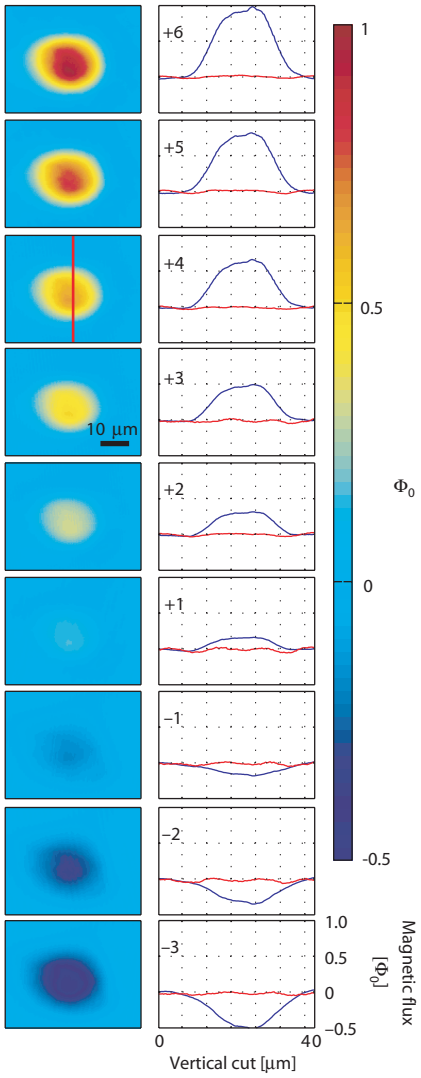

Figure 5.3: Results of the first Senthil experiment on a sample, with initial states running from +6 to -3 vortices in the sample hole. Images in the left column show scans of the initial state, after field-cooling below T_c to generate the desired number of fluxoids and then zeroing the ambient field. The vertical red line in the image for the initial state of +4 vortices indicates the cut used for the cross sections shown in the right hand column. Blue cross sections are from the initial state images, red cross sections are from the final state images (not shown). The final state cross sections show that there was no vortex memory effect for any of these initial states.

demonstrate that no vortex remains after cycling above T_c.

We set a limit on the energy of the vison by using the temperature cycle time in our measurement as an upper bound on the vison escape time: given that we never saw the vison signature, then if it exists at all, it must have escaped from the hole in some time less than τ_{cycle}. Substituting equation 5.1 into $\tau_{\text{vison}} < \tau_{\text{cycle}}$ and solving for E_{vison}, we obtain

$$E_{\text{vison}} < k_B T \ln\left(\frac{\tau_{\text{cycle}}}{\tau_0}\right) \tag{5.2}$$

where T may be taken as the maximum temperature during the cycle (typically T_c, or just below).

The lowest T_c sample ($T_c = 6.0$K) and shortest cycle time (1s) provide the most stringent limit on E_{vison}. Before quoting that limit, however, there are some additional effects observed in this sample that deserve explanation. Flux was frequently observed to be trapped in the annulus or to 'leak' from vortices trapped in the central hole into the annulus. These could indicate that the ring is effectively granular – even though it is a single crystal. That might come about if the doping were sufficiently inhomogeneous (say, due to oxygen disorder) that some parts of the sample were effectively non-superconducting. Even if that were the case, the Senthil-Fisher theory predicts that these intergrain regions would be in a "fractionalized insulator" state where the vison still costs an energy $\sim T^*$, so this would not provide an easy escape route for the vison, and the vortex memory test would still work as advertised.

In addition to possible indications of granularity, other vortices in the sample annulus could interfere with the measurement. For example, if one performs the Senthil experiment while there is a nearby vortex in the sample annulus, then as you cycle above T_c the magnetic part of that vortex escapes and the vison that was paired to it may jump into the sample hole (which is a lower energy state for the vison) and annihilate with a vison already in the hole, thus eliminating the expected vortex memory effect. Thus the importance of having the entire crystal sample fit within the microscope field of view in order to be sure there are no extraneous vortices.

With this in mind, we note that the data set pictured in figure 5.4 is constructed of runs in which there was a clear number of fluxoids in the central hole and no other

flux in the annulus.

In order to turn this data into a limit on the vison energy, we need an estimate for τ_0. A very conservative estimate might be $\tau_0 = 2 \times 10^{-15}$s, the time for an electron to cross a CuO_2 unit cell. With the data set shown in figure 5.4, in which cycling the temperature to 5.6K for 1s was sufficient to allow the fluxoid to escape, this would give $E_{\text{vison}} < 190$K. As a more realistic estimate, one might consider the lower bound of $\tau_0 = 10^{-12}$s given for vortex movement in the context of vortex creep in conventional superconductors and based on the characteristic frequencies of lattice vibrations (Beasley et al. 1969). This gives $E_{\text{vison}} < 160$K. In either case this is much lower than the pseudogap energy scale, which is believed to be in the range of 500-700K for samples with this doping (Tallon and Loram 2001).[3]

5.8 Conclusions

In summary, it seems unlikely that cuprate superconductivity is explained by SCS with visons, because the visons, if they exist, do so only at an energy scale much lower than the pseudogap temperature – presenting a serious challenge for theories which depend on them. There is still some debate, however, about how broad a range of SCS theories are covered in this class and whether there are some SCS theories which might still be reasonable candidates.

Some theorists, for example, have found SCS formulations in which the vison is gapped at an energy scale much lower than the pseudogap (Paramekanti et al. 2002, 2003) , while others suggest that the electron-doped cuprates may display the expected SCS/vison behaviour where the hole-doped cuprates do not (Ribeiro and Wen 2003). These possibilities show that SCS is still a matter of great interest for the cuprates, though the appeal is somewhat reduced because the SCS/vison picture no longer seems viable as a general explanation for superconductivity and pseudogap physics in the cuprates.

[3]Actual measurement of the pseudogap crossover temperature in these samples is not possible because the samples themselves break down before those temperatures. The pseudogap energy at these dopings is extrapolated from measurements at higher dopings.

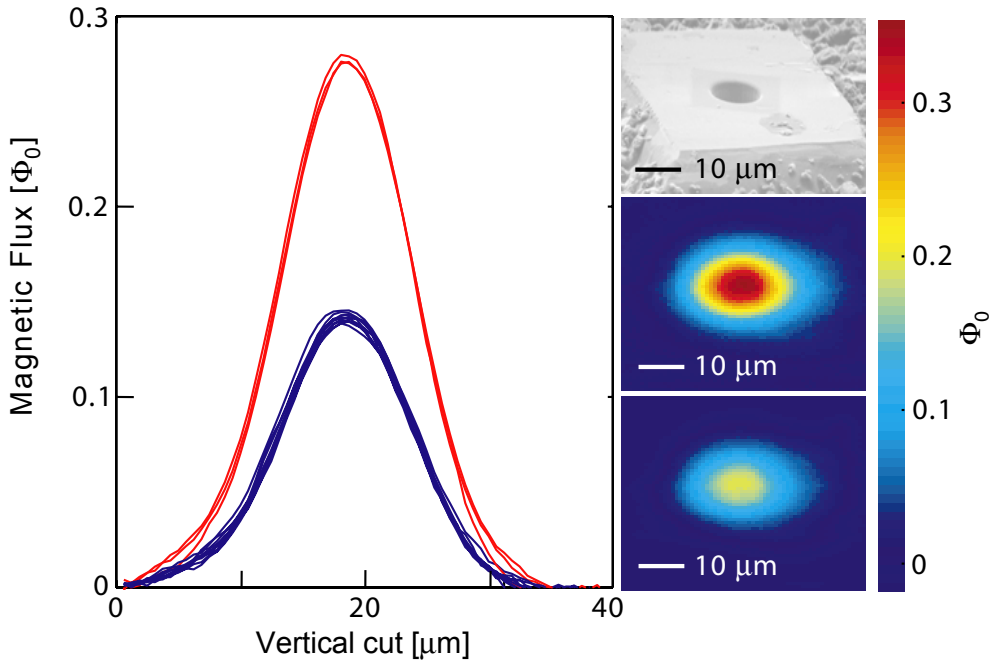

Figure 5.4: Results of the final Senthil experiment. Many runs with initial states of one fluxoid (blue cross sections, lower scan image) and two fluxoids (red cross sections, upper scan image) all showed no vortex memory effect. The greyscale image on the top right is a scanning electron micrograph of the $YBa_2Cu_3O_{6.354}$ sample showing the 50μm by 50μm crystal with a central hole drilled by a focussed ion beam. Asymmetry of the fluxoids in the scanning SQUID images is likely due to irregularities in the cleaved crystal. The lack of a vortex memory effect after cycling to 5.6K for less than 1s leads to a limit on the possible energy of a vison, $E_{\text{vison}} < 160$K.

Chapter 6

Fluxoid dynamics in $YBa_2Cu_3O_{6.350}$ rings

6.1 Introduction

The total energy of a vortex (including the core energy) is a fundamental phenomenological parameter which, although it can be calculated for BCS superconductors, is not precisely known for the cuprates. Liang et al. (1994) inferred the vortex energy from careful measurements of H_{c1} on an ellipsoidal sample of YBCO, but there has been no measurement made on single vortices. In principle one should be able to extract the core energy from the total vortex energy, at least in a Ginzburg-Landau picture. The nature of the vortex core in cuprate superconductors is an open question. Knowledge of the vortex core energy would be useful for distinguishing between competing theories and could provide insight to the normal state of the cuprates.

In this chapter I discuss an experiment intended to measure the total energy of single vortices by studying the dynamics of a vortex hopping in and out of a superconducting ring as a function of temperature. This is similar to the technique of Kirtley et al. (2003) (see also Goldman (1970)). When a superconducting ring is placed in an ambient field equivalent to $\Phi_0/2$ flux through the ring, the system has two degenerate minima of the free energy: zero or one Φ_0 through the ring. The latter state corresponds to a vortex trapped in the centre of the ring, the former to no vortex. The system jumps between these two degenerate states via thermal activation over the energy barrier between them, which is to say that the vortex hops

in and out of the ring at a rate depending on the temperature. A SQUID with its pickup loop positioned beneath the ring can detect the change in flux associated with the vortex entering or leaving the ring. The measured signal is telegraph noise with a characteristic switching rate depending on the temperature and the energy for the vortex to hop through the ring wall.

The idea behind a dynamical measurement is that one remains sensitive to what is happening at all times (within the time resolution of the measurement) and there is a possibility of seeing *how* things happen, in addition to whether they occur or not. In the context of the Senthil experiment (see Chapter 5) improved time resolution for measuring vortices or visons escaping from a $YBa_2Cu_3O_{6+x}$ ring is directly related to the limit that one can set on the vison energy. This is because the measured quantity is actually an escape time $\tau = \tau_0 \exp(E_{\rm v}/k_B T)$, where $E_{\rm v}$ is the total vortex energy, from which an energy limit is deduced under conservative assumptions about the attempt time prefactor, τ_0. We hoped, then, to pursue a measurement of the energy of a single vortex, and possibly to place a tighter limit on the possible vison energy by performing dynamic measurements.

6.2 Theory

The energy of a superconducting ring in an applied field is lowest at zero field and increases as a field is applied due to the creation of shielding currents in the Meissner state. After sufficient field has been applied, it becomes energetically favourable to admit a vortex into the ring in order to reduce the shielding currents. Further increases in applied field result in more vortices entering the ring each time the field increases by $\Phi_0/A_{\rm eff}$ where $A_{\rm eff}$ is the effective area of the ring. The energy of the system as a function of the applied field can be calculated from the Ginzburg-Landau free energy functional:

$$\mathcal{F} = \frac{1}{8\pi}\int d^3r\ \vec{B}^2 + \frac{2\pi\lambda^2}{c^2}\int d^3r\ \vec{j}\cdot\vec{j} - \frac{1}{4\pi}\int d^3r\ \vec{H}_a\cdot\vec{B}. \tag{6.1}$$

Working in the London limit, considering a cylinder tall relative to its radius ($t >> r$), and neglecting demagnetizing effects one finds that the free energy is approximately:

$$\mathcal{F} = \frac{t}{8\pi A_{\text{eff}}}(n\Phi_0 - A_{\text{eff}}H_a)^2 + \tilde{E}_0(H_a), \tag{6.2}$$

where $A_{\text{eff}} = \pi(r_{\text{inner}} + \lambda)^2$, n is the number of flux quanta in the ring, and $\tilde{E}_0(H_a)$ is a term accounting for the energy of the applied field, which is irrelevant and may be dropped. The energy vs. applied field for various numbers of flux quanta in the ring is shown in figure 6.1.

When the applied field is exactly $(n + \frac{1}{2})\Phi_0/A_{\text{eff}}$, the states of the ring with n and $n + 1$ flux quanta inside become degenerate. Near this bias field, a fluxoid may jump the barrier presented by the ring wall and enter or escape so that the ring switches from the n to $n + 1$ fluxoid state, or vice versa. The probability per unit time for a given fluxoid to do this depends on the thermal energy available, the applied flux, and microscopic parameters which can be absorbed into an "attempt frequency." Together these result in a characteristic frequency for the fluxoid transitions which should follow a thermal activation law (assuming that the microscopic attempt frequency is temperature independent). The switching of the ring's fluxoid state can be detected as a change in flux through a detector just below the ring. The resulting flux vs. time signal from the detector is characterized by so-called 'switching noise' or 'telegraph noise.'

6.3 Sample Preparation

We work with single crystals of very underdoped $YBa_2Cu_3O_{6.350}$ grown by the UBC group (Liang et al. 1998, 2001) which have T_c on the order of 3-5K. We make a ring by milling the sample with a Focussed Ion Beam (FIB) which uses 30kV Ga^+ ions to oblate material from the sample. We used an FIB beam current of 3000pA over 2-4 hours to mill a ring, and created several rings with inner radii ranging from 4-4.5μm and outer radii ranging from 7.25-15μm. These sizes were chosen in order to have a ring wall slightly larger than the penetration depth, so that we have nearly full flux

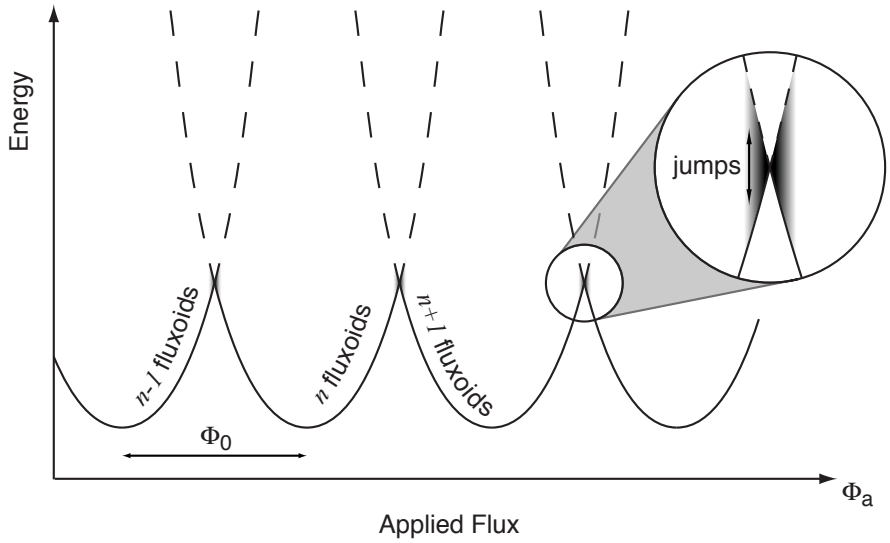

Figure 6.1: A schematic of the potential of the $YBa_2Cu_3O_{6.350}$ ring as a function of applied flux. Several branches of the potential for different numbers of fluxoids in the ring are shown. When the applied flux is $(n+\frac{1}{2})\Phi_0$ the n and $n+1$ fluxoid states become degenerate and the ring will switch between them. The grayscale shading near the intersection of the different fluxoid branches schematically indicates the characteristic switching rate between them, which is highest at the crossing point and drops off rapidly as the applied flux is tuned away from $(n+\frac{1}{2})\Phi_0$ (see blow up).

Table 6.1: Sample parameters for YBCO ring samples measured.

Sample	doping	T_c	r_{inner}	r_{outer}	thickness
Ring K **	6.350	?	4μm	9μm	20μm
Ring C **	6.350	3.6K?	10μm	15μm	20μm
Ring A **	6.350	3.6K?	4μm	9μm	20μm
Arnold	6.350	3.6K	4.5μm	7.25μm	30μm
Becky	6.350	4.7K	4.5μm	6.5μm	4.3μm
Carlos *	6.350	–	4.5μm	6.5μm	0.5-1μm

* This ring was sliced very thin with the FIB (damaged?). We saw no sign of superconductivity.

** Discovery of a leak placed the temperature measurements for rings K, C, and A in doubt.

quantization (as opposed to much of the phase winding being made up by shielding currents) while still leaving a relatively thin barrier for vortices to escape over, and in order to match closely the 8μm by 8μm pickup loop of the SQUID used for the measurements.[1] All rings were milled with the ring axis along the crystallographic *c*-axis direction so that azimuthal currents in a ring run in the *ab*-plane. The thickness of the crystals was 20 or 30μm and most rings were left that thickness. One ring, however, was turned on its side and returned to the FIB to be sliced in to sections, yielding rings of 1-5μm thickness. See table 6.1 for a summary of sample parameters. Unless otherwise noted, all data shown in the remainder of this chapter is taken from the ring "Arnold."

We hope that the importance of ion damage to the crystal will be small for our measurements because with good focus one can achieve FIB beam widths of a few tens of nanometres or less, suggesting that the damaged sections of the crystal will be isolated to only a very small layer near the ring walls. This layer should have a minimal effect on the superconductivity directly – however, inhomogeneities on this scale, which is much greater than ξ but less than λ, may affect vortex entry by modifying the surface barrier. One could also imagine that local heating during the

[1] With a ring much larger than the pickup loop, only a small amount of flux is captured and much of the signal is wasted; with a ring much smaller than the pickup loop many of the flux lines return inside the loop, contributing no net flux and again leading to a reduced signal (see Fig. 2.1(c)).

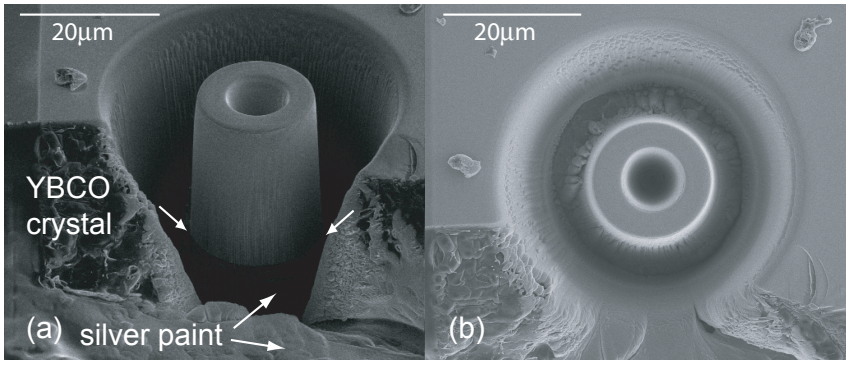

Figure 6.2: Scanning Electron Microscope images of one of the $YBa_2Cu_3O_{6.350}$ rings (Ring A) after milling with the Focussed Ion Beam. (a) 52 degree view. Notice the slight tonal change between the $YBa_2Cu_3O_{6.350}$ and the silver paint at the bottom of the ring (indicated with arrows). (b) Top view.

ion milling process might affect the samples. As evidence against this, we point out that the T_c of the samples, which can be affected by annealing around 40°C, does not seem to change.

6.4 Setup & Measurement

After milling in the FIB we are left with a $YBa_2Cu_3O_{6.350}$ ring atop a thin layer of silver paint (see Fig. 6.2(a); the silver paint is used as a conducting adhesive to attach the crystal to the sample stub for the FIB). We use a probe station consisting of an optical microscope and micrometer-controlled micromanipulators to break the ring off the silver paint and transfer it to the SQUID where it is flipped over and aligned over the pickup loop (Fig. 6.3). In order to ensure that the ring would stick in place, the pickup loop was previously painted with a thin layer of vacuum grease using an eyelash affixed to a micromanipulator. In addition to the vacuum grease, there is a 0.5 micron thick layer of silicon dioxide on top of the SQUID pickup loop (part of the multi-layer HYPRES Inc. fabrication process). The sum of these two distances gives the height of the ring above the SQUID pickup loop, which we will denote h (see schematic Fig. 6.4). One of the rings (Arnold) was later imaged in place on the

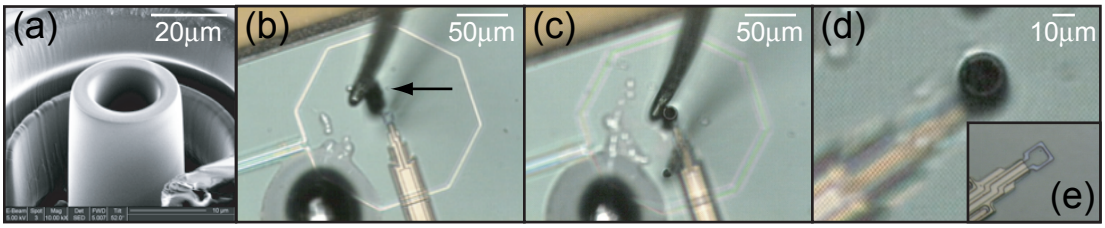

Figure 6.3: (a) Scanning Electron Microscope image of one of the $YBa_2Cu_3O_{6.350}$ ring samples (Arnold). (b)-(d) Sequence of photographs showing the placement of the ring over the pickup loop of the SQUID. The ring is indicated by an arrow in (b). A large blob of vacuum grease is visible in the lower left corner of these images. An eyelash affixed to a micromanipulator was used to paint a minute amount of the grease over the pickup loop of the SQUID. The ring (shown attached to an eyelash in (b) and (c)) was then placed on the SQUID and pushed into position over the centre of the pickup loop. (e) An image of the SQUID pickup loop without a ring, on the same scale as (d).

SQUID with a scanning electron microscope, and the height between the pickup loop and the bottom of the ring was estimated to be $0.9\mu\text{m} \pm 0.2\mu\text{m}$.

To make our measurement, we record the total flux through the SQUID as a function of time at various temperatures and with various fields applied by the susceptometer field coils.

The noise in the SQUID is on the order of $10\mu\Phi_0/\sqrt{\text{Hz}}$ which allows us to easily measure jumps as small as $1\text{m}\Phi_0$ with a bandwidth of 1kHz. In practice, we chose to keep a high signal to noise ratio in order to simplify the code necessary to count jumps in the Φ_s vs. t data we obtained. A bandwidth (after software averaging) of 100Hz was typical. This generally allowed us to measure telegraph noise over about two decades in frequency and a corresponding temperature range on the order of 0.25K.

The signal from the field coils of the susceptometer is nulled above T_c using the centre tap (described in Chapter 2) and a resistor network so that only the diamagnetic response and fluxoids in the ring contribute to the measured signal below T_c. We then perform a series of measurements:

1. Susceptibility as a function of T (a lock-in measurement) with a DC bias field applied to keep the ring away from fluxoid jumps. This gives us a susceptibility

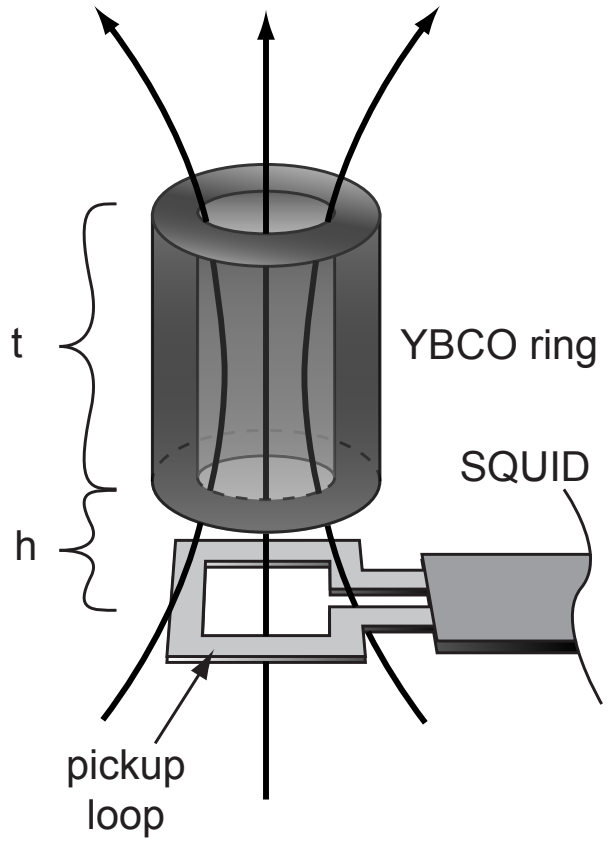

Figure 6.4: The $YBa_2Cu_3O_{6.350}$ ring of thickness t, inner radius $r_{\text{inner}} \sim 4\mu$m, and outer radius $r_{\text{outer}} \sim 10\mu$m is placed a distance h directly above the pickup loop of a SQUID. The dimensions of the ring are chosen to match the size of the SQUID pickup loop. The distance h between the SQUID and the bottom of the ring is determined by the thickness of a thin layer of grease used to hold the ring in place (not shown) plus the thickness of a silicon dioxide layer covering the pickup loop (left over from the lithography process for fabricating the SQUID; not shown). Because of the distance h between the ring and pickup loop some of the flux of a vortex in the ring does not enter the pickup loop. The penetration depth λ_{ab} also contributes to this effect, adding to the effective height. An octagonal field coil of radius 82.5μm coplanar and concentric with the pickup loop is used to apply magnetic fields. The SQUID uses a susceptometer configuration with an identical field coil and counterwound pickup loop far away on the substrate so that fields applied by the field coils are cancelled out and the SQUID is sensitive only to the flux from the ring.

curve and allows us to pinpoint T_c.

2. We next perform magnetization sweeps at each T, sweeping the field applied by the field coil and measuring the SQUID signal (Fig. 6.5). This identifies the applied fields at which the ring switches fluxoid states, and also indicates whether such switching is hysteretic at that temperature.

3. We then move to a bias field at which switching occurs and measure timetraces to see spontaneous jumps. We step the field in small increments around this bias field and take a timetrace for each applied field, H_a.

4. We then adjust the temperature and repeat the taking of timetraces for each H_a.

Table 6.2 shows the measurements performed on each of the ring samples. T range refers to the temperature range over which the measurements were performed for that sample, mag. sweeps refers to the observation of magnetization sweeps showing fluxoid jumps, intermed. states refers to the presence of intermediate states (described below) in the magnetization sweeps, telegraph noise refers to whether we observed spontaneous fluxoid switching at some field and temperature range for that sample, peaks vs. T refers to whether we tracked the peak in fluxoid switching rate as a function of H_a and T, Meissner regime refers to whether there was a range around zero field larger than Φ_0/A_{eff} at some T for which the ring exhibited no fluxoid jumps, but beyond which it did exhibit them at Φ_0/A_{eff} spacing.

6.5 Results & Discussion

In a simple picture of fluxoids hopping into and out of a superconducting ring as the applied field is changed, one would expect the magnetization sweeps to have sloped areas where the diamagnetic response of the ring deflects some of the applied field into the SQUID pickup loop (with a larger slope as T is lowered), as well as regularly spaced jumps where the maximum supported shielding current in the ring

Table 6.2: Table showing which measurements were performed on each YBCO sample. See section 6.4 for an explanation of the measurements.

Sample	T range	mag. sweeps	intermed. states	telegraph noise	peaks vs. T	Meissner regime	Susceptibility
Ring K**	?	y	n	n	n	y	y
Ring C**	3-6K?	y	n?	n	n	n	y
Ring A**	2-4.5K?	y	n	n	n	n	y
Arnold	1.9-6K	y	y	y	y	n	y
Arnold†	1.9-6K	y	y	y	y	n	y
Becky	1.9-7K	y	y	n	n	n	y
Carlos*	2.0-4.5K	n*	n*	n*	n*	n*	y*

† Flipped upside down, putting the silver paint layer between the SQUID and pickup loop.

* This ring was sliced very thin with the FIB (damaged?). We saw no sign of superconductivity.

** Discovery of a leak placed the temperature measurements for rings K, C, and A in doubt.

is reached and a fluxoid jumps into (or out of) the ring. The size of these jumps also depends on T in the same way as the slope of the diamagnetic screening sections.

For the telegraph noise timetraces, one would expect that the ring should be predominantly in the n fluxoid state when the applied field is below $(n+\frac{1}{2})\Phi_0/A_{\text{eff}}$, but occasionally jump to the $n+1$ fluxoid state for some period of time. As H_a is increased towards $(n+\frac{1}{2})\Phi_0/A_{\text{eff}}$, the frequency of such jumps and the fraction of time spent in the $n+1$ state should increase until at $H_a = (n+\frac{1}{2})\Phi_0/A_{\text{eff}}$ the switching rate is maximum and the relative occupation of the two states is 50% each. Increasing the field further reduces the switching rate and continues to tip the relative occupation towards the $n+1$ state.

As we discuss below, our observations of these two types of data were much more complex than this naïve picture.

6.5.1 Magnetization Sweeps

By sweeping the applied field, with the field coils balanced, we can see the diamagnetic response of the ring and jumps in the magnetization as vortices enter or leave the ring (Fig. 6.5). Several characteristics of the magnetization sweeps are notable:

The spacing between the dominant jumps is about 4mA (varying slightly with temperature). This corresponds to a change in applied field of $\Delta H_a \approx 0.3$G for the ring to change its fluxoid state by one. If we assume a fluxoid to have $\Phi = h/2e$ then we can calculate an effective area $A_{\text{eff}} = (h/2e)/\Delta H_a = 68\mu\text{m}^2$. For comparison, the area of the ring calculated from the inner radius is $63.6\mu\text{m}^2$ while that calculated from $r_{\text{inner}} + \lambda_{ab}$, with λ_{ab} taken as 1μm, is $95\mu\text{m}^2$. Using the geometric mean of the inner and outer radii (often used as an estimate since it accounts for some of the excess flux pushed into the ring due to shielding) gives $102.5\mu\text{m}^2$ and a similar calculation using an inner radius $r_{\text{inner}} + \lambda_{ab}$ and outer radius $r_{\text{outer}} - \lambda_{ab}$, again with λ_{ab} taken as 1μm, gives $108\mu\text{m}^2$. The fact that the measured effective area is so small is surprising. It suggests that either there are demagnetizing effects or some other shielding effects that act to decrease the effective area, or that the fluxoid may be larger than $h/2e$. If we had instead assumed a flux of h/e, we would arrive at $A_{\text{eff}} = 136\mu\text{m}^2$ which, while slightly closer to our estimated values, is too high (note that taking $\lambda_{ab} > 1\mu$m does not increase the estimated A_{eff} beyond $108\mu\text{m}^2$ because then $r_{\text{inner}} + \lambda_{ab}$ and $r_{\text{outer}} - \lambda_{ab}$ begin to overlap). This is inconclusive and requires (at least) more sophisticated modelling of the ring to get an accurate picture of what is hopping.

The slope of the linear sections due to the diamagnetic shielding is proportional to the susceptibility of the ring and becomes increasingly negative with decreasing temperature (Fig. 6.6). The susceptibility thus calculated agrees reasonably with the lock-in measurement.

The size of the dominant jumps, $\Delta\Phi_s$, visible in the magnetization sweeps depends on temperature: they are larger at low temperature and become very small near T_c (Fig. 6.6). This is presumably due to the temperature dependence of the penetration depth, λ_{ab}, which affects $\Delta\Phi_s$ in two ways. Coupling to the SQUID is not 100%, because the pickup loop sits a distance h below the bottom of the ring (see Fig. 6.4). The greater the distance between the ring and the pickup loop, the more flux can escape – so the change in flux, $\Delta\Phi_s$, detected by the SQUID due to the presence or absence of a vortex is reduced.

Flux inside the ring can spread out over a radius $\sim r + \lambda_{ab}$, so that near T_c, where

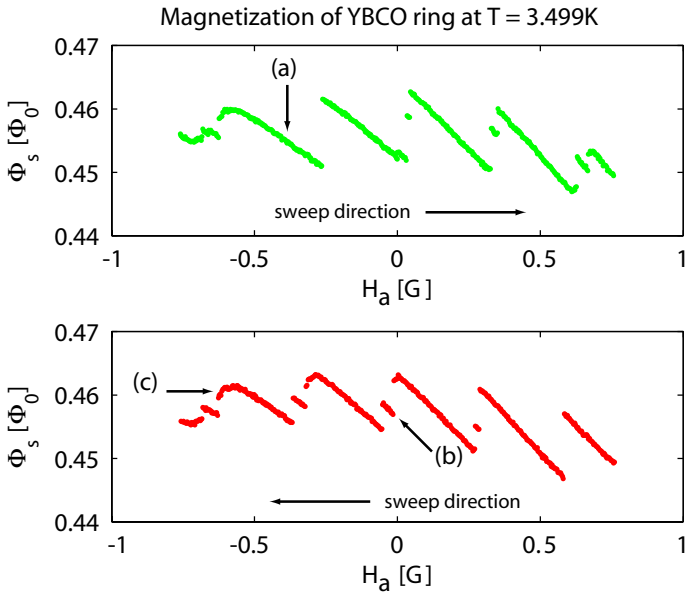

Figure 6.5: Magnetization of a $YBa_2Cu_3O_{6.350}$ ring. The vertical axis is the flux measured by a SQUID with a pickup loop 0.9μm directly below the ring. The horizontal axis is the applied field. The downward slope of the linear portions of the graphs are proportional to the diamagnetic shielding. (a) Large jumps correspond to a fluxoid entering or leaving the ring. (b) Smaller linear portions are indications of an intermediate state in between 'in' and 'out' where the fluxoid is presumably pinned in the ring wall. (c) Regions with positive slope on this graph indicate telegraph noise which is being averaged over so that the value displayed is the average flux over two states, weighted by their relative occupation. Also of note is the fact that some of the telegraph noise and intermediate state features can depend on the direction of field sweep.

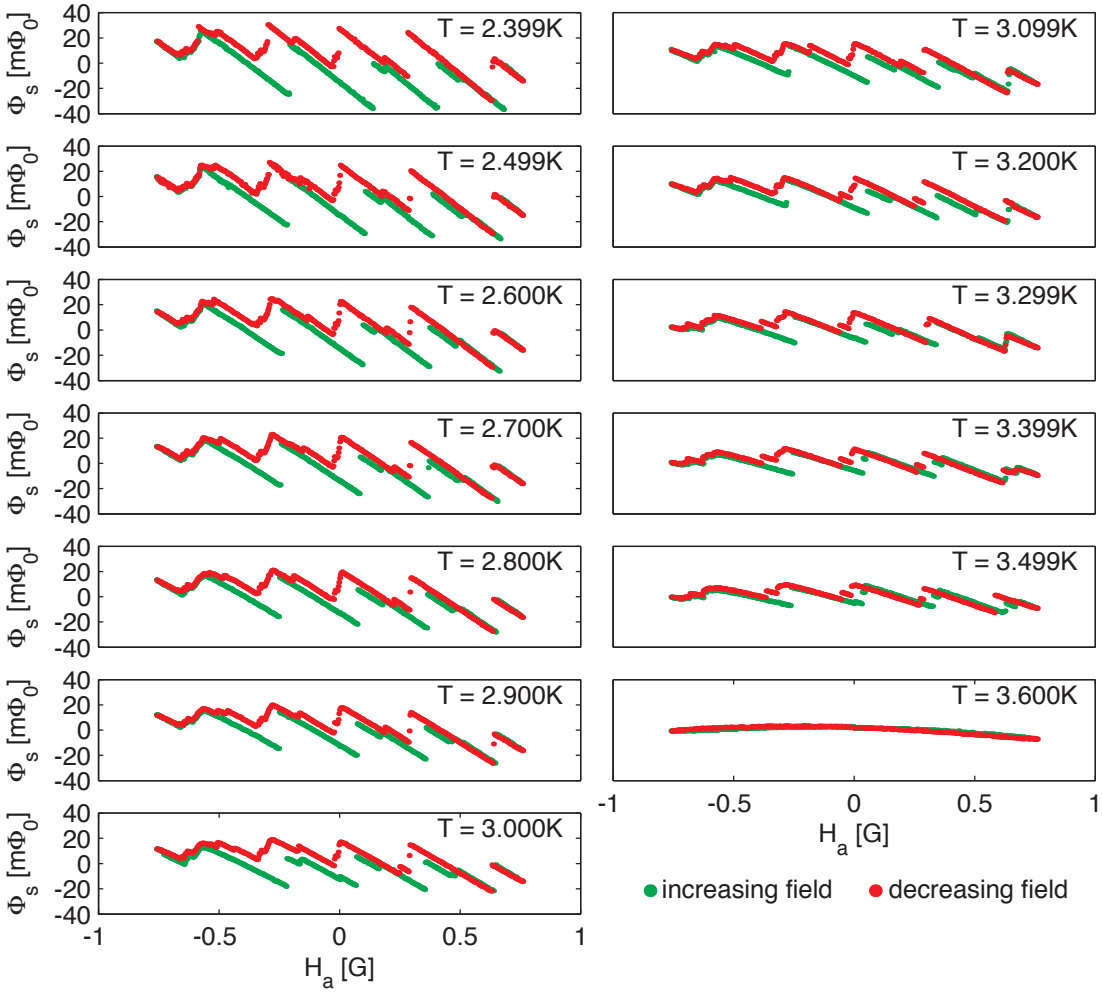

Figure 6.6: Magnetization of a $YBa_2Cu_3O_{6.350}$ ring for several temperatures. The vertical axis is the flux measured by a SQUID with a pickup loop 0.9μm directly below the ring. The horizontal axis is the applied field. Green indicates increasing field sweep, red indicates decreasing field. The slope of the linear portions of the graphs are proportional to the diamagnetic shielding. Note that the strength of the diamagnetic shielding and the change in flux measured in the SQUID between different fluxoid states of the ring decrease as temperature is increased. The slight curvature in the $T = 3.600$K plot is due to a temperature independent nonlinearity which we believe is in our SQUID feedback loop.

λ_{ab} is large, the flux can spread out more. In addition, the finite penetration depth into the bottom of the ring allows the flux even more room to spread out between the ring and the pickup loop, resulting in further decreased coupling to the SQUID. Because the amount of spreading depends not only on h, but also on λ_{ab}, this gives a temperature dependence to $\Delta\Phi_s$. Typical values of $\Delta\Phi_s$ well below T_c, where λ_{ab} is smaller, are $30\text{m}\Phi_0$. The height was measured to be $h = 0.9\mu$m using a scanning electron microscope, so such a small $\Delta\Phi_s$ indicates that λ_{ab} is very long in these samples.

Indeed, if λ_{ab} is large enough, then one may have fluxoid quantization in the ring (where flux plus the integral of the (non-vanishing) supercurrent in the ring is quantized rather than just the flux) and the actual flux in the ring due to a vortex may be less than Φ_0, again leading to smaller jumps. For these samples λ_{ab} is believed to be in excess of 1μm at low temperatures (Guikema 2004)and the annular thickness of our thinner rings is 3μm, so fluxoid quantization may occur over a significant temperature range.

In addition to the expected jumps between n and $n \pm 1$ fluxoid states of the ring, the magnetization sweeps show many intermediate states between the main branches of the curves (e.g. Fig. 6.5(b)). That is to say, the fluxoids do not tend to jump from all the way inside the ring to all the way outside. There is some, or more than one, (meta)stable intermediate state that they tend to stop in. We believe this to be a pinning site (or different pinning sites at different temperatures, see section 6.5.2). These intermediate states occur at all accessible temperatures and for almost all jumps. The fluxoids seem more likely to stop in these pinning sites on the downward sweep for negative applied fields and on the upward sweep for positive applied fields, which may indicate that pinning sites are more readily accessible for a vortex entering from the exterior of the ring than for a vortex exiting the ring, but this behaviour is not understood.

There are also 'slides' where the apparent magnetization reverses slope where you would expect a jump (e.g. Fig. 6.5(c)). After looking more closely at these, we concluded they are in fact due to the vortex jumping back and forth to another state much faster than our measurement rate so that we detect the time-averaged flux.

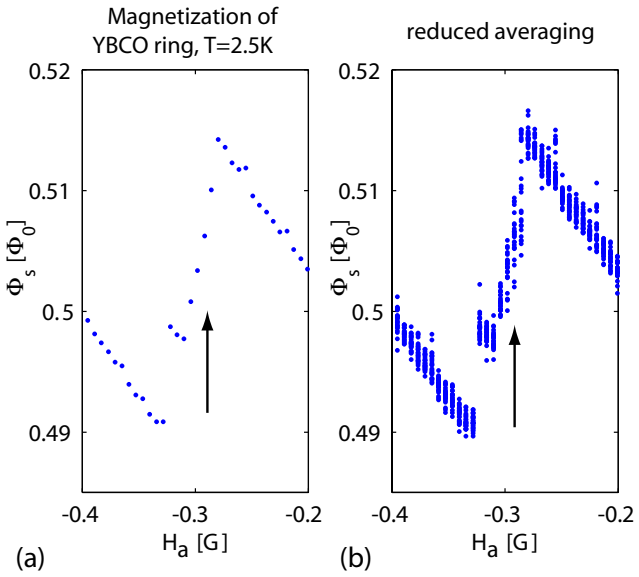

Figure 6.7: (a) Time averaged telegraph noise can appear as an apparent paramagnetic response in magnetization sweeps (positive slope on the magnetization curve, indicated by arrows). (b) Closer inspection reveals that by reducing the averaging time, increased variance is visible in this regime compared to the diamagnetic regime (negative slope) indicating the telegraph noise is partially resolved. The apparent positive slope is in fact caused by averaging of the telegraph noise, and the apparent value of Φ_s is determined by the relative occupation of the two states the ring switches between.

Figure 6.7 shows that the apparent width of the flux signal is increased on the slide area relative to the nearby diamagnetic area when we reduce averaging time and plot many points for each field. This can be explained if the variation in the flux signal in the slide area is due to partially resolved telegraph noise, while the flux noise in the diamagnetic area is the background noise of the measurement system. The relative occupation of the two states changes continuously (and roughly linearly in applied field) so that averaging gives a magnetization which appears as a continuous line with slope opposite to what you would expect for the diamagnetic response.

There is hysteresis: the field at which the vortices jump in as we ramp the field up is not the same as the field at which they jump out on the way down. As expected, hysteresis is more pronounced at lower temperatures. This is visible in the separation of the upward vs. downward sweeping data at low temperatures in the magnetization sweeps (Fig. 6.6). The hysteresis can also affect the appearance of intermediate states or telegraph noise (Fig. 6.8).

While the magnetization sweeps ought to be symmetric under time-reversal symmetry ($I \to -I, \Phi \to -\Phi$) this is not explicitly obvious. This could be due to sweep rate: sweeping too fast means that the vortex may remain in a state even when it becomes metastable, and where exactly the vortex decides to jump is statistical. Strictly speaking, the symmetry only really applies to the magnetization averaged over many sweeps, or to sweeps that are sufficiently slow that the vortex always finds the ground state before the measurement. It could also be due to symmetry breaking fields. Although a background field along the axis of the ring would give an offset that could be compensated for, a background field in the plane of the ring might be much more complicated. Indeed, it is known that Josephson vortices (i.e. vortices in the *ab*-plane) can act as pinning sites for *c*-axis oriented vortices (Grigorenko et al. 2001). Since λ_c is very large for these underdoped samples (on the order of 100μm (Hosseini et al. 2003)), we expect shielding against lateral fields to be poor. A Josephson vortex could then be expected for a lateral field on the order of $H_\perp \cong \Phi_0/(2rt) \cong 50$mG, with r the ring radius and t the thickness along the *c*-axis. Unfortunately, this setup does not provide for any way to apply a lateral field or to measure the residual lateral field, so we cannot rule this out.

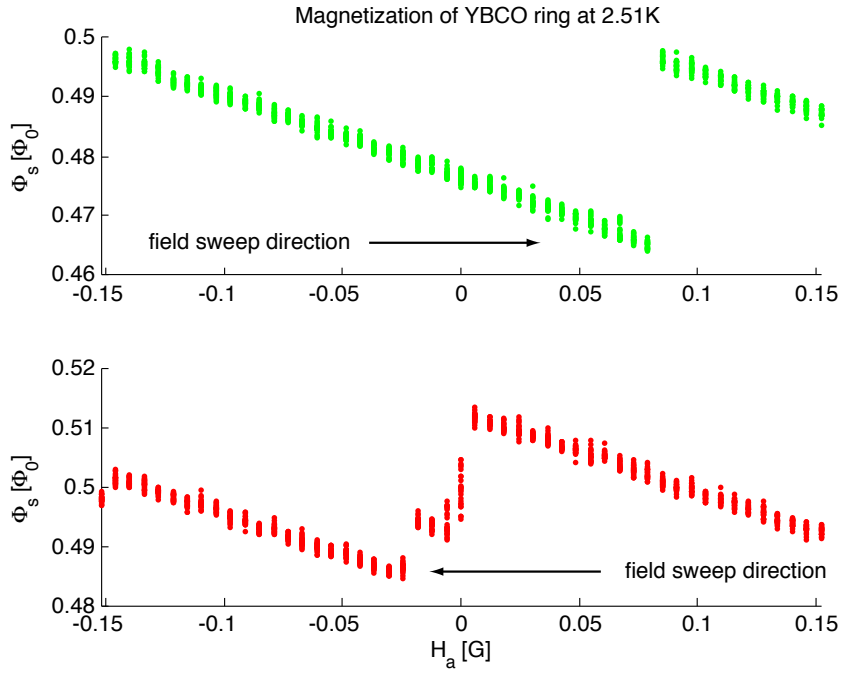

Figure 6.8: Hysteretic behaviour in the $YBa_2Cu_3O_{6.350}$ rings can be seen in the different fields at which fluxoid jumps occur (around $I_{\rm fc} = 1$mA on the upward sweep of field vs. 0mA on the downward sweep in this example). Telegraph noise and intermediate states can also depend on field history. In this case there is telegraph noise and an intermediate state at the fluxoid transition for decreasing field, but not for increasing field. Generally, hysteresis is more pronounced at lower temperatures. This example is taken at $T = 2.51$K on a ring with $T_c = 3.6$K.

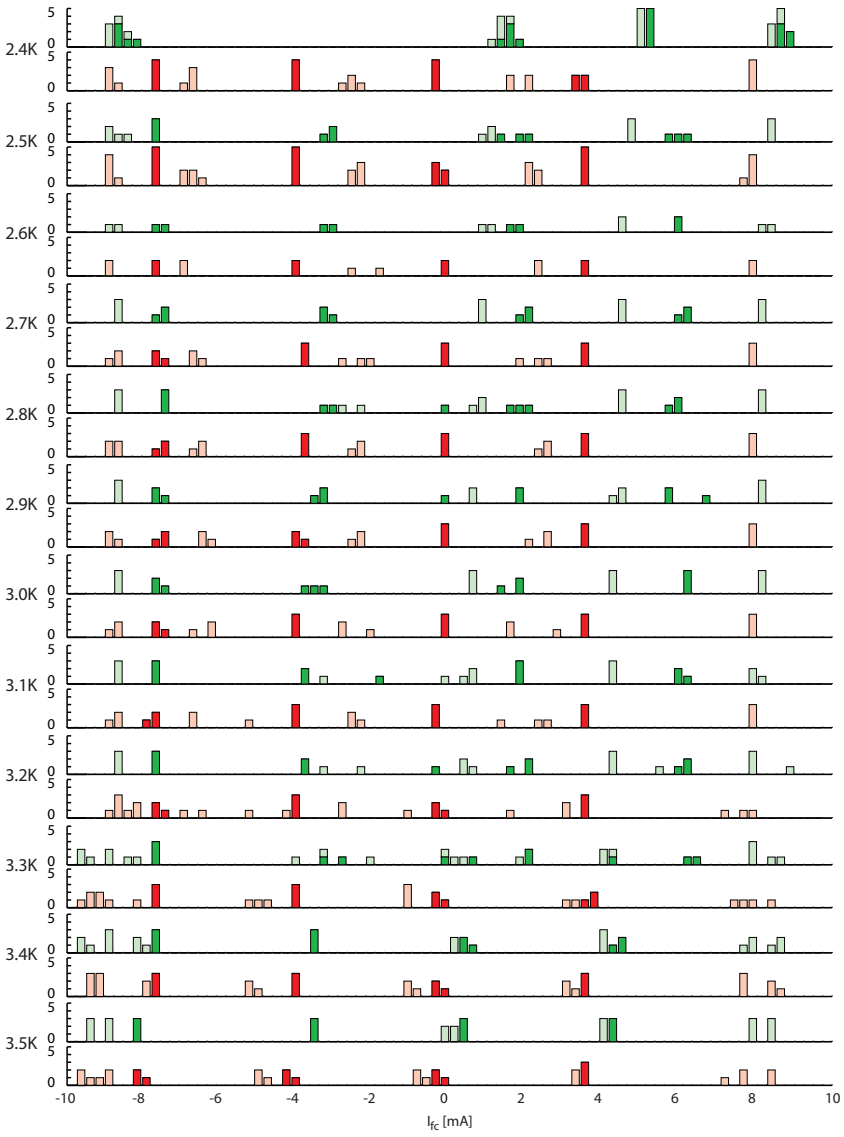

Figure 6.9: Histograms showing the number of fluxoid jumps (including both intermediate states and main branches of the magnetization curves) that occurred at each field at each temperature. Green indicates jumps on increasing applied field, red on decreasing field. Solid colours indicate dominant jumps (ending on a main branch of the magnetization curves), while pale colours indicate minor jumps (ending on an intermediate state). Data are compiled from three to five sweeps at each temperature. Hysteresis, especially for dominant jumps near zero applied field, is clearly visible at 3.3K and below.

6.5.2 Telegraph Noise

At various applied fields we observe random jumps in the flux measured in the SQUID (Fig. 6.10). Jump height or jump size refers to the change in flux associated with the jump, as measured by the SQUID ($\Delta\Phi_s$).

Jump size is dependent on which two states the system is jumping between, but is generally in the range of 1-10mV ($1.35 - 13.5\text{m}\Phi_0$). For a given pair of states, the jump height between the states depends on temperature (due to the change in λ_{ab}, as described above). In all cases the jump size observed in the telegraph noise measurements was smaller than the full 'in' to 'out' jump size as measured in the magnetization sweeps, and we believe all our measurements were were of jumps between 'in' and an intermediate state or 'out' and an intermediate state. Very rarely we also observed a transition between two different intermediate states, or a change from switching between 'in" and intermediate to switching between intermediate and 'out.' A change in the participating states would also lead to a change in the jump rate (e.g. Fig. 6.11).

Spontaneous jumping only occurs for a relatively narrow range of fields near where the ring has $\sim (n+\frac{1}{2})\Phi_0$ external flux applied. The jump rate is peaked at $(n+\frac{1}{2})\Phi_0$ flux bias and tails off sharply on either side. The height of the peaks is observed to follow an Arrhenius law (Fig. 6.12), indicating that the jump rate is controlled by thermal activation. The characteristic energy is, however, different for sets of peaks corresponding to jumps between different sets of states, implying that the barriers between different pairs of states are quite different.

The peak position is also observed to be temperature dependent (see Fig. 6.12). If λ_{ab} is changing as a function of T, then so is A_{eff}, and the centre of the peak should also shift with T, unless it is already at $B = 0$. We have observed this for one of the peaks we measured. The other was already centred at zero. It is unclear why jumps in magnetization sweeps and telegraph noise peaks are often *conspicuously* near $I_{\text{fc}} = 0$. At zero applied field, the ring should be in its minimum energy state with no shielding currents necessary. Jumps should begin to occur when the applied flux makes it possible to reduce the shielding currents by introducing a vortex, i.e. when the external field is nearer $\pm\frac{1}{2}\Phi_0/A_{\text{eff}}$ than to zero. One possible explanation is simply

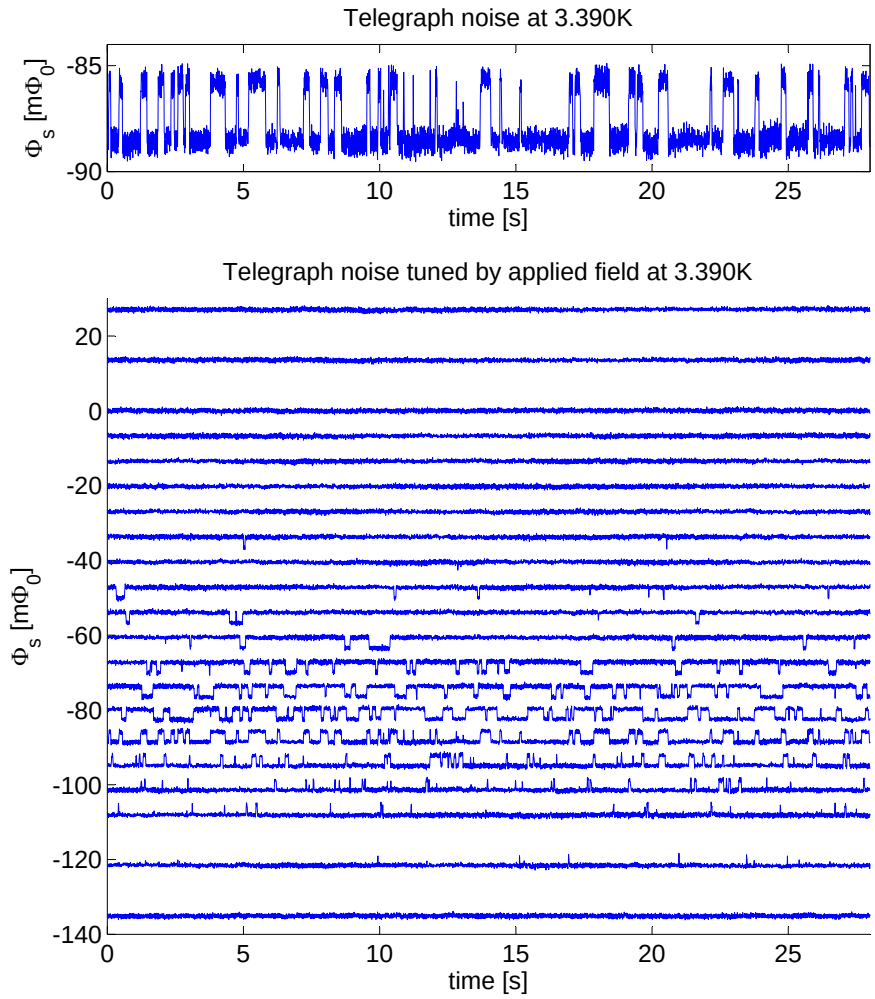

Figure 6.10: Timetraces showing telegraph noise caused by fluxoid switching in the ring. (a) A typical timetrace for fluxoid switching when the external field is near $(n + \frac{1}{2})\Phi_0/A_{\text{eff}}$. Note that the upper state in this trace is less energetically favourable: the fluxoid spends most of the time in the lower state and makes relatively short excursions to the upper state. (b) A sequence of timetraces (each offset by $6.75\text{m}\Phi_0$ for visibility) from which the timetrace in (a) was taken. Each timetrace is taken at a different applied field which determines the characteristic time for switching between states. The fluxoid begins in one state (in the lowest timetrace) and as the applied field is incremented (successive traces) it begins switching to the upper state until, in the top traces, it is solidly in the upper state. The switching rate is maximized when the applied field makes the two states degenerate. Plotting the inverse of the mean switching time vs. the applied field gives the peaks shown in Fig. 6.12

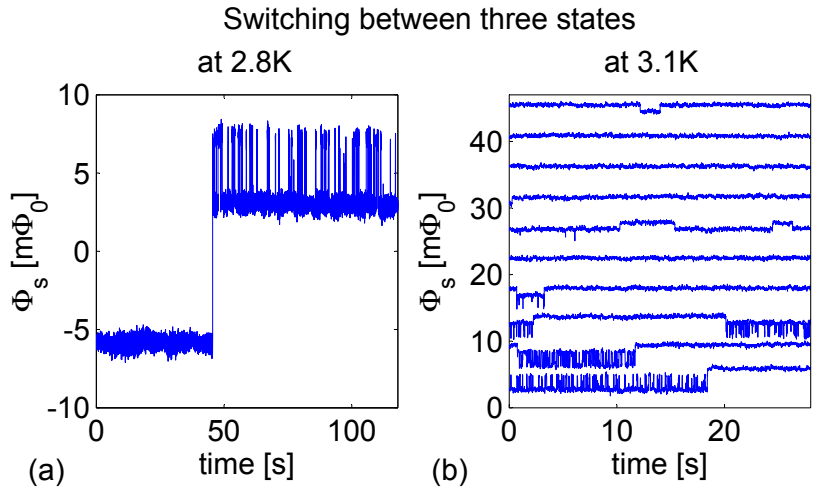

Figure 6.11: Very occasionally we observed the ring switching between three different states. (a) The fluxoid begins in state 1. At $t \approx 45$ seconds it switches to state 2 and begins telegraph switching with state 3. The flux difference $\Delta\Phi_s$ between the top and bottom states is consistent with these states differing by one fluxoid in the ring (i.e. top and bottom states are 'in' and 'out'). (b) A sequence of timetraces (each offset by $5\text{m}\Phi_0$ for visibility) taken during another data run. Each timetrace is taken at a different applied field. Distinct upper, middle and lower states are visible. The characteristic time for switching between the upper and middle states is much longer than that for the middle and lower states. As the applied field is tuned (successive traces) the lower state becomes less energetically favourable and switching occurs only between the upper and middle states. The flux difference $\Delta\Phi_s$ between the top and bottom states in these traces appears to be smaller than one full fluxoid difference in the ring at this temperature. This is evidence for two intermediate states with different characteristic timescales.

that our apparatus has a residual field of $\frac{1}{2}\Phi_0/68\mu\text{m}^2 = 0.15\text{G}$. However, we operate in a magnetically shielded dewar which specifies 80dB attenuation, and Earth's field is already only 0.5G. In addition, a random offset field would not be expected to be so near 0.15G any more (or less) than some other small number. While, explanation might apply for a peak near zero field which nonetheless changes position with T, it cannot explain a peak which stays at the same field regardless of T.

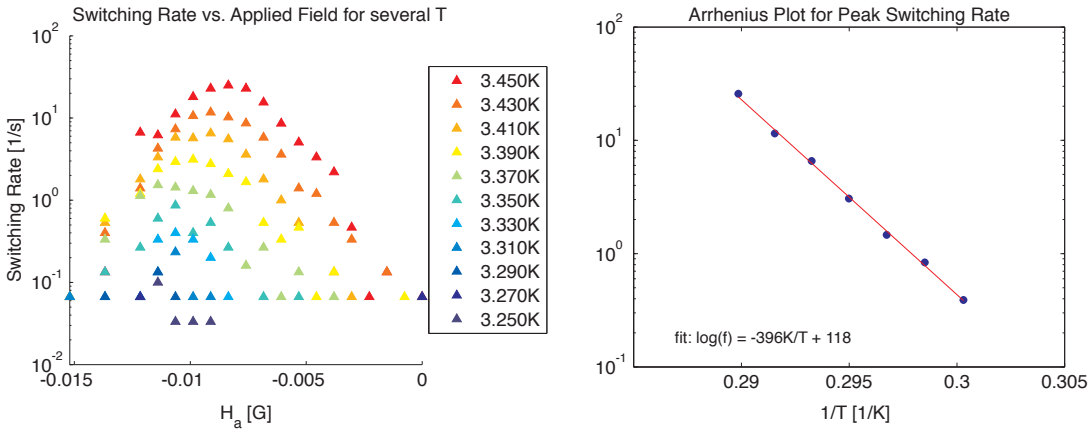

Figure 6.12: The fluxoid switching rate shows sensitive dependence on the applied field and also on temperature. The width of the peak in fluxoid switching rate is tiny compared to the inter-peak spacing showing that the fluxoid switching occurs only when the 'in' and 'out' states are very close to degenerate. The peak shifts slightly with increasing T as the effective area increases due to increasing λ_{ab}. (a) Log scale plot of fluxoid switching rate vs. applied field and temperature. (b) Arrhenius plot of the peak heights showing thermal activation of the fluxoid switching.

The peaks are often not symmetric. This can be observed directly in the timetraces where, on one side of the peak, the system makes many jumps into the other state, but hardly stays there for any time at all (Fig. 6.10(b)). Since we plot number of jumps vs. applied field, this gives an asymmetric peak. This might indicate that although the two states participating in the telegraph noise are close in energy (at the given temperature and field conditions), they may have different characteristic escape times τ_0.

6.6 Conclusions

Instead of measuring simple jumping of fluxoids in and out of the ring, we found a complex system in which (presumed) pinning sites in the material would trap the fluxoids in states which were intermediate between 'in the ring' and 'out of it.' The effects of these intermediate states is clearly visible on the magnetization sweeps (Fig. 6.5) in the form of separation of branches of the curve by small jumps. The intermediate states dominate the fluxoid dynamics in the sense that fluxoids almost never jumped between 'in' and 'out,' but rather between 'in' and some intermediate state or 'out' and some intermediate state. In principle one might expect the importance of the intermediate states to fade as the temperature approaches T_c from below. In practice, at temperatures where the fluxoids seemed to jump all the way in and out of the ring without stopping at intermediate states, the signal $\Delta\Phi_s$ associated with the jumps was sufficiently small as to make telegraph noise measurements difficult, and it was sufficiently close to T_c that there was little room left to vary the temperature.

One possible complication is that of lateral fields. We have no way to measure residual lateral fields at our sample, and though we operate in a magnetically shielded environment and therefore expect all residual fields to be small, we have no measurement of this. A lateral field could create Josephson vortices in the ring, and only a small field $H_\perp \approx 50$mG would be needed to do this since shielding is very poor in that direction because λ_c is so big – i.e. there is probably not a large Meissner regime. Such a Josephson vortex might act as a pinning centre for the fluxoids whose hopping we are trying to measure.

The temperature dependence of the magnetization sweep data is due to the temperature dependence of the penetration depth. The slopes of the linear parts are a measure of the diamagnetic response of the ring, which depends on the screening currents available, and hence on λ_{ab}. The magnitude of the jumps are a measure of the fluxoid, and the flux spreading, both of which depend essentially on λ_{ab}. Both of these measures relate to λ_{ab} in a geometrically non-trivial way – however, they can in principle be modelled because we know our ring geometry well. This suggests that we could extract the temperature-dependent penetration depth. Currently, the

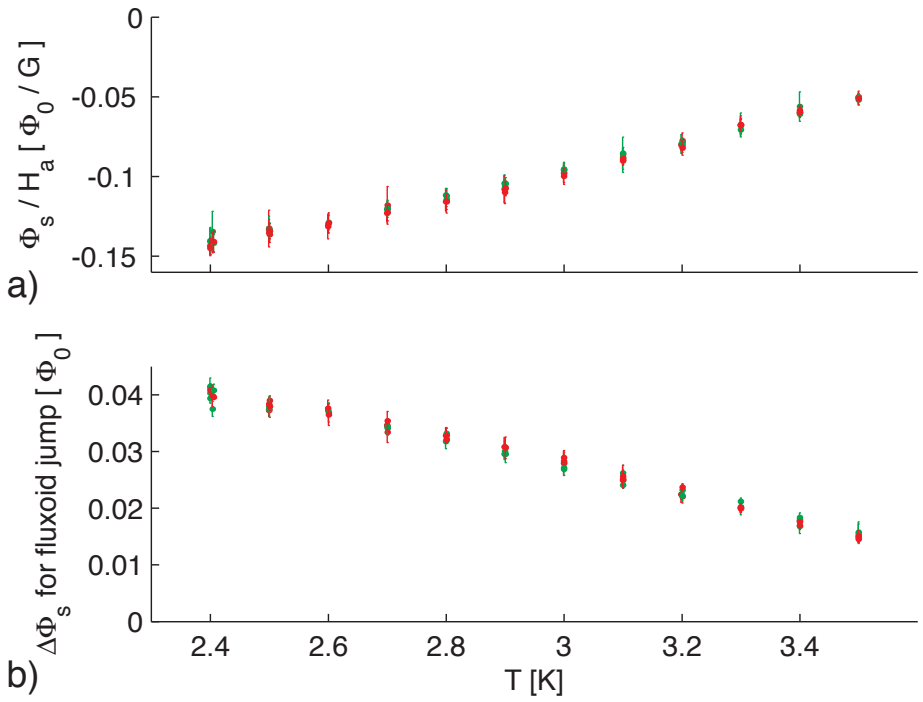

Figure 6.13: a) Diamagnetic response vs. T as measured by the average slope of the magnetization sweep on the linear areas between fluxoid jumps. b) Magnitude of the flux change, $\Delta\Phi_s$, measured by the SQUID in a fluxoid switching event for various temperatures. Data are obtained from the magnetization sweep data (Fig. 6.5) by subtracting a linear fit of the diamagnetic response, then measuring the difference in flux between the major branches.

unknowns in the system are $\lambda(T)$ and h, the latter of which is fixed. Given h, we could, solve for $\lambda(T)$ from $\Delta\Phi_s(T)$, but this is not well constrained. Ideally, we would like to vary h at each temperature in order to extract λ from the best fit of $\Delta\Phi_s(h)$ for each T, because then the quality of the fits would validate the model. Figure 6.13 shows the diamagnetic response and $\Delta\Phi_s$ extracted from the magnetization sweep vs. T data. The fact that these change by many times their associated error bars over the temperature range we are able to measure suggests that, with the appropriate model, this could prove a useful technique to measure λ_{ab}.

The fact that the intermediate states persisted almost all the way up to T_c indicates that they are associated with very deep pinning sites. Furthermore, the magnetization sweeps at any given temperature were quite repeatable, indicating that the same intermediate states were being accessed on each sweep. This also argues for the pinning sites being relatively scarce. If there were many such sites available, one would expect different sites to be accessed on repeated sweeps of the applied field. See Fig. 6.14 for a schematic representation. As discussed below, it is not clear exactly what the horizontal axis represents, because the way in which the vortex crosses the ring wall is not understood, nor the nature of the intermediate states it encounters along the way.

Our telegraph noise measurements lead to a similar conclusion: Over each range in temperature, switching occurred into a single intermediate state (with the very rare exceptions as discussed and shown in Fig. 6.11). The fact that we could follow thermal activation of the switching over $\sim$ 0.25K and two orders of magnitude in switching rate in with very little deviation from an Arrhenius law also indicates that we are observing only a single site over that temperature range – multiple different sites would have no reason to have the same activation energy.

Indications of such deep pinning sites can also be inferred from the observation of apparent 'partial vortices' by Guikema (2004). The 'partial vortices' are believed to be split stacks of pancake vortices where each sub-stack is strongly pinned and the split is sufficiently near the surface of the sample that residual fields of the sub-surface terminated stack penetrate up through the surface where they can be observed by a scanning SQUID or Hall probe.

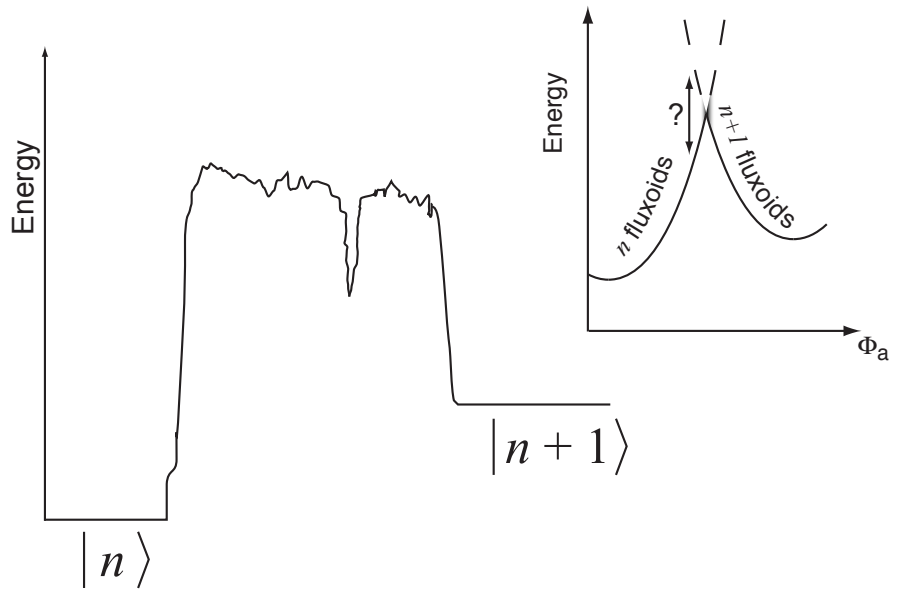

Figure 6.14: The vortex escaping (or entering) over the ring wall via thermal activation encounters a complex pinning landscape. Our observation of thermally activated telegraph noise arising from switching to and from a single pinning site for any given temperature indicates that pinning sites are dilute but deep.

Ideally, one would like a model of the pinning sites in a ring such as we measured. What exactly happens at higher temperatures to the pinning site we measured at 2.4K? Is there still switching on timescales far too short for us to see? Has it been absorbed into the 'in' state or 'out' state, perhaps actually swallowed by the encroaching penetration depth with increasing T?

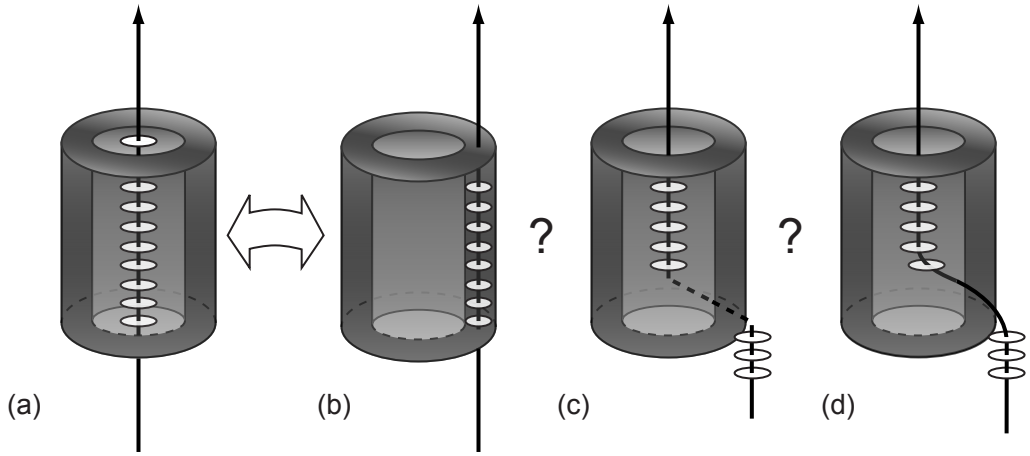

Figure 6.15: Several different pictures are possible for the intermediate states we observe. The vortex in (a) could: (b) Remain oriented along the axis of the ring and jump to a state entirely within the ring wall (unlikely because columnar defects are unlikely, and the energy cost of putting a vortex in each layer would be prohibitive). (c) Have a clean cut with pancake vortices in all layers above the cut, and none in the layers below it. (d) Escape through the ring wall as a Josephson vortex. The difference between (c) and (d) depends on the strength of the Josephson coupling. Note that pancakes do not actually exist outside the ring, and that in our rings λ_c is sufficiently large that the Josephson vortex whose core is shown in (d) should extend around the entire circumference of the ring. These pictures are figurative only.

The energy scales we measure are far too small for the picture of a rigid, axially oriented vortex jumping radially in and out of the ring. (A simple calculation of those energies yields an activation energy in the millions of Kelvin unless the ring is extremely close to T_c.) Our measurement then suggests thinking of the vortex

as a collection of pancake vortices, one in each layer, coupled either electromagnetically or with both electromagnetic and Josephson coupling (pictured schematically in Fig. 6.15). The coupling must still be fairly strong since we always observe fluxoid jumps between just a few states (usually 'in,' 'out,' and one intermediate) rather than a multitude or continuum of states that one might expect from a set of independent pancakes.

This becomes an open question: How do the fluxoids jump? The low activation energies suggest something like single pancakes (or small groups) jumping and then causing their fellows to follow shortly after, perhaps in a zipper-like fashion. Is the jumping controlled by a statistical, long range electromagnetic interaction between pancakes? Or is it a zipper-like effect with a Josephson vortex through the wall of the ring as the zipper pull? In either picture, what kind of pinning sites control the intermediates states we observe? In the Josephson coupled case, what does the Josephson vortex core look like? (We expect our rings have λ_c in excess of 100μm, making the flux profile of the Josephson vortex pretty much azimuthally isotropic around the ring and leaving very little interlayer current flow.)

6.7 Future Work

With a proper theoretical model and ideal sample, it would be interesting to pursue the original goal of measuring telegraph noise in the rings without intermediate states. If the intermediate states are indeed caused by pinning which impedes vertical movement of Josephson vortices, this may be possible by making thinner rings. If the intermediate states don't go away, that would argue against the Josephson coupling picture. Perhaps if controlled pinning sites could be introduced, this would become a useful approach for the study of pinning of individual vortices by different pinning mechanisms. One could also imagine pursuing the telegraph noise study without pinning into the quantum regime by going to much lower temperatures and thinner ring walls for which jump times at low T will still be anthropocentric.

Chapter 7

Conclusion

The Scanning SQUID is a uniquely useful tool that, because of its excellent flux sensitivity, has been applied to many problems that can be addressed with magnetic imaging. The addition of the field coil to allow for susceptometry and other uses of locally applied fields has greatly expanded the scanning SQUID's capabilities, and opened up new lines of research. I have chosen to pursue vortices in the cuprate superconductors, but even within the Moler lab, others have applied them to studies of Sr_2RuO_4, niobium films and tungsten superconducting devices, and a project to use them for measurements of persistent currents in normal metal rings is currently underway. Other possible uses include studies of nanomagnets or mesoscopic superconductors, searching for trace amounts of superconductivity or magnetism in novel materials, studies of vortex pinning strength in various materials – especially measurement of pinning strength in devices. The problem of being unable to see the field below the surface is not an issue in the case of thin films or nanomagnets, which are likely candidates for technological applications where this technique might be most useful.

We have demonstrated the first scanning SQUID susceptometer by imaging the superconducting transition of 3μm disks of tin, and then applied these SQUID susceptometers to extensively study the behaviour of single vortices in very underdoped $YBa_2Cu_3O_{6+x}$. We have moved single vortices and created vortex-antivortex pairs and observed the characteristics of their annihilation. Both of these sets of studies give general information on the pinning landscape which the vortices inhabit. Eric

Straver (2004) has built our lab's MFM and used it to raise single vortex manipulation to the level where we are now able to write letters with vortices (he chose to write SU for Stanford University), and to measure vortex pinning forces in optimally doped $YBa_2Cu_3O_{6+x}$.

Our experiments on the underdoped cuprates were made possible by the availability of new samples grown by Ruixing Liang et al. (1998, 2001), and also by the availability of a focussed ion beam (FIB) here in the Geballe Laboratory for Advanced Materials, which has allowed us to mill our samples into rings. Using the $YBa_2Cu_3O_{6+x}$ single crystals, we have tested the predicted memory effect for vortices in a ring-shaped sample, and from this deduced a limit on the possible energy of the vison, an excitation predicted in spin-charge separation theories to inhabit the vortex core. In conjunction with the our measurement of $h/2e$ flux quantization (Wynn et al. 2001), this essentially eliminates the vison-based spin-charge separation theories of the cuprates.

We have measured the dynamics of thermally excited vortices in a superconducting ring, including the thermal activation to available pinning sites in the ring. We have shown that this occurs at temperatures much lower than would be expected for a rigid vortex, indicating that vortices in this regime are pancake vortices coupled via electromagnetic and possibly Josephson interactions.The discovery of robust intermediate states for vortices hopping in and out of a $YBa_2Cu_3O_{6.354}$ ring, was unexpected and further study of the nature of vortex dynamics would be necessary to determine the nature of the states we observed. The most likely possibilities seem to involve pinning of Josephson vortices which connect stacks of pancake vortices. If some such pinning is the answer, then we believe that this data, taken in conjunction with the annihilation data for vortex-antivortex pairs, in which vortices went through several distinct pinning sites before annihilation, indicate that pinning in underdoped $YBa_2Cu_3O_{6.354}$ is characterized by deep, sparse pinning sites separated by a characteristic scale on the order of microns.

Pinning in very underdoped samples is complicated by this fact that vortices seem to move as coupled pancakes slipping around, rather than as rigid stacks, and understanding of the role of Josephson coupling compared to simple electromagnetic

coupling would be useful in producing a clearer picture of vortex pinning and dynamics in this doping regime. That could open the doors both to practical studies of pinning for technological applications, and possibly more vortex-based tests of theories of the cuprates.

Our data on the temperature dependance of the flux change for vortices jumping in and out of a ring, as well as the diamagnetic response, suggest that we could extract the temperature-dependent penetration depth. Currently, the unknowns in the system are $\lambda(T)$ and h, the latter of which is fixed. Given h, we could, in principle, solve for $\lambda(T)$ from $\Delta\Phi_s(T)$, but this is not well constrained. Ideally, we would like to vary h at each temperature in order to extract λ from the best fit of $\Delta\Phi_s(h)$ for each T, because then the quality of the fits would validate the model. One could also imagine varying x and y by performing a scanning experiment. Hendrik Bluhm has produced a finite element Maxwell-London model which we believe is sufficient for this idea. It remains only to set up a ring in a scanning system with an externally applied field, which should be possible with our new generation of symmetric SQUIDs. This might extend earlier work by Guikema (2004) in which the size of a vortex (usually determined by λ) was found to be abnormally large at very low dopings, suggesting a possible violation of the Uemura relation. Even if this turns out not to be the case, a good measurement of λ_{ab} at these low dopings is quite valuable.

Every experimentalist spends some time building instrumentation, and apart from my experimental work, I built a set of high-bandwidth, direct-feedback SQUID controllers based on a design from John Martinis at NIST Boulder which we now use for all of our SQUID measurements in the lab. Our collaboration with Martin Huber of CU Denver/NIST has led to a new generation of SQUID susceptometers with smaller (4μm) circular pickup loops and a well-shielded, symmetric design that eliminates most background flux, allowing these SQUIDs to operate in higher ambient fields. Other design improvements include moving all the bonding pads to the back of the chip to allow the SQUID to be aligned at a shallower angle to the surface for scanning. The NIST fabricated SQUIDs also seem to have slightly improved noise characteristics compared to our previous generation fabricated at HYPRES.

Ten years ago, resolving individual vortices was difficult and simply seeing them

was exciting. We were extremely excited the first time we saw them, too! Now there are many researchers who routinely image individual vortices. In one sense, the work presented in this thesis can be thought of as a succession of refinements of our techniques to image and probe individual vortices. One imagines that future researchers will engineer clever systems in which to study vortices, and hopes that one day this may elucidate the true mechanism for superconductivity in the cuprates.

Appendix A

Visons and Senthil-Fisher $\mathbb{Z}_2$ Gauge Theory

Gauge Principle: Quantities which are conserved globally are conserved locally, not merely globally.

We know that conserved quantities arise from symmetries of the Lagrangian (this is the content of Noether's Theorem).

There are two distinct types of symmetries:

- Internal
- External

External symmetries are the ones we are used to:

- translation → conservation of momentum
- rotation → conservation of angular momentum
- time translation → conservation of energy
- etc.

These are symmetries of the Lagrangian under transformations of spacetime (the manifold on which the Lagrangian lives).

Internal symmetries arise from transformations of the Lagrangian variables themselves. E.g.

$$\mathcal{L} = \partial_\mu \phi \partial^\mu \phi^* - m^2 \phi^* \phi \qquad \text{where } \phi(x^\mu) \text{ is in } \mathbb{C}. \tag{A.1}$$

Here ϕ is a"complex scalar field" i.e. some complex number for every point in spacetime. The transformation $\phi \to e^{-i\Lambda}\phi$ (global phase shift $\leftrightarrow$ rotation of ϕ in the complex plane) leaves the Lagrangian invariant. The study of such internal symmetries and their consequences constitutes Gauge Theory.

This particular symmetry corresponds to the conservation of charge. The Gauge Principle says we should require this to be a *local* symmetry. This is because relativity eschews doing the same thing to all points in space at the exact same time. So we let the number Λ depend on $\vec{x}$ and t. $\Lambda = \Lambda(x^\mu)$. This changes things because

$$\partial_\mu \phi \to \partial_\mu \left(e^{-i\Lambda(x^\mu)} \right) \phi = (\partial_\mu \phi e^{-i\Lambda})\phi + e^{-i\Lambda}\partial_\mu \phi = -i(\partial_\mu \Lambda) e^{-i\Lambda}\phi + e^{-i\Lambda}\partial_\mu \phi \tag{A.2}$$

Our derivative $\partial_\mu \phi$ doesn't transform like ϕ does, so in transforming our Lagrangian we pick up an extra term

$$\left(-i\phi\partial_\mu \phi^* + i\phi^* \partial_\mu \phi\right) \partial_\mu \Lambda. \tag{A.3}$$

We can get rid of this term by adding some terms containing another field which transforms like

$$A_\mu \to A_\mu + \frac{1}{e}\partial_\mu \Lambda. \tag{A.4}$$

Of course, this statement is devoid of intuitive meaning. If you play the math game and do this, you see that you are defining a new sort of derivative, the "covariant" derivative,

$$D_\mu = \partial_\mu + ieA_\mu. \tag{A.5}$$

This derivative takes into account the variation due to moving along the manifold, and the variation due to the change in the symmetry transformation as you move

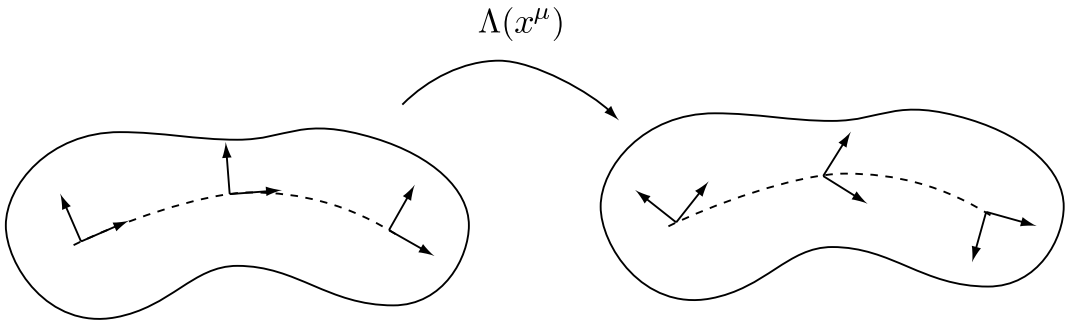

Figure A.1: A mapping induces a rotation of the basis vectors.

along the manifold. That's why you require the funny transformation law

$$A_\mu \to A_\mu + \frac{1}{e}\partial_\mu \Lambda. \tag{A.6}$$

where the $1/e$ is some scale factor (essentially to fix units) and the $\partial_\mu \Lambda$ is how your symmetry changed moving along the manifold. This new field A_μ is called the Gauge Field (or to impress your friends you can use math lingo and call it a "connection").

Another example of this comes up in fluid mechanics, where you have the "advective derivative" (same thing) which tells you how things are changing from the point of view of someone riding along with the flow of the fluid.

To explore this just a bit further, these are all examples of parallel transport: you have some basis vectors for a space (here $\mathbb{C}$) defined at every point on some curvy manifold (spacetime). At each point on our manifold we've done something to our little basis vectors: we've rotated them (Fig. A.1). (You could also squish, but we haven't.)

So what we've done with $\Lambda(x^\mu)$ is changed the coordinate systems for $\mathbb{C}$ at each point on our manifold. Then $\partial_\mu \phi$ is not covariant because $\phi(x^\mu)$ and $\phi(x^\mu + dx^\mu) = \phi(x^\mu) + d\phi$ are measured in different coordinate systems (Fig. A.2).

What is the value $\phi + \delta\phi$ which $\phi(x^\mu)$ would have had under parallel transport?

- It is proportional to ϕ

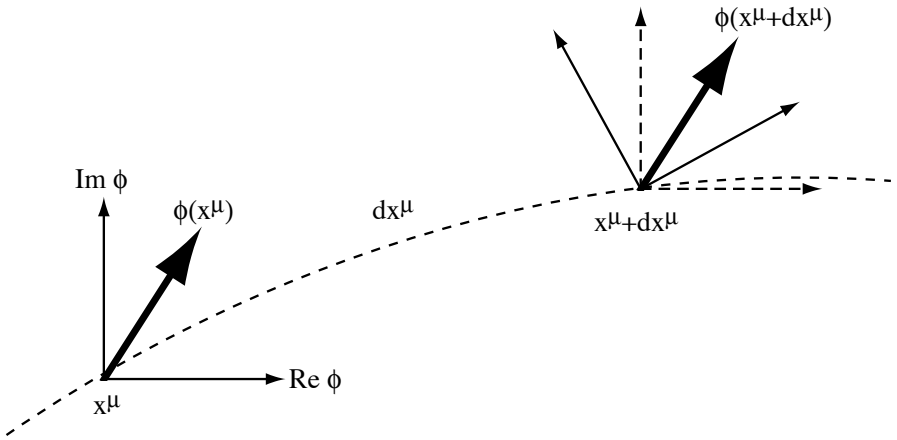

Figure A.2: The regular derivative ignores the fact that the axes rotated while you shifted them a distance dx^μ and compares $\phi(x^\mu + dx^\mu)$ with $\phi(x^\mu)$. The covariant derivative compensates for the rotation of the axes and compares $\phi(x^\mu + dx^\mu)$ with the value $\phi(x^\mu)$ *would have had* if it were carried to $x^\mu + dx^\mu$ keeping the axes fixed (parallel transport). In this picture, the covariant derivative uses the dotted axes at $x^\mu + dx^\mu$, while the regular derivative uses the solid axes.

- It is proportional to dx^μ
- It is proportional to some field telling us how the axes were rotated and/or squished.

A_μ is that field. The initial choice of A_μ corresponds to choosing the axes of $\mathbb{C}$ at each point on the manifold. Then transformations $A_\mu \to A_\mu + \frac{1}{e}\partial_\mu \Lambda$ do the right thing by telling us what additional rotation/distortion has been induced on the axes as we travel along any path on the manifold.

A few remarks before we see what all this has to do with visons:

1. In general, there will also be terms involving A_μ added to the Lagrangian to keep it symmetric under the Gauge transformation of interest. e.g.

$$\mathcal{L} = \partial_\mu \phi \partial^\mu \phi^* - m^2 \phi^* \phi \to D_\mu \phi D^\mu \phi - m^2 \phi^* \phi - \frac{1}{4} F^{\mu\nu} F_{\mu\nu} \tag{A.7}$$

   where $F_{\mu\nu} = \partial_\mu A_\nu - \partial_\nu A_\mu$, the electromagnetic field tensor.

2. Certain types of terms involving the gauge field don't keep the symmetry and are not added. e.g. $M^2 A_\mu A^\mu$ is not symmetric under $A_\mu \to A_\mu + \frac{1}{e}\partial_\mu \Lambda$. Terms like $\phi^* \phi$ and $A_\mu A^\mu$ correspond to self-energy, or mass. This is remarkable: the observation that $\mathcal{L}$ had a symmetry and the requirement that it be a local symmetry has led us to discover the photon (A_μ) and showed us that the photon has no mass ($M^2 = 0$).

3. One last math-like observation before we tackle visons. The A_μ we know and love is probably most famous for its role in the Bohm-Aharanov effect: particles going around flux know about it. When do we see the Bohm-Aharanov effect? When there is flux

$$\Phi = \int \vec{B} \cdot d\vec{S} = \int \vec{\nabla} \times \vec{A} \cdot d\vec{S} = \oint \vec{A} \cdot d\vec{\ell} \tag{A.8}$$

The last part, $\int \vec{A} \cdot d\vec{\ell}$, tells us to add up the components of our "connection" along some loopy path and check if they sum to zero.

Yes $\Rightarrow$ no flux, no Bohm-Aharanov shift.

No $\Rightarrow \exists$ flux, Bohm-Aharanov phase shift.

Let's take a specific example of a solenoid of radius R

$$B_r = B_\phi = 0 \quad \forall \vec{x} \tag{A.9}$$

$$B_z = \begin{cases} B & \text{inside solenoid} \\ 0 & \text{outside} \end{cases} \tag{A.10}$$

In the region outside the solenoid $\vec{B} = \nabla \times \vec{A} = 0$ so we may write

$$\vec{A} = \nabla \chi = \frac{1}{r} \frac{\partial}{\partial \phi} \chi \hat{\phi} = \frac{BR^2}{2r} \hat{\phi} \tag{A.11}$$

$$\text{so } \chi = \frac{BR^2}{2} + \text{const.} \tag{A.12}$$

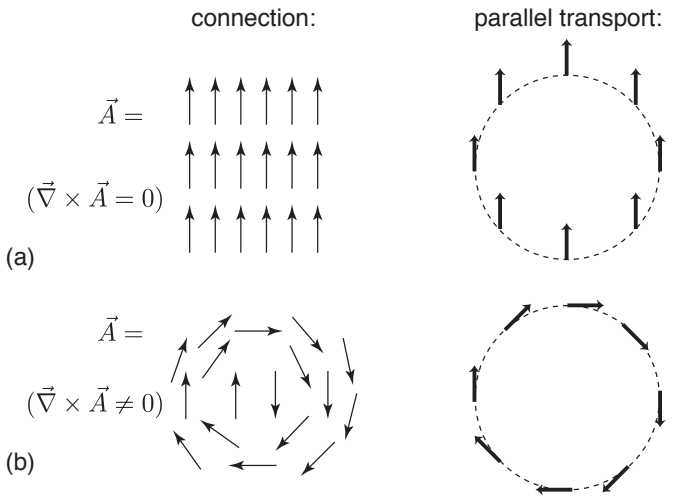

Figure A.3: Topology and connections: (a) Given a connection $\vec{A}$ with zero curl, parallel transport of a vector around a closed loop induces no winding of the transported vector. (b) For the curling connection (i.e. when there is flux of the gauge field), parallel transport of a vector around a closed loop winds the vector, indicating the presence of a topological defect inside the loop.

Now note that $\Phi = \int_{\text{circle}} \vec{A} \cdot d\vec{\ell} = \int_{\text{circle}} \nabla\chi \cdot d\vec{\ell} = \chi(2\pi) - \chi(0) \neq 0$. So χ is not single valued. That means either it is not regular, nice, differentiable, etc., or it lives on a funny space like a corkscrew. This is mathematically equivalent to a space with a hole poked in the middle where you have to keep track of how many times you went around the hole. In fancy terms, the connection A_μ is telling us about the topology of the vacuum. So far I have avoided saying what the symmetry was that gave us A_μ – it is the rotations of the plane SO(2) or U(1). It is the topology of this group, specifically that it is not simply connected, that allows the Bohm-Aharanov effect. (It does not necessitate non-zero phase shifts – if there is no flux χ is single valued.)

The point of this digression is that if we follow our connection around a loop using parallel transport and end up with a vector different from the one we started with, then there is a topological defect inside. As an example, consider the situation in figure A.3.

With all the preliminaries out of the way, we can turn to the question "So what is a vison, anyway?"

Here's our theory, defined by the action:

$$\begin{aligned} S = \int \mathcal{L} dt &= t_c \sum_{<ij>} \sigma_{ij} (b_i^* b_j + c.c) \\ &+ \sum_{<ij>} \sigma_{ij} (t_{ij}^s \bar{f}_{i\alpha} f_{j\alpha} + t_{ij}^{\Delta} f_{i\uparrow} f_{j\downarrow} + c.c) + \Sigma_i \bar{f}_{i\alpha} f_{i\alpha} \\ &+ K \sum_{\square} \prod_{\square} \sigma_{ij} + \text{Berry's phase} \end{aligned} \tag{A.13}$$

$$\begin{aligned} b^* &= \text{chargon operator} \\ f^* &= \text{spinon operator} \\ \sigma_{ij} &= \text{the connection, or Gauge field} \end{aligned}$$

This is already the fully invariant action. The symmetry which got us here in this case is

$$\begin{cases} b \to -b \\ f \to -f \end{cases} \quad \text{or } \mathbb{Z}_2 \tag{A.14}$$

The reason we don't have U(1) symmetry is due to the existence of terms like $f_{i\uparrow} f_{j\downarrow}$.The symmetry is local since you can choose to send $b_i \to -b_i, f_i \to -f_i$ on each lattice site, or not, independently. If you change, or "flip" site i, then you need to look at all of the neighbouring sites j and see if they flipped. If not, you have to change the connection σ_{ij} So our transformation $\Lambda(i)$ is

$$\Lambda_i = \begin{cases} b_i \to -b_i \\ f_i \to -f_i \end{cases} \equiv 1 \quad \text{or} \quad \Lambda_i = \begin{cases} b_i \to b_i \\ f_i \to f_i \end{cases} \equiv 0 \tag{A.15}$$

and

$$\sigma_{ij} \to \sigma_{ij} +_2 (\Lambda_i +_2 \Lambda_j) \tag{A.16}$$

where we have taken the representation $\mathbb{Z}_2 \to (\{0,1\}, +_2)$ and $+_2$ is addition mod 2.

In the multiplicative representation $\mathbb{Z}_2 \to (\{1,-1\},\cdot)$ the connection is instead

$$\sigma_{ij} \to \sigma_{ij} \cdot \Lambda_i \cdot \Lambda_j. \tag{A.17}$$

Our manifold is a square lattice, and the space above each (spacetime) lattice point is $\{\uparrow,\downarrow\}$. Parallel transport becomes flipping or not flipping when you move from one lattice site to the next. The Bohm-Aharanov effect becomes simple summation (or multiplication) of the connection values around a path. The Vison is this defect. It is the flux of the gauge field σ_{ij}.

Some questions remaining to be answered:

1. Why does the vison nucleate (or at least like to attach to) an $h/2e$ vortex?
2. Why is the hole necessary in the Senthil experiment?
3. What's all the hooplah about "confined," "deconfined," and "topoligical order"? What is the vison condensate?
4. Why do we have the even-odd phenomenon with visons generating vortices?
5. What drives the phase transitions and how is each phase characterized?

Answers, as much as I can provide them:

1. *Why does the vison nucleate (or at least like to attach to) an $h/2e$ vortex?* The phase of a superconducting wavefunction must be $n2\pi$ on going around a loop.

$$n2\pi = \Delta\theta = \oint \nabla\theta \cdot d\vec{\ell} = \frac{e^*}{\hbar} \oint \vec{A} \cdot d\vec{\ell} = \frac{e^*}{\hbar}\Phi \tag{A.18}$$

$$\Rightarrow \Phi = n\frac{2\pi\hbar}{e^*} = n\frac{h}{e^*} \tag{A.19}$$

which is the condition for flux quantization. But suppose we have a vison in the loop. Then

$$n2\pi = \Delta\theta = \oint \nabla\theta \cdot d\vec{\ell} = \underbrace{\pi}_{\text{from vison}} + \frac{e^*}{\hbar} \oint \vec{A} \cdot d\vec{\ell} = \pi + \frac{e^*}{\hbar}\Phi \tag{A.20}$$

$$\Rightarrow \Phi = (2n-1)\pi\frac{\hbar}{e^*} = (2n-1)\frac{h}{2e^*} \tag{A.21}$$

so we see that the presence of a vison requires an odd number of flux quanta be associated with it in order to preserve the single-valued character of the wavefunction.

2. *Why is the hole necessary in the Senthil experiment?* It is important that the states with a vison and without a vison be degenerate in the normal state so that we don't attract or expel visons when we warm up and get rid of the vortex. There is still an energy cost (T^*) associated with a lone vison in the normal state, so that it might tend to try to run out of your sample without a hole. If we make a hole for it to sit in, it will generally stay there (excepting the possibility of taking thermal energy to escape).

3. *What's all the hooplah about "confined," "deconfined," and "topological order?" What is the vison condensate?* Recall that chargons or spinons circling around a vison pick up a phase of π. Note also that the reverse holds true: visons circling around a chargon or spinon also pick up a phase of π. This makes moving around rather difficult, as it can only be accomplished as long as nobody's wavefunction gets an odd π. When all the chargons condense into a single wavefunction, it is impossible for the vison to move anywhere at all without being accompanied by $h/2e$ of flux, or by another vison. We thus say that the vison is *confined*, and in this case it is driven by the condensation of the chargons. The reverse can also happen: if the visons proliferate and condense, it becomes impossible for the chargons to go anywhere without their spinons, and vice versa. This is the situation above the pseudogap, where the spinons and chargons are *confined* into behaving as proper electrons by the vison condensate. In the pseudogap, neither visons nor chargons are condensed, and chargons, spinons, and visons are all *deconfined*.

   As for topological order, consider a ring of cuprate superconductor. The fact that the two states with and without a vison in the ring are degenerate is due to symmetry of the system. This is in fact a topological symmetry, because it

has to do with the winding of the phase around the cylinder. Although the two states degenerate, their *wavefunctions* are *not* the same, and you can clearly tell whether the system is in one state or the other. Thus, we have a *broken* topological symmetry, which is also called a topological *order*. All this is true when the vison is gapped and cannot escape through the ring wall. If the vison gap goes away, however, and visons are free to propagate through the material, then there is no longer a useful distinction between states with and without a vison in the hole. There is no more broken topological symmetry, and no topological order. This is what occurs above T^* where not only are visons plentiful, they in fact form a condensate.

4. *Why do we have the even-odd phenomenon with visons generating vortices?* Any path encircling two visons (or any even number) has a odd number of '+1' links contributed from each of them to the sum of the σ_{ij} along the path. These give an overall even number of ones, which cancel out in addition mod 2, leaving zero net gauge flux, and hence no need for a vortex. Similarly, any odd number of visons contributes an odd number of ones to the sum of the σ_{ij}, yielding a net gauge flux of one unit, and requiring a vortex.

5. *What drives the phase transitions and how is each phase characterized?* At high temperature (above T^*) are plentiful. In fact, we have a vison condensate which means that the chargons and spinons are confined, that is, they cannot move independently and are forced to stay together and behave as proper electrons. Visons, on the other hand, are deconfined. As T is decreased below T^* the vison becomes energetically expensive and there is no longer a vison condensate. We are in the pseudogap state, and the spinons and chargons can separate. The pseudogap is in fact the vison gap – the vison energy you have to pay to bind a spinon and chargon into an electron which your experiment measures. In the pseudogap visons, chargons, and spinons are all deconfined. As you decrease T below T_c, the chargons condense into a superconducting state and the visons become confined: unable to separate from their attached flux.

List of References

A. A. Abrikosov. On the magnetic properties of superconductors of the second group. *Soviet Physics JETP-USSR* **5**, 1174 – 1183 (1957).

P.W. Anderson. The resonating valence bond state in La_2CuO_4 and superconductivity. *Science* **235**, 1196–8 (1987).

D. D. Awschalom and J. Warnock. Picosecond magnetic spectroscopy of two- and three-dimensional diluted magnetic semiconductors. *IEEE Journal of Quantum Electronics* **25**, 2570 – 9 (1989).

M.R. Beasley, R. Labusch, and W.W. Webb. Flux creep in type-II superconductors. *Physical Review* **181**, 682–700 (1969).

M. Breitwisch and D. K. Finnemore. Pinning of a single Abrikosov vortex in superconducting Nb thin films using artificially induced pinning sites. *Phys. Rev. B* **62**, 671–677 (2000).

V. Chandrasekhar, R. A. Webb, M. J. Brady, M. B. Ketchen, W. J. Gallagher, and A. Kleinsasser. Magnetic response of a single, isolated gold loop. *Physical Review Letters* **67**, 3578 – 81 (1991).

J. R. Clem and A. Sanchez. Hysteretic AC losses and susceptibility of thin superconducting disks. *Physical Review B (Condensed Matter)* **50**, 9355 – 62 (1994).

John R. Clem and Mark W. Coffey. Vortex dynamics in a type-II superconducting film and complex linear response functions. *Phys. Rev. B* **46**, 14662–14674 (1992).

P. G. de Gennes. *Superconductivity of Metals and Alloys.* Addison-Wesley, New York (1989).

A. M. Goldman. Lifetimes of persistent currents in superconducting loops interrupted by josephson junctions. *Journal of Low Temperature Physics* **3**, 55 – 63 (1970).

C.E. Gough, M.S. Colclough, E.M. Forgan, R.G. Jordan, M. Keene, C.M. Muirhead, A.I.M. Rae, N. Thomas, J.S. Abell, and S. Sutton. Flux quantization in a high-T_c superconductor. *Nature* **326**, 855 (1987).

A. Grigorenko, S. Bending, T. Tamegai, S. Ooi, and M. Henini. A one-dimensional chain state of vortex matter. *Nature* **414**, 728 – 31 (2001).

Janice Wynn Guikema. *Scanning Hall Probe Microscopy of Magnetic Vortices in Very Underdoped Yttrium-Barium-Copper-Oxide*. PhD thesis, Stanford University, (2004).

A. Hosseini, D.M. Broun, D.E. Sheehy, T.P. Davis, M. Franz, W.N. Hardy, Ruixing Liang, and D.A. Bonn. Survival of the d-wave superconducting state near the edge of antiferromagnetism in the cuprate phase diagram. `xxx.lanl.gov` cond-mat/0312542 (2003).

HYPRES Inc. URL `www.hypres.com`.

O .B. Hyun, J. R. Clem, and D. K. Finnemore. Motion of a single superconducting vortex. *Phys. Rev. B* **40**, 175 (1989).

O .B. Hyun, D. K. Finnemore, L. A. Schwartzkopf, and J. R. Clem. Elementary Pinning Force for a Superconducting Vortex. *Phys. Rev. Letters* **58**, 599 (1987).

M. B. Ketchen, D. D. Awschalom, W. J. Gallagher, A. W. Kleinsasser, R. L. Sandstrom, J. R. Rozen, and B. Bumble. Design, fabrication, and performance of integrated miniature SQUID susceptometers. *IEEE Transactions on Magnetics* **25**, 1212–1215 (1989).

M. B. Ketchen and J. R. Kirtley. Design and Performance Aspects of Pickup Loop Structures for Miniature SQUID Magnetometry. *IEEE Transactions on Applied Superconductivity* **5**, 2133–2136 (1995).

M. B. Ketchen, T. Kopley, and H. Ling. Miniature SQUID susceptometer. *Applied Physics Letters* **44**, 1008 – 10 (1984).

J.R. Kirtley, C.C. Tsuei, V.G. Kogan, J.R. Clem, H. Raffy, and Z.Z. Li. Fluxoid dynamics in superconducting thin film rings. *Physical Review B* **68**, 214505/1–8 (2003).

S.A. Kivelson, D.S. Rokhsar, and J.P. Sethna. 2e or not 2e: flux quantization in the resonating valence bond state. *Europhysics Letters* **6**, 353–8 (1988).

V. G. Kogan. Meissner response of anisotropic superconductors. *Physical Review B* **68**, 104511 – 1 (2003).

V. G. Kogan, A. Yu. Simonov, and M. Ledvij. Magnetic field of vortices crossing a superconductor surface. *Phys. Rev. B* **48**, 392–397 (1993).

D. Kouzoudis, M. Breitwisch, and D. K. Finnemore. Edge barrier pinning for a single superconducting vortex. *Phys. Rev. B* **60**, 10508–10512 (1999).

L. D. Landau and E. M. Lifshitz. *Electrodynamics of Continuous Media. 2nd Ed.* Pergamon Press, Oxford (1984).

Q. Li, J. R. Clem, and D. K. Finnemore. Nucleation and motion of an isolated Abrikosov vortex. *Phys. Rev. B* **43**, 12843–12847 (1991).

Q. Li and D. K. Finnemore. Abrikosov vortex memory based on a single vortex. *IEEE Transactions on Magnetics* **27**, 2913–2915 (1991).

R. Liang, D. A. Bonn, and W. N. Hardy. Growth of High Quality YBCO Crystals Using $BaZrO_3$ Crucibles. *Physica C* **304**, 105–111 (1998).

R. Liang, D.A. Bonn, W.N. Hardy, J.C. Wynn, K.A. Moler, L. Lu, S. Larochelle, L. Zhou, M. Greven, L. Lurio, and S.G.J. Mochrie. Preparation and characterization of homogeneous YBCO single crystals with doping level near the SC-AFM boundary. *Physica C* **383**, 1–7 (2002).

Ruixing Liang, D. A. Bonn, and W. N. Hardy. Preparation and Characterization of Homogeneous YBCO Single Crystals with Doping Level near the SC-AFM Boundary. unpublished, (2001).

Ruixing Liang, P. Dosanjh, D. A. Bonn, W. N. Hardy, and A. J. Berlinsky. Lower critical fields in an ellipsoid-shaped $YBa_2Cu_3O_{6.95}$ single crystal. *Physical Review B (Condensed Matter)* **50**, 4212 – 15 (1994).

M. A. McCord and D. D. Awschalom. Direct deposition of magnetic dots using a scanning tunneling microscope. *Applied Physics Letters* **57**, 2153 – 5 (1990).

K. A. Moler, J. R. Kirtley, D. G. Hinks, T. W. Li, and M. Xu. Images of interlayer Josephson vortices in $Tl_2Ba_2CuO_{6+\delta}$. *Science* **279**, 1193 – 6 (1998).

N. Nagaosa. e vs. 2e quantization in the spin gap phase of high-T_c superconductors. *Journal of the Physical Society of Japan* **63**, 2835–6 (1994).

L. R. Narasimhan, M. Takigawa, and M. B. Ketchen. Magnetic resonance of a small platinum particle using an integrated DC SQUID. *Applied Physics Letters* **65**, 1305 – 7 (1994).

A. Paramekanti, L. Balents, and M.P.A. Fisher. Ring exchange, the exciton Bose liquid, and bosonization in two dimensions. *Physical Review B* **66**, 054526/1–27 (2002).

A. Paramekanti, M. Randeria, and N. Trivedi. Fractionalization in spin liquid Mott insulators: vison wavefunctions and gaps. `xxx.lanl.gov` cond-mat/0303360 (2003).

J. Pearl. Structure of superconductive vortices near a metal-air interface. *Journal of Applied Physics* **37**, 4139–41 (1966).

B. L. T. Plourde. *Vortex distributions and dynamics in superconductors near surface steps and sample edges studied by scanning SQUID microscopy and critical current measurements*. PhD thesis, University of Illinois at Urbana-Champaign, (2000).

T.C. Ribeiro and X.-G. Wen. Possible Z_2 phase and spin-charge separation in electron-doped cuprate superconductors. *Physical Review B* **68**, 24501/1–6 (2003).

S. Sachdev. Stable hc/e vortices in a gauge theory of superconductivity in strongly correlated systems. *Physical Review B* **45**, 389–99 (1992).

B. A. Scott, J. R. Kirtley, D. Walker, B. H. Chen, and Y. H. Wang. Application of scanning SQUID petrology to high-pressure materials science. *Nature* **389**, 164 – 7 (1997).

T. Senthil and M.P.A. Fisher. Detecting fractions of electrons in the high-T_c cuprates. *Physical Review B* **64**, 214511/1–6 (2001).

J. Siegel, J. Witt, N. Venturi, and S. Field. Compact large-range cryogenic scanner. *Review of Scientific Instruments* **66**, 2520–3 (1995).

J. Sok and D. K. Finnemore. Thermal depinning of a single superconducting vortex in Nb. *Phys. Rev. B* **50**, 12770–12773 (1994).

Eric W. J. Straver. *Cantilever-based Measurements on Nanomagnets and Superconductors*. PhD thesis, Stanford University, (2004).

J.L. Tallon and J.W. Loram. The doping dependence of T^* – what is the real high-T_c phase diagram?. *Physica C* **349**, 53–68 (2001).

J.C. Wynn, D.A. Bonn, B.W. Gardner, Yu-Ju Lin, Ruixing Liang, W.N. Hardy, J.R. Kirtley, and K.A. Moler. Limits on spin-charge separation from h/2e fluxoids in very underdoped $YBa_2Cu_3O_{6+x}$. *Physical Review Letters* **87**, 197002/1–4 (2001).